EXPERIMENTAL INVESTIGATION OF THE INTERFACIAL THERMAL RESISTANCE IN URANIUM DIOXIDE AND BERYLLIUM OXIDE COMPOSITES BY THE FLASH METHOD

A Dissertation

by

RYAN ANTHONY BRITO

Submitted to the Office of Graduate and Professional Studies of
Texas A&M University
in partial fulfillment of the requirements for the degree of

DOCTOR OF PHILOSOPHY

Chair of Committee,	Sean McDeavitt
Committee Members,	Tahir Cagin
	Patrick Shamberger
	Lin Shao
Head of Department,	Ibrahim Karaman

December 2022

Major Subject: Materials Science and Engineering

ABSTRACT

The addition of a continuous, high thermal conductivity beryllium oxide (BeO) network to the uranium dioxide (UO_2) nuclear fuel microstructure has been proposed for improved accident tolerance. The interfacial thermal resistance (ITR) is identified as critical to understanding the effective thermal conductivity of UO_2 and BeO composites; however, existing measurements fit the ITR to underdetermined systems with complex percolated microstructures. This work presents a dedicated, combined experimental and analytical approach to quantify the ITR in UO_2-BeO composites by the flash method and examines the role of the ITR in the design of microstructures with improved thermal conductivity for nuclear applications.

Dense UO_2-BeO composites with a dispersed BeO granules were fabricated using methods aligned with industry practice to provide uniform microstructures with distinct thermal properties and limit assumptions to improve confidence in measurement accuracy. A smoothed inversion procedure transformed the observed granule cross-sections to the true diameters. The ITR and component thermal conductivities were fit by an analytical model to the experimental data measured by light flash analysis. The measured ITR, on the order of 10^{-6} m^2-K/W, was remarkably near reported values fit to continuous BeO microstructures of varied fabrication technique and thermal conductivity improvement. The method applied here reduced uncertainty compared to the existing literature by fitting the thermal conductivity of UO_2 and BeO in application, which were more predictive of the effective thermal conductivity, rather than relying on literature correlations.

With the resulting ITR, an effective thermal resistance model for idealized continuous microstructures was applied to quantify the critical particle diameter to maintain thermal conductivity improvement over UO_2 across operating and accident conditions, given a constant ITR at these temperatures. A lower limit of 100 μm is identified for a 5 vol.% BeO composite and 40 μm for a 10 vol.% BeO composite with the upper diameter set by practical fabrication limits demonstrated as low as 300 μm. The insight reported with high confidence here improves predictions of the composite thermal conductivity and evaluation of the impact of features such as shape and orientation for the BeO network to design the microstructure for improved fuel performance and accident tolerance.

ACKNOWLEDGEMENTS

I would like to express my deepest appreciation to Dr. Sean McDeavitt, my advisor, for his unwavering support and encouragement over the many years and the rest of the members of my committee, Dr. Cagin, Dr. Shamberger, and Dr. Shao for their guidance throughout the course of this research. This endeavor would not have been possible without my current and former colleagues in the Fuel Cycle and Materials Laboratory, especially Dr. Luis Ortega, Dr. Delia Perez-Nuñez, Chad Garcia, and Dr. Brandon Blamer, thank you for the help and reassurance.

I'd like to recognize the Texas A&M University Graduate and Professional School and the Bridge to the Doctorate Program for providing funding for me and my research and many resources to support my professional development along the way.

I also want to extend my sincere thanks to my friends, Kelly and Jessica, for their immense wisdom, humor, and encouragement and for the accountability meetings that continue to this day. Finally, I am so grateful to my family for their understanding, patience, and love during this very long road. I was especially lucky to share this journey with my sister, Jordan, who I am certain will be writing her own acknowledgements soon.

CONTRIBUTORS AND FUNDING SOURCES

Contributors

This work was supervised by a dissertation committee consisting of advisor Dr. Sean McDeavitt and Dr. Lin Shao of the Department of Nuclear Engineering and Dr. Tahir Cagin and Dr. Patrick Shamberger of the Department of Materials Science and Engineering.

The author acknowledges the characterization part of this work was performed in the Texas A&M University Materials Characterization Core Facility (RRID:SCR_022202) under the supervision of Dr. Andrew Mott. The data analyzed in Chapter 4 was conducted in part by the author and Mohammed Gomaa Abdoelatef of the Department of Materials Science and Engineering at Texas A&M University and Fergany Badry, Sean McDeavitt, and Karim Ahmed of the Department of Nuclear Engineering at Texas A&M University and was published in 2019.

All other work conducted for this dissertation was completed by the student independently.

Funding Sources

Graduate study was supported by fellowships from Texas A&M University, including support from the National Science Foundation Award No. HRD-1249272, and by the Department of Materials Science and Engineering at Texas A&M University.

This material is also based upon work supported by the National Science Foundation Graduate Research Fellowship under Grant No. 1252521. Any opinion,

findings, and conclusions or recommendations expressed in this material are those of the author and do not necessarily reflect the views of the National Science Foundation.

TABLE OF CONTENTS

Page

LIST OF FIGURES

Page

LIST OF TABLES

Page

1. INTRODUCTION

A precise description of the thermal properties of nuclear fuel is crucial to the safe and economic operations of a nuclear power plant. An empirical understanding of uranium dioxide fuel thermal conductivity has supported the analysis of light water reactors for decades; however, renewed interest in advanced fuel concepts [1-2] and considerable advances in computational methods have driven the development of physically justified approaches to modeling the thermal performance of nuclear fuel. This work considers the thermal conductivity of uranium dioxide, beryllium oxide and their composite combination as a representative nuclear fuel system. The objective of this research is to measure the interfacial thermal resistance between the composite components by a combined experimental and analytical approach, the flash method, and implement the resistance into an analytical model of the microstructure's thermal conductivity, verified by mesoscale computational models, to contribute to the development of adaptable, physically justified models of nuclear fuel.

Nuclear power plays a vital role in the domestic generation of carbon emission free energy, accounting for over half of clean energy production in the United States. Historically, nuclear research with applications in light water reactor (LWR) power production has focused on improving fuel performance; however, the Fukushima Daiichi nuclear accident highlighted vulnerabilities in the fuel-cladding system employed in commercial nuclear power reactors. Supported by new research initiatives and over half a century of advanced materials development, the central focus in nuclear materials research

shifted to improved safety and performance in beyond design basis accidents (BDBA), such as the loss of active cooling. Through this new lens, renewed interest in underdeveloped fuel forms and cladding materials moved to the forefront of LWR nuclear materials research [1].

The Advanced Fuels Program of the U.S. Department of Energy issued research directives to develop next generation fuels for the current fleet of LWRs (GEN II) and codified the attributes of accident tolerance. The next generation fuel should enhance accident tolerance, as compared to the current uranium dioxide (UO_2)—Zircaloy system, in BDBA, such as a loss of active cooling, increasing the time period before requiring active intervention. While next-generation reactors (GEN III and GEN III+) have design features to improve accident tolerance, GEN II LWRs provide a substantial fraction of the carbon-free energy in the U.S. but are undermined by suppressed prices of competing sources and aging infrastructure. Therefore, in order to motivate vendors and utilities to adopt, the accident tolerant fuel (ATF) must exhibit better safety performance and reliability, more favorable neutronics, and be economically feasible in current fuel configurations [1].

To enhance accident tolerance, four attributes of the cladding and fuel have been identified as follow: reduced hydrogen generation rate, improved fission product retention, reduced cladding reaction with steam, and reduced fuel-cladding interactions. To improve fission product retention in the fuel, fuel technologies were categorized by potential performance benefit and timeline to deployment. High-density fuels, such as uranium nitride and uranium silicide, were classified as having the potential for high performance

benefits but extended time to deployment and more significant vulnerabilities. Alternatively, enhanced UO_2 fuels were classified as having more modest potential for performance benefits but reduced time to deployment with lower risk related to the research vulnerabilities. Despite the differences, research in both fuel categories has proceeded [2].

Of the enhanced UO_2 fuel concepts, one approach considers inserting a thermally conductive additive to the fuel microstructure which has been demonstrated to improve thermal conductivity [1-3]. Rather than selecting a high-density fuel with higher native thermal conductivity, this approach benefits from the operation experience existing for UO_2 fuel in LWR applications, reducing the risk of undiscovered vulnerabilities. With the design and time constraints for ATFs, UO_2-based fuel retains the vast database of experimental support to validate fuel performance modeling [2]. An enhanced UO_2 fuel composite with higher thermal conductivity can lower operating temperatures for the same heat generation rate or allow a power uprate. An increased margin to fuel melting can be achieved through an operating temperature reduction in the fuel. By reducing the temperature gradient across the fuel, thermal-induced stress in the pellet is reduced, potentially reducing cracking and improving fission product retention in the pellet, an attribute of an ATF [1-2]. The thermally conductive additive will, however, displace fissionable material, potentially requiring higher enrichment or reduced burnup.

Materials under consideration as thermally conductive additives have included silicon carbide [3-7], diamond [8-9], alumina [2-3], graphene [10], molybdenum [11-14], Ti_3SiC_2 (MAX phase) [15], and beryllium oxide (BeO) [3,16-17]. This work focuses on a

particular concept refined by A. A. Solomon and his research team at Purdue University wherein large UO_2 microspheres are dispersed within a continuous BeO matrix [3,16]. Beryllium oxide has a high thermal conductivity (370 W m^{-1} $^oC^{-1}$ at 25^{o}C for a single crystal) [18], the primary focus of the additive, and is compatible in nuclear applications. A comparison between the thermal conductivity of dense, polycrystalline UO_2 and BeO is shown in Fig. 1.1 [19-20]. Beryllium oxide has a low thermal neutron absorption cross-section and is chemically stable with respect to the water coolant used in LWRs and the other materials for fuel and support, UO_2 and Zircaloy. Beryllium oxide does not interact with UO_2 until the UO_2-BeO eutectic temperature near 2433 K [21]. Beryllium oxide can be incorporated into the current fuel manufacturing processing stream and sintered with the UO_2 powder to form pellets, eliminating the need for additional manufacturing streams to support a fuel switch [3].

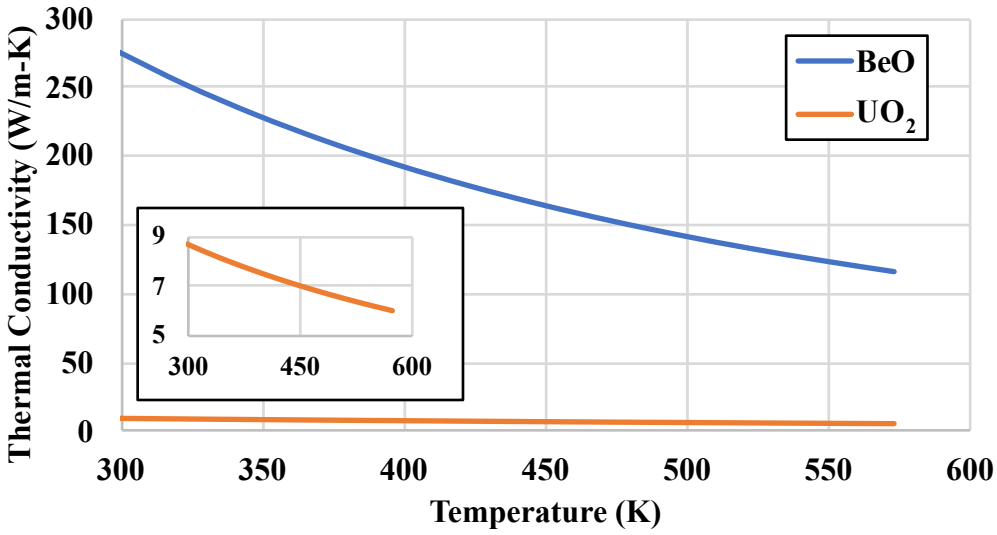

Figure 1.1 A comparison of the thermal conductivity of dense, polycrystalline BeO and UO_2 with a higher resolution inset of the UO_2 thermal conductivity [Adapted from 19-20]

To implement a new fuel form, the physical properties must be well-characterized to enable detailed evaluation of the phenomenological response and system and safety analysis in LWR simulation tools. While LWR fuel performance simulations have shown results consistent with the performance of an accident tolerant fuel for UO_2-BeO composites, the thermal conductivity correlations return the most favorable experimental results, disregarding research fabricated at temperatures aligned with industry processes [22-24]. Previous work developing a model to unify the experimental thermal conductivity results using finite element method representations of the fuel microstructures could not explain the reported experimental physical properties [16]. A systematic review of the impact of the simulation setup on the computed thermal conductivity was not reported. Additionally, other physical properties known to impact heat transfer were not presented.

The work presented here seeks to address these shortcomings in support of a robust description of the composite thermal conductivity and future evaluations of the fuel forms impact on LWR operating conditions. The objective is to quantify the interfacial thermal resistance between conventionally sintered UO_2 and BeO to inform the design and development of the composite fuel. The interfacial thermal resistance has been shown to be a critical parameter in the thermal conductivity of UO_2-BeO composites [16,25-27]. The literature regarding the development of the UO_2-BeO composite fuel form and investigation of models identifying the critical features impacting the composite physical properties are reviewed in Chapter 2.

While previous studies have quantified the magnitude and impact of the interfacial thermal resistance in this composite, the research tended to draw from complex and poorly characterized composite microstructures preventing conclusive results [25-27]. Drawing on the literature review, Chapter 3 presents a suite of complimentary experimental, analytical, and computational techniques to fabricate and characterize the composite microstructure, quantify the interfacial thermal resistance, and implement the results in a mesoscale and analytical model. The combined experimental and analytical flash method is presented to calculate the interfacial thermal resistance using an expression for a composite of dispersed, spherical particulates dependent on the thermal conductivities of the bulk composite, the matrix, and the particulates, the interfacial thermal resistance, the particle radius, and the volumetric fraction of particulate in the matrix [28-33]. The expression is further detailed in Section 2.3. To evaluate the variables within a system of equations, multiple sintering experiments aligned with previous work are carried out to

fabricate microstructures with dispersed, spherical granules of uniform size [3,34]. The thermophysical properties of the composite are characterized by pycnometer, light flash analysis, and scanning electron microscopy. Finally, the methodological approach taken to simulate the microstructure in MOOSE is presented based on the scheme reported by Badry *et al.* [27] and compared to the analytical model reported by Zhu *et al.* [26].

The results from the methodology created to quantify the ITR in UO_2-BeO composites are reported in Chapter 4 and discussed in Chapter 5. Microstructure features observed by scanning electron microscopy were quantified in ImageJ and converted to three-dimensional measurements from the distribution of the sections [35-39]. With the collected experimental data, the interfacial thermal resistance was calculated by the flash method and considered in the context of the existing literature for the composite. Verified analytical models were exploited to determine the critical features of the composite design necessary to achieve the design goals of the fuel. The results were input into mesoscale and analytical models following the scheme reported by Badry *et al.* and Zhu *et al.* to evaluate the impact on the fuel design parameters [26-27].

2. LITERATURE REVIEW

The framework of this literature review considers the state of the research on the fabrication and modeling of uranium dioxide and beryllium oxide composites. Prior investigations of uranium dioxide and beryllium oxide composites, reviewed in Section 2.1, achieved microstructures that improved the bulk thermal conductivity in ways consistent with an accident tolerant fuel. Section 2.2 presents studies simulating the experimental microstructures were inconsistent in accuracy and highlighted the role of the interface in heat transfer. The role of the thermal boundary resistance in these composites has not been conclusively determined, thus theoretical, computational, and experimental methods to quantify the thermal boundary resistance are investigated for this application in Section 2.3.

2.1. Composite Fabrication and Thermal Property Analysis

Ishimoto *et al.* first demonstrated that a UO_2-BeO composite formed by melting above the eutectic temperature at 2473 K could raise the thermal conductivity of the fuel by approximately 60% at room temperature due to the 4.2 vol.% continuous BeO matrix. In contrast, composites sintered below the eutectic temperature resulting in a dispersed BeO microstructure only increased the thermal conductivity around 11% at the same concentration [40]. Over the concentration range below the eutectic mixture studied (1.1 to 4.2 vol.% BeO), a linear relationship was observed between the concentration of BeO and the improvement in thermal conductivity for each microstructure type. For microstructures with a continuous BeO matrix fabricated above 2473 K, the composites

improved the thermal conductivity of UO_2 roughly 14% for every 1 vol.% of BeO at 1100 K. In contrast, microstructures with a dispersed BeO matrix fabricated at 2073 K improved the thermal conductivity of UO_2 roughly 3% for every 1 vol.% of BeO. The continuous and dispersed BeO morphologies, as well as the eutectic mixture, can be compared in Fig. 2.1 demonstrating the influence of the fabrication temperature and BeO concentration on the resultant microstructure. For application as an ATF, the ceramic morphology with an embedded, interconnected BeO network within the UO_2 is critical to the performance enhancement. The dispersed UO_2-BeO structures did not exhibit comparable performance improvement.

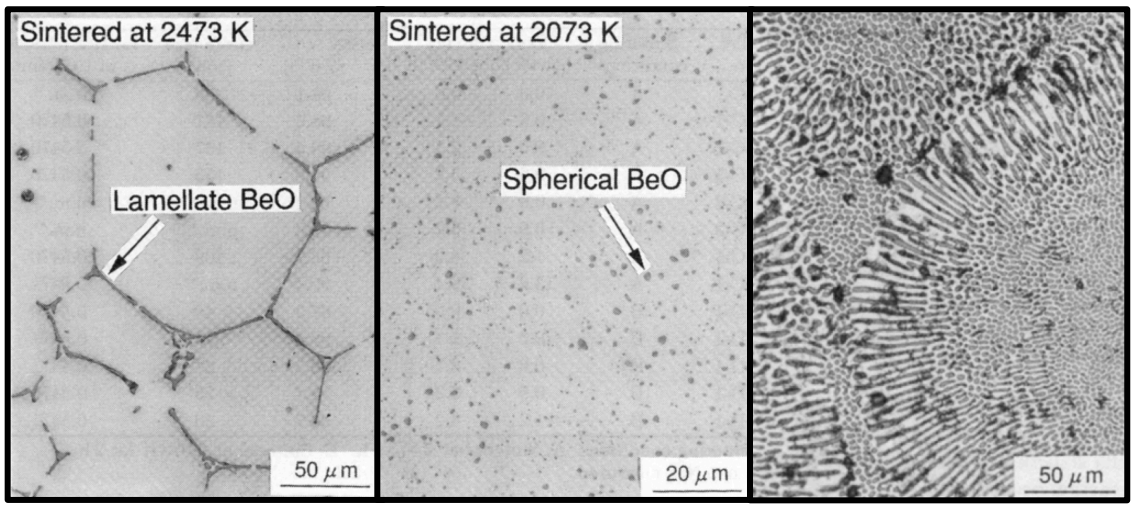

Figure 2.1 Ceramographs of UO_2-3.2 vol.% BeO composites exhibiting a continuous BeO microstructure when processed above the eutectic temperature (left) and a dispersed BeO microstructure when processed below the eutectic temperature (center) and the resultant microstructure by processing the eutectic mixture, UO_2-36.4 vol.% BeO, above the eutectic temperature (right) Reprinted with permission from Taylor & Francis* [40]

* Reprinted with permission from "Thermal Conductivity of UO_2-BeO Pellet" by S. Ishimoto, M. Hirai, K. Ito and Y. Korei, 1996. *Journal of Nuclear Science and Technology*, 33:2, 134-140, Copyright 1996 by Taylor and Francis Group.

Whereas Ishimoto *et al.* processed above the eutectic temperature to achieve the continuous composite microstructure, Sarma *et al.*, led by A.A. Solomon at Purdue University, sought to align the production process with industry practices. To reduce processing temperatures, Sarma *et al.* showed similar improvements could be made by co-sintering UO_2 granules pre-coated with BeO powder at 1973 K, 500 K lower than the temperature used by Ishimoto *et al.* to achieve a continuous BeO microstructure [3,40]. The work compared a green granules and slug bisque manufacturing procedure, differing in the starting condition of the UO_2 granules. The green granules method used pre-compacted granules of UO_2 powder coated in BeO to form a final compact for co-sintering. While the green granules method used pre-compacted granules, the slug-bisque method coated pre-sintered UO_2 granules in BeO. As shown in Fig. 2.2, the resulting microstructures differ in the extent of BeO uninterrupted by UO_2. In contrast to the uninterrupted BeO matrix formed by the slug-bisque method, the green granules method resulted in a BeO matrix containing 24 vol.% UO_2. Despite the processing and microstructural differences, both methods demonstrated similar improvements in the thermal conductivity over UO_2 and achieved pellet densities >90%TD [3,16]. As an illustration of the continuous BeO network, the UO_2 was dissolved away from a UO_2-BeO composite pellet using nitric acid to reveal the BeO as a mechanically robust, continuous network [3], a requirement for performance improvement noted in the work of Ishimoto *et al*. [40]. A composite pellet and the illustration of the continuous BeO network are shown in Fig. 2.3 [3].

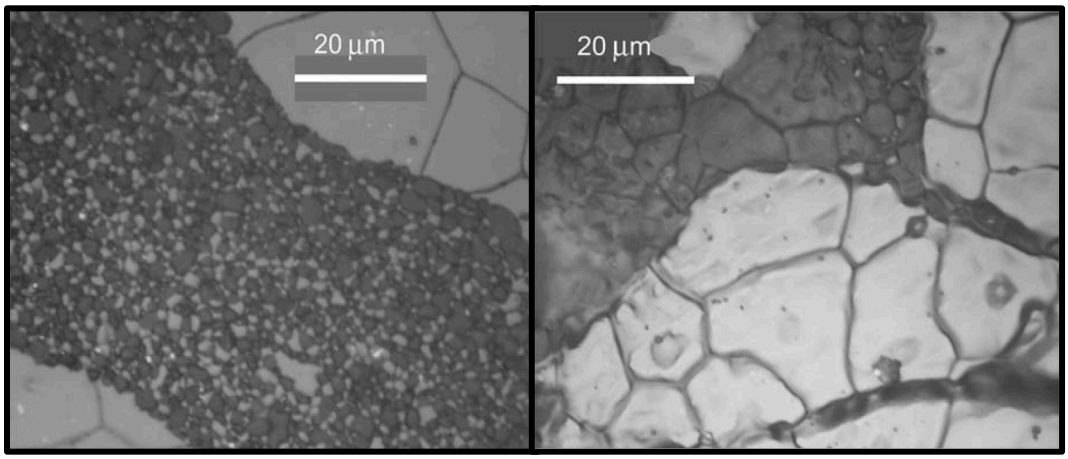

Figure 2.2 SEM micrographs of the resultant microstructures of the green granules (left) and slug-bisque (right) manufacturing methods where light regions are UO_2 and dark regions are BeO, Reprinted with permission from Elsevier* [3]

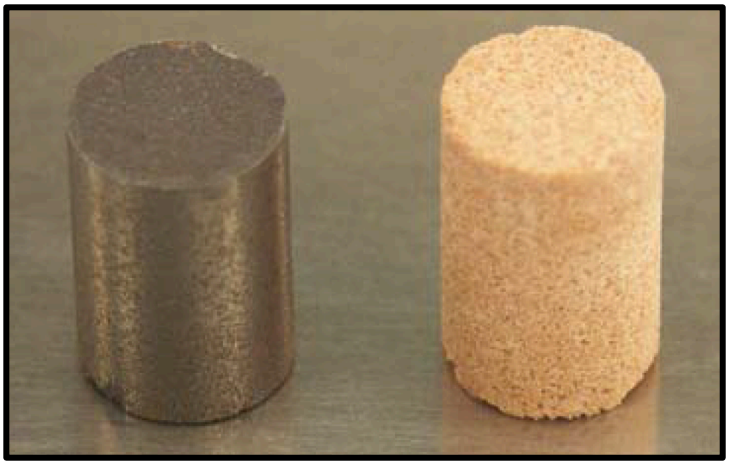

Figure 2.3 A UO_2-BeO composite pellet (left) and the continuous BeO network after the UO_2 was dissolved away using nitric acid, Reprinted with permission from Elsevier* [3]

Using the green granules production method, Garcia *et al.* at Texas A&M University produced UO_2-*x* BeO samples (*x*=2.5, 5, 7.5, 10 vol.%) to enable an evaluation of the enhancement achievable by a BeO matrix using samples manufactured from the

* Reprinted with permission from "New processing methods to produce silicon carbide and beryllium oxide inert matrix and enhanced thermal conductivity oxide fuels" by K.H. Sarma, J. Fourcade, S-G. Lee, and A.A. Solomon, 2006. *Journal of Nuclear Materials*, 352, 324-333, Copyright 2006 by Elsevier.

same source materials, using identical processing parameters, and targeting the range of interest for an ATF [34]. The addition of BeO displaces UO_2 fuel volume, requiring higher enrichment of U-235 to maintain the number density, guiding the range of BeO concentrations of interest. The achieved microstructures were similar to those seen by Sarma *et al.* for the green granules method, as shown in Fig 2.4, although the BeO matrix contained less fine UO_2, 16 vol.% as measured by quantitative stereology, likely due to differing BeO powder features [3,34]. The thermal conductivity results indicated that the thermal conductivity of UO_2 improved approximately 10% for each 1 vol.% of BeO added [34]. Compared to the results for samples fabricated by Sarma *et al.* and reported by Latta, Revankar, and Solomon., Garcia *et al.* attained a thermal conductivity 7% higher at the 10 vol.% BeO concentration as measured at 473 K [3,16,34]. Microstructure differences may explain the magnitude of improvement in the thermal conductivity for this composite.

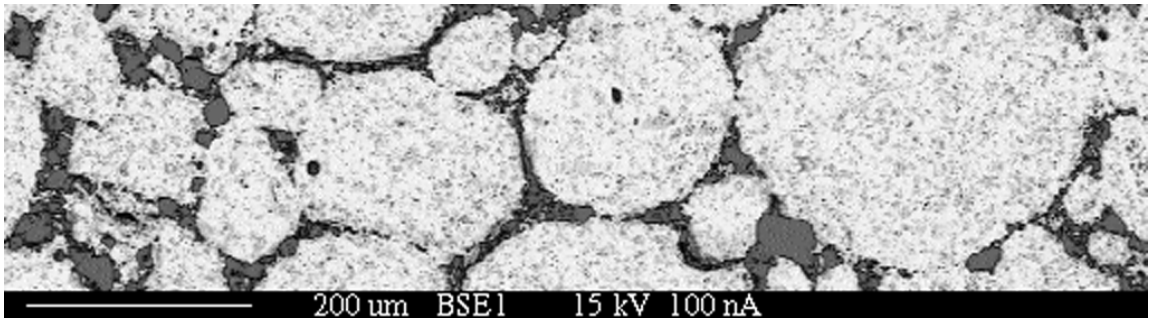

Figure 2.4 Representative SEM micrograph of the UO_2-BeO microstructures fabricated by Garcia *et al.* Reprinted with permission from Springer Nature* [34]

* Reprinted with permission from "Manufacture of a UO_2-Based Nuclear Fuel with Improved Thermal Conductivity with the Addition of BeO" by C. Garcia, R. Brito, L. Ortega, J. Malone, and S. McDeavitt, 2017. *Metallurgical and Materials Transactions E*, 4E, 70-76, Copyright 2017 by Springer Nature.

Recently, Li *et al.* at the China Academy of Engineering Physics Institute of Materials demonstrated the fabrication of a UO_2-BeO continuous microstructure using spark plasma sintering and characterized the composite's coefficient of thermal expansion up to 2273 K and thermal conductivity up to 1873 K [41]. Further analysis reported by Gao *et al.* on the spark plasma sintered composite found that the porosity of the BeO matrix was 26.97% [25], masked by the low concentration of BeO and the high overall density of the composite. The density of the BeO matrix was identified as a critical parameter to the performance enhancement; however, the density alone could not account for the reported thermal conductivity. As also reported in literature discussed later [16,27,34], an *interfacial thermal resistance* on the order of 10^{-6} to 10^{-5} m^2-K/W was necessary to align analytical expressions for the thermal conductivity with the experimental results. The behavior of composites fabricated by pressureless sintering reported by Gao *et al.* supported these conclusions [25].

Together the works of Ishimoto *et al.*, Sarma *et al.*, Garcia *et al.*, Li *et al.*, and Gao *et al.* demonstrate that the thermal conductivity of UO_2 can be improved with the addition of BeO by a variety of production methods and without significant disruption to current manufacturing procedures. The reported enhancements from these investigations, normalized by the volumetric concentration of BeO in a continuous microstructure, are shown in Fig. 2.5. As shown, a broad range of improvement has been reported for continuous UO_2-BeO composite microstructures with investigations into the basis of the divergence being actively pursued both in this work and in published literature. While absent of fabrication method and microstructure details, the data suggests that significant

improvements in thermal conductivity are achievable with improved understanding of the critical parameters differentiating the experimental results and by applying informed design to the composite microstructure. This is a foundational premise motivating this present work.

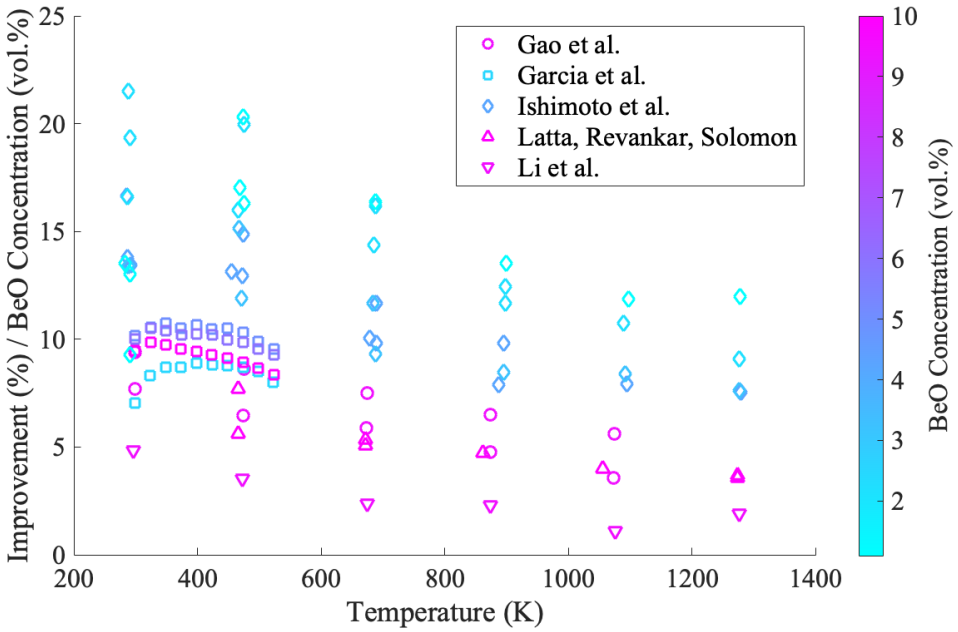

Figure 2.5 Comparison of the reported literature on the thermal conductivity improvement of UO_2 with a continuous BeO microstructure, normalized by the concentration of BeO indicated by the symbol color corresponding to the color bar legend on the far right [Adapted from 16,25,34,40-41]

2.2. Simulation of Fuel Performance and Microstructure

The fabrication of uranium dioxide and beryllium oxide composites with improved thermal properties has motivated further study into the impacts on heat transfer and fuel performance in nuclear reactors. To evaluate phenomenological impacts, the improved properties must be implemented in a multiscale, multiphysics nuclear simulation code. The experimental results provide a basis for the development of empirical equations for

the composite thermal conductivity for input into LWR simulation tools. This section reviews results of fuel performance analyses for UO_2-BeO composites, emphasizing that, compared to the results shown in Fig. 2.5, meaningful fuel performance enhancement and improved accident tolerance can be realized with the improvements achievable with an informed design of the UO_2-BeO microstructure.

To scope the system impact of a fuel switch from UO_2 to a high conductivity composite, several investigations have implemented empirical expressions for the composite fuel thermal properties. In a fully coupled multiphysics analysis of UO_2-BeO composite fuel performance in COMSOL-based framework CAMPUS, Liu *et al.* implemented physical properties for 2.1, 4.2, and 36.4 vol.% BeO concentrations in UO_2 fuel. COMSOL is a coupled, multiphysics simulation software, solver, and finite element analysis package within which the CAMPUS framework was developed to host multiple user-defined physical models for simulating UO_2-BeO composite fuel performance. The empirical relationship between the thermal conductivity and temperature used was

$$k(T) = k(UO_2 - BeO) \cdot f_d \cdot f_p \cdot f_{por} \cdot f_x \cdot f_r. \quad (1)$$

The composite thermal conductivity for each BeO concentration was determined by fitting the coefficients of the physically based thermal conductivity equation for UO_2 given by

$$k(UO_2 - BeO) = \left(\frac{1}{A+BT} + \frac{E}{T^2} e^{-F/T}\right)\left(\frac{1}{1-0.05(2.6-0.0005T)}\right) \quad (2)$$

to the data obtained by Ishimoto *et al.* [24,40] and correcting the porosity to fully dense. The factors f_d, f_p, f_{por}, f_x, and f_r in Eq. 1, applied to roughly account for the influence of dissolved and precipitated fission products, porosity, stoichiometry, and radiation damage on the thermal conductivity of the composite, were developed by Lucuta, Matzke, and

Hastings for traditional LWR UO_2 fuel throughout burnup, although the relevance of the factors to the composite fuel was not verified in the reported work [42]. The density and specific heat for the composite were determined by mass and volume-weighted averaging as appropriate which has been shown to accurately reflect the composite properties [34]. Additional material properties and model implementation were consistent with practices in use in BISON, ABAQUS, and FRAPCON, and the simulation capability of CAMPUS was verified and validated against the fuel behavior predicted by those of standard nuclear evaluation codes [24].

The results of the analyses showed the fuel with enhanced thermal conductivity reduced the centerline fuel temperature by roughly 120 – 140 K over the fuel lifetime at the lower concentrations of BeO studied and applicable to the current proposed work. The fuel change also delayed gas gap closure, reduced fission gas release, and decreased plenum pressure which may facilitate a reduction in pellet cladding interaction by lessened thermal stresses that result in fuel cracking, relocation, and swelling. For the lower concentrations of BeO, during normal operation, the calculated fission gas release was reduced by almost 40% [24]. Although the work only assessed conditions under normal operation, these results are consistent with the goals of an accident tolerant fuel and demonstrate impacts on reactor operations motivating to vendors and utilities.

In an analysis by Chandramouli and Revankar. in FRAPTRAN (Fuel Rod Analysis Program Transient), the simulated performance of UO_2 and a UO_2-10 vol.% BeO composite were compared to experimental data for UO_2 for non-normal operating conditions in steady-state and transient cases [43-44]. FRAPTRAN calculates the transient

performance of oxide fuel rods during reactor transients and accident scenarios. For the thermal conductivity of a UO_2-BeO composite, the expression for the thermal conductivity of UO_2 with gadolinium oxide was refit to the data provided by Ishimoto *et al.* [23,40]. The empirical relationship between the thermal conductivity and temperature used was

$$k\left(T_n = \frac{T}{1000}\right) = \frac{1}{0.0375+0.2165T_n-0.034248-0.315VT_n} + \frac{4750}{T_n^2} e^{-16.361/T_n}, \qquad (3)$$

where V is the percentage of BeO. The thermal properties were implemented in MATPRO. Similar to other works, the density, specific heat, and enthalpy for the composite were calculated by mass or volume-weighted averaging as appropriate.

For the steady-state, normal operating conditions case, Chandramouli and Revankar reported results consistent with those reported by Liu *et al.*—a reduction in the centerline temperature and in plenum pressure (3.55% for 10 vol.% BeO). To study steady-state, abnormal operating conditions cases, two cases were considered, a two-phase coolant at the inlet with constant temperature but increasing quality and a coolant with low flow rates forming steam near mid-height. In both scenarios, the enhanced thermal conductivity fuel reduced centerline temperatures (200 to 230 K). For the first case, the plenum pressure was also reduced by 3.6%; however, in the second case, no change in plenum pressure was predicted. The elastic cladding strain is excessive in this case and dominates in contribution to the overall plenum pressure. Finally, in the modeling of a transient reflood and cladding rupture, a smaller reduction in centerline temperature was observed (40 K) and a more significant reduction in cladding strain following rupture, as compared to the FRAPTRAN simulated results and the experimental data obtained by

Geelhood *et al.* [44]. Importantly, in all of the cases the total energy stored in the fuel was significantly reduced when the enhanced thermal conductivity fuel was implemented [23].

In an investigation into the fuel performance during a LOCA simulated in RELAP5 (Reactor Excursion and Leak Analysis Program), Revankar, Zhou, and Chandramouli compared UO_2 and UO_2-10 vol.% BeO fuels in steady-state operation and in transients with and without SCRAM and water injection. RELAP5 couples the behavior of the reactor coolant system and core to simulate transients and accident scenarios [44-46]. The thermophysical properties used were identical to those applied by Chandramouli and Revankar [23]. During normal, steady state operation, Revankar, Zhou, and Chandramouli reported a near 20% decrease in maximum fuel rod temperature comparing conventional UO_2 to an enhanced thermal conductivity composite, from 1561 K to 1244 K, a 323 K decrease [22]. For comparison, Liu *et al.* calculated a 120 to 140 K decrease for 2.1 and 4.2 vol.% BeO composites [24]. For both LOCA scenarios, with and without SCRAM and water injection, the composite fuel demonstrated lower centerline temperatures of similar magnitude to normal operation; however, the lower temperatures did not translate to a significant change in the reactor vessel pressure or void fraction in either scenario.

In contrast to the previously described approaches, McCoy and Mays [47] opted to simulate a 5, 10, and 50% increase in thermal conductivity in COPERNIC, AREVA's proprietary fuel performance code, to represent 4.0 vol.% and 9.6 vol.% of BeO in UO_2. The simulated thermal conductivity enhancement was not associated with experimental data, rather an evaluation of the impact of an improvement in the thermal conductivity on fuel performance. Notably, the authors report that an improvement as low as 5% had

signification benefits on the scale of the spread in the experimental data shown above in Fig. 2.5. Similar to the previously discussed results, a 50% increase in thermal conductivity was associated with a decrease in the volumetric-averaged fuel temperature (122 K), fission gas release (4.5%, down from 19.6%), and internal pressure (9.1 MPa) at the end of the projected fuel lifetime. The improvement also yielded significant improvements in LOCA behavior [47].

The fuel performance analyses have shown that the enhanced thermal conductivity of the composite reduces fuel temperatures which in turn reduces fission gas release and plenum pressure. This behavior has the potential to improve power generation and extend fuel burnup and is consistent with expectations for an accident tolerant fuel; however, as discussed below, an empirical fit procedure used in much of the previously described work can overgeneralize the complexity in microstructure. As noted by Li, Garmestani, and Schwartz, especially in legacy codes, the thermal conductivity correlations often neglect the influence of the microstructure, relying on the isotropic properties of the fuel. This assumption hinders the prediction of the thermal conductivity and of coupled phenomena in fuels with engineered microstructures and preferred anisotropic properties [48]. While an empirical fit is specific to the experimental setup, microstructural simulations and physically justified models are adaptable and potentially more suitable to the microstructures observed experimentally for UO_2-BeO composites. The remainder of Section 2.2 reviews approaches undertaken to compute the composite thermal conductivity using simulated microstructures, highlighting that there is a demonstrated need for additional experimental data to support the fuel development.

While the literature largely computes the thermal conductivity of UO_2-BeO composites with explicitly defined geometries in an FEM mesh, Li, Garmestani, and Schwartz applied a statistical approach to scope the achievable improvements in thermal conductivity for anisotropic microstructures with a high conductivity component [16,48-49]. When applied to the UO_2-BeO composite system at room temperature, the model could predict an improvement in the effective thermal conductivity, spanning 0 to 100 vol.% BeO, for isotropic and anisotropic microstructures. Even in isotropic, dispersed microstructures, the model predicted effective thermal conductivities approaching the theoretical upper limit for composite thermal conductivity where the conducting phase is oriented completely parallel to the heat flow, although an improvement of this magnitude has not been observed experimentally. Comparing isotropic to increasingly anisotropic microstructures, Li, Garmestani, and Schwartz showed the effective thermal conductivity could be improved by a further 4 to 6% in the direction of preferred anisotropy at the expense of the other direction (the simulations were two-dimensional, although the framework for three-dimensions is outlined) [48]. The results highlight the potential achievable improvement predicted by simulations of the composite microstructure and of engineered preferred anisotropy in the microstructure.

In contrast to the statistical formulation of the composite microstructure used by Li, Garmestani, and Schwartz, Zhou *et al.* constructed two-dimensional and three-dimensional FEM meshes in ANSYS to represent the continuous microstructures observed experimentally, using the data collected by Ishimoto *et al.* as a benchmark. The

temperature distribution across the simulated microstructure was determined by solving the Fourier heat conduction equation at the nodes of the FEM mesh which takes the form

$$q_x^{"} = k\frac{T_{i+1}-T_i}{l}, \quad (4)$$

where $q_x^{"}$ is the applied heat flux, k is the thermal conductivity, and T_{i+1} and T_i are the temperatures at nodes $i+1$ and i, respectively. The effective thermal conductivity over the simulated domain of the composite was then calculated by averaging the resulting temperature distributions at the boundaries and solving

$$k_{effective} = q^{"}\frac{dx}{dT}, \quad (5)$$

where $k_{effective}$ is the effective thermal conductivity of the composite domain, $q^{"}$ is the applied heat flux, dx is the known simulation dimension, and dT is the resulting temperature difference across the domain calculated by Eq. 4. All of the simulations executed were within 10% of the experimental measurements reported by Ishimoto *et al.*, regardless of the mesh dimension or geometry, although, accuracy did improve with increasing BeO concentration and temperature [40,49]. As noted by Zhou *et al.*, the uniformity across the simulation dimension concurs with Boey *et al.* who used similar geometries with different assigned material properties to describe the effective thermal conductivity of an aluminum nitride and yttria composite [49-50]. When the approach was extended to concentrations of BeO not reported by Ishimoto *et al.* and the effective thermal conductivity implemented in a COMSOL simulation of a fuel pellet, the fuel performance simulations were consistent with previous work showing a reduction in centerline temperature and the temperature gradient [49].

Latta, Revankar, and Solomon expanded the set of experimental data used to benchmark the simulated microstructures to include the microstructures reported by Sarma *et al.* for UO_2-SiC and UO_2-BeO [3,16]. The microstructures were simulated and the effective thermal conductivity calculated in ANSYS similarly to Zhou *et al.* and were validated against the results for Ishimoto *et al.* within the error of the experimental data [16,40,49]. When applied to the co-sintered microstructures demonstrated by Sarma *et al.*, the model resulted in 9 to 19% error, varying with temperature. A factor reducing the thermal conductivity of the BeO component by 30% improved the agreement between the model and experimental results. Similar to Gao *et al.*, the authors identified the composite interfaces and component properties in application as the source of error [16,22,25]. Recalling the spread in the reported enhancement shown in Fig. 2.5, the features could improve understanding of the underlying differences.

The simulation of the fuel performance and composite microstructure point to the recognized potential for BeO to be used as an enhancement for UO_2 nuclear fuel. Both the experimental and computational results demonstrate notable increases in the thermal conductivity which translate to fuel performance benefits consistent with the behavior of an accident tolerant fuel; however, simulation improvements may be achieved to enable a physical basis for the calculations. This is the motivation for the present study that seeks to characterize the *interfacial thermal resistance* between UO_2 and BeO.

2.3. Quantifying the Interfacial Thermal Resistance

Awareness of the thermal boundary resistance is not recent, having first been observed in 1936 but not quantified until Kapitza in 1941 between copper and liquid

helium, hence the namesake Kapitza resistance [51-53]. Reserving the terminology Kapitza resistance for solid-liquid helium boundaries, a similar phenomenon has been observed at other boundaries termed the *thermal boundary resistance*. While smaller in magnitude and less well-defined phenomenologically, the solid-solid thermal boundary resistance has become increasingly significant in nanoscale structures, thin-films, superlattices, and composite materials [16, 54-57]. In addition to the thermal boundary resistance resulting from differences in component physical properties, a *thermal contact resistance* can result from microstructural features at the interface, such as poor mechanical or chemical bonding [58-59]. The synergistic contributions of the thermal boundary resistance and the thermal contact resistance act together and may be termed the *interfacial thermal resistance* [58]. The interfacial thermal resistance has been shown to impact bulk heat transfer depending on the magnitude of the resistance and boundary density [54].

Research computing the thermal conductivity of simulated microstructures has emphasized that critical features of the composite microstructure are absent from the simulations. The interfacial thermal resistance has been identified as a candidate feature due to its role in understanding heat transfer in other composite systems and recent work has confirmed this. This section reviews the theoretical, computational, and experimental and analytical methods for computing the contributions to the interfacial thermal resistance to justify the selection of a combined experimental and analytical method for this application. Contemporary results investigating the interfacial thermal resistance for this composite are reviewed to feature the improvements to accuracy proposed here.

These techniques have been applied to several material systems demonstrating reasonable agreement amongst them and identifying trends and domains in which features demonstrate dominance in their impact on the bulk behavior. For example, experimental investigations have confirmed the theoretical prediction that the *thermal boundary resistance* is temperature independent above room temperature, or above and near the component Debye temperatures [55-56,60]. Experimental measurements of the *interfacial thermal resistance*, however, have shown a temperature dependence [58]. This result suggests a more dominant role of the effect of differential thermal expansion at the boundary on the contribution of the *thermal contact resistance*. Incorporating the interfacial boundary resistance into composite thermal conductivity models is crucial to capturing the scope of these effects and improves the model flexibility.

Early theoretical approaches to understand the temperature discontinuity at the liquid helium interface and at low temperature solid-solid interfaces resulted in two bounding theories, the acoustic mismatch (AM) model and the diffuse mismatch (DM) model [61-64]. The major difference between the two theories is the assumption regarding the behavior of phonons at the boundary. The AM model assumes phonons undergo only specular reflection and transmission, not scattering, and the probability of transmission related to the acoustic impedance of the materials [61]. In contrast, the DM model assumes all phonons diffusely scatter at the interface, and the probability of scattering across the boundary is related to the density of phonon states [61,64]. Several additional assumptions are shared between the two models: heat is conducted primarily by phonons such as in nonmetals; acoustic phonons are the primary conduction mode as occurs at temperatures

under 10 K; the bulk behaves as if defect-free such that phonon interactions occur only at the interface and phonon propagation is well-behaved; and the interface is ideal [62]. The bounding models reasonably predict solid-solid interface thermal boundary resistances within the limits of the models' assumptions and additional work has incorporated the effects of interface roughness, inelastic scattering, and higher temperatures [65].

As computing capabilities have developed, additional theoretical expressions have been proposed to predict the thermal boundary resistance supported by lattice dynamics (LD)-based models. By using LD to provide data to calculate the transmission probabilities, the approach accounts for the atomic detail and forces acting across the interface and does not rely on the Debye approximation for the phonon dispersion curves, shortcomings in the AM and DM models. Thus, this approach can be applied to higher temperatures without the use of fitting parameters determined from experimental data as used in the modified AM and DM models [66-67]. With the atomic-scale resolution at the boundary, results of this approach are sensitive to the forces assumed at the interface and the resulting equilibrium positions [67]. Similar to the AM and DM models, the LD-based model was reasonably accurate within the limits of the model's assumptions. When compared to the calculation of the thermal boundary resistance made by molecular dynamics (MD), discussed later, the LD-based model diverged at higher temperatures as inelastic scattering introduced additional modes of heat transfer at the interface [66].

Similar to LD simulations, MD resolves the atomic detail of the lattice and the forces acting across the interface. As stated for LD, the interface structure is sensitive to the forces, or potentials, assumed for the atoms and the resulting equilibrium positions. To

accurately predict thermal transport in MD, a potential should be selected which describes the material elastic properties, phonon dispersion curves, yield strength, and thermal expansion coefficients [68]. While LD assumes vibrational modes are harmonic and applies an analytical solution to the equations of motion based on the selected potentials, MD applies a numerical solution and makes no assumptions regarding the phonon interactions [68-69]. Unlike theoretical and computational methods discussed previously, MD simulations are also valid at and above the Debye temperature [68]. These distinctions have helped classical atomistic simulations quantify the thermal boundary resistance more accurately and at higher temperatures. Chen *et al.* demonstrated the use of MD to calculate the grain boundary resistance in unirradiated UO_2 and with defect structures induced by simulated ion irradiation [70-71]. While the simulation domain and time scales are limited, MD simulations can probe individual microstructural contributions to the thermal transport which cannot necessarily be separated from competing phenomena experimentally, but constructing the bulk thermal transport *a priori* remains challenging.

For UO_2-BeO interfaces, the thermal boundary resistance has been calculated using the AM and DM models. Liu and Zhou incorporated the thermal boundary resistance calculated by the AM model into several fuel microstructure geometries modeled in CAMPUS [72]. Using an estimation by Swartz and Pohl for the interfacial thermal conductance and calculating the phonon velocities by the method provided by Da Silva and Kaviany using values reported by Wang *et al.* for UO_2 and Riou *et al.* for BeO [73-75], the thermal boundary resistance was reported on the order of 10^{-9} m^2-K/W over the temperature range 400 K to 2000 K. Similar to Latta, Revankar, and Solomon, however,

a factor of 1.13 was necessary to adjust the dispersed analytical model utilized and account for the interconnected BeO network. It is highly desirable to develop a more robust and physically justified approach to model the effective thermal conductivity of the composite microstructure to support the develop, design, and evaluation of the fuel and help identify the critical features contributing to the varying thermal conductivity improvements reported in Fig. 2.5.

Zhu *et al.* theoretically determined the thermal boundary resistance on the scale of 10^{-9} m^2-K/W, similar to Liu and Zhou, using the diffuse mismatch model (DMM) based on the full-band phonon dispersions calculated by density functional theory (DFT). When the analytical model used in the paper was compared to the experimental results reported by Ishimoto *et al.* and Badry *et al.*, the data reported by Ishimoto *et al.* for dispersed microstructures indicated the thermal boundary resistance had an insignificant influence on the composite thermal conductivity. The data reported by Badry *et al.* could be fit to the theoretical thermal boundary resistance, if the BeO granules were smaller than 100 nm which, as discussed later, was not the case [27]. In the continuous microstructures, however, the thermal boundary resistance was a non-negligible contributor to the effective thermal conductivity of the composite. The value calculated by the DM model was not sufficient to predict the experimental composite thermal conductivity indicating the vibrational mismatch between the components was not the dominant mechanism impeding heat transfer across the boundary [26].

The theoretical and computational methods discussed thus far provide approaches to compute the thermal boundary resistance but have limited functionality to quantify the

thermal contact resistance, noted as a potential contributor to the interfacial thermal resistance in UO_2-BeO composites by Zhu *et al*. The AM, DM, and LD models assume the thermal contact resistance is negligible, either disregarding or addressing by fit to experimental data factors such as local atomic disorder, lattice distortions, interdiffusion, oxidation, and incomplete bonding [58,65-67]. While MD can incorporate some of these phenomena into the boundary simulation [65,70], as stated previously, it is challenging to construct a simulation representative of the actual boundary. Composites often feature imperfect boundaries which increase the overall interfacial thermal resistance. To measure this additional contribution to the resistance to heat transfer across the composite boundaries, several experimental methods have been successfully utilized to measure the interfacial thermal resistance directly and indirectly. Additional experimental methods exist to measure the thermal boundary resistance directly and validate computational results.

As reviewed by Pietrak and Wiśniewski, the experimental methods to interrogate thermal transfer at composite boundaries can be classified based on the fabrication of the composite boundary. The first classification of methods uses samples of the same components to mimic the target boundary but different fabrication methods, geometries, and/or dimensions to enable the direct measurement of the thermal boundary resistance. The alternate fabrication can create a better bonded boundary and is ideal for direct measurements of the thermal boundary resistance to validate computational methods [58]. Of this classification of experimental methods, however, many can be excluded from this review due to lack of applicability. For example, methods such as the Swartz and Pohl

method [64] and transient [76] and modulated thermoreflectance [77] require one component to be metallic and vapor-deposited as a film, and the hot wire method [78] requires an electrically conductive component embedded in a non-conductive matrix. Methods such as the macromodel method and flash method, however, are compatible with the dual ceramic component system under study here.

The macromodel method probes an enlarged interface between the composite components which can be visualized as sandwiched, but bonded, discs under a temperature gradient. At this scale, the net resistance of the system in steady-state is the simple sum of the thermal resistance of each part in series [79]. The approach assumes the thermal boundary resistance measured by the macromodel method is the same as the interfacial boundary resistance in the in-application composite, an assumption not supported by the literature in all cases, although the dependence varies by composite system and dimension in application [54,58,78].

The flash method uses a pulsed light or laser to heat one side of a thin sample and remotely measures the temperature rise on the opposite side with an infrared camera. The thermal diffusivity of the sample is calculated from on the half-rise time of the recorded temperature signal as proposed by Parker *et al.* and improved on by Cowan [80-81]. The thermal conductivity (k) of the sample can be calculated from the thermal diffusivity (α) using the equation

$$k = \alpha \rho c_p, \tag{6}$$

when the density (ρ) and specific heat (c_p) are known. Depending on the fabrication of the sample, this method can be categorized as either of the two classifications of methods

to experimentally measure the thermal boundary resistance. If the samples are fabricated similar to the macromethod, the thermal diffusivity and interfacial thermal resistance can be calculated by the flash method by either treating the sample as homogeneous, varying the thickness of one component, and interpolating the composite trend to zero thickness to determine the thermal boundary resistance [82-83] or using the flash software models for two- or three-layer samples [84-87]. Similar to the macromodel method, this approach assumes the thermal boundary resistance in the layered sample is the same as the interfacial thermal resistance in-application.

Alternatively, the flash method can be applied directly to a composite with the same fabrication procedure, geometry, and dimension, the second classification of methods to measure the interfacial boundary resistance. Within this classification, the interfacial thermal resistance, the sum of the thermal boundary resistance and the thermal contact resistance, is measured. By measuring the interfacial thermal resistance while maintaining linkage to the desired application microstructure, these methods capture the role of incomplete mechanical or chemical bonding, corrosion, and interdiffusion inherent to the fabrication and in application [58]. Similar to the previous methodology, the flash method measures the effective thermal diffusivity of the composite which can be converted to thermal conductivity by Eq. 6. To determine the interfacial thermal resistance, the data is fit to an analytical model for the composite effective thermal conductivity. The selection of an analytical model restricts the microstructural features incorporated into the calculation of the interfacial thermal resistance, such as inclusion shape and size, and must be selected appropriately for the composite of interest.

A final method to quantify the interfacial boundary resistance is the semi-intrinsic thermocouple method [58]. In this method, a feature of interest on an exposed surface of the sample, such as an inclusion in the composite matrix, is coated in a thin nickel film. A thin platinum wire completes the thermocouple and interrogates the temperature along the film. The inclusion is then heated by a modulated laser and the phase lag recorded by the thermocouple at known distances from the input. Using a theoretical model to account for the shape of the inclusion, the interfacial thermal resistance can be calculated.

While the experimental approaches of interest in this work cannot resolve the physical processes at the boundary, the measurements effectively average the contributions to the boundary resistance of all interface features, a functionality not currently available in theoretical approaches or those supported by lattice- or molecular-dynamics. As indicated by Zhu *et al.*, the vibrational mismatch is not the dominant mechanism impeding heat transfer in the UO_2-BeO composites reported in literature; thus, the experimental measurement of the interfacial thermal resistance should suffice for application in mesoscale simulations of the microstructure and the corresponding analytical models.

As stated previously, when composite boundary morphologies are more complex than simple planes, analytical models for the composite effective thermal conductivity are used to determine the interfacial thermal resistance. The transport properties—thermal conduction, of interest here, electrical conduction, electrostatics, and magnetostatics—share analogous predictive models for the effective properties of heterogenous materials; thus, the topic has been of historical, interdisciplinary interest. Maxwell proposed in 1873

an analytical expression to model electrical conduction in heterogeneous materials with *dilute, spherical inclusions* given by

$$\frac{k_{eff}}{k_m} = 1 + \frac{3f}{\frac{k_p+2k_m}{k_p-k_m} - f}, \tag{7}$$

where k_{eff}, k_m, and k_p are the thermal conductivities of the bulk composite, the matrix, and the particulates, respectively, and f is the volumetric fraction of particulate in the matrix [88-90]. Bruggeman and later Landauer applied a differential approach to deriving Maxwell's expression and was able to expand beyond dilute, closed, and isolated porosity to open, interconnected porosity in a physically justifiable way [91-92]. Nielsen further incorporated an ellipsoidal pore shape and orientation into the analytical prediction of the effective thermal conductivity [93]. Unlike empirical or semi-empirical expressions, the models discussed are physically justified in their development and are thus adaptable and flexible in their usage [94].

Hasselman and Johnson and Benveniste and Miloh independently developed expressions for the effective thermal conductivity of composites, incorporating the interfacial thermal resistance into predictions, using a Maxwellian-approach and based on a micromechanical model, respectively [28-31,95]. While Hasselman and Johnson's approach assumed dilute, spherical inclusions similar to Maxwell, Benveniste extended to non-dilute concentrations of spherical particulate inclusions [28-30]. Every *et al.* applied the differential approach used by Bruggeman and Landauer to integrate the interfacial boundary resistance for composites with isolated and connected second phases [33,91-92]. In their development, the aforementioned models explicitly feature the particulate size,

highlighting that only when the interfacial thermal resistance is considered does the bulk thermal conductivity vary with particulate size for the same concentration and explicitly linking these two properties. In addition to size, Nan *et al.* developed a more general approach using multiple-scattering theory for arbitrary ellipsoidal shapes and orientations in dilute concentrations [31-32]. Whereas there is variability in the predictions of the models in complex microstructures or non-dilute conditions, for dilute, spherical particulate inclusions, all of the models yield the same expression

$$\frac{k_{eff}}{k_m} = \frac{k_p\left(1+\frac{2k_mR_k}{r}\right)+2k_m+2f\left[k_p\left(1-\frac{k_mR_k}{r}\right)-k_m\right]}{k_p\left(1+\frac{2k_mR_k}{r}\right)+2k_m-f\left[k_p\left(1-\frac{k_mR_k}{r}\right)-k_m\right]}, \tag{8}$$

where k_{eff}, k_m, and k_p are the thermal conductivities of the bulk composite, the matrix, and the particulates, respectively, R_k is the interfacial thermal resistance, r is the particulate radius, and f is the volumetric fraction of particulate in the matrix [28-31,33]. If there is no interfacial thermal resistance, Eq. 8 reduces to Eq. 7, consistent with the results of Maxwell [88]. The analytical model described by Eq. 8 and the associated assumptions guide the fabrication, characterization, and analysis performed in the present work.

In an application of the analytical and experimental methods, Zain-ul-abdein *et al.* analyzed composites of opposing behavior with increasing concentration of more conductive particulate inclusions. Analytical expressions that neglect the interfacial thermal resistance predict an increasing effective thermal conductivity with increasing concentration of conductive particulate inclusions, regardless of the inclusion size, contrary to the observed experimental data. Using a modified Hasselman-Johnson model,

Zain-ul-abdein *et al.* showed that the divergent behavior could be predicted when the composite matrix thermal conductivity was greater that the product of the inclusion radius and the boundary conductance. In resistive systems where increasing concentrations of conductive inclusions decreases the effective thermal conductivity, the interfacial thermal resistance dominates the composite thermal response, and the bulk properties are relatively insensitive to the effect of inclusion shape. Alternatively, in low resistance composite systems where increasing concentrations of conductive inclusions increases the effective thermal conductivity, the contribution of the inclusion shape plays a more dominant role in the effective thermal conductivity [54].

Gao *et al.* and Zhu *et al.* have recently applied analytical models to specifically identify the interfacial boundary resistance and the individual component densities as critical parameters for UO_2-BeO composite thermal conductivity. When the thermal boundary resistance calculated by the DM model resulted in a negligible impact on the effective composite thermal conductivity, Zhu *et al.* used the model developed by Hasselman and Johnson to scope the critical particle size and critical volume fraction to achieve a desired enhancement in thermal conductivity. For a dispersed microstructure, the critical radius of the BeO granules, $a_{critical}$, for improvement in the matrix thermal conductivity with a thermal boundary resistance can be described by

$$a_{critical} = \frac{k_p \cdot R}{k_p / k_m - 1}, \tag{9}$$

where k_p is the particle thermal conductivity, k_m is the matrix thermal conductivity, and R is the thermal boundary resistance. For a continuous microstructure, the critical radius of the UO_2 granules, denoted by $l_{m-critical}$, can be described by

$$l_{m-critical} = \frac{R \cdot l_{mp}\left[-2k_m(1+l_{mp})^2 + k_p(2+4l_{mp})\right]}{(l_{mp}^2 - l_{mp} - 1) + {k_m(l_{mp}+1)^2}/{k_p} - {k_p(2l_{mp}^2 + l_{mp})}/{k_m}}, \quad (10)$$

where, in the continuous microstructure case, k_p is the thermal conductivity of the continuous component, k_m is the thermal conductivity of the majority-phase granules, R is the thermal boundary resistance, and l_{mp} can be calculated by

$$l_{mp} = \frac{l_m}{l_p} = \frac{(1-V_p)^{1/3}}{1-(1-V_p)^{1/3}} \quad (11)$$

with V_p as the volume fraction of the continuous component. The expressions are derived from an analytical equation formulated by the method of equivalent thermal resistance

$$k_{eff} = \frac{1}{l_{mp}+1} k_p + \frac{1}{{k_p}/{k_m} + {1}/{l_{mp}} + {2k_pR}/{l_m}} k_p \quad (12)$$

for a two-dimensional model and

$$k_{eff} = \left(\frac{1}{{l_{mp}+1}/{l_{mp}+2}} + \frac{1}{l_{mp}+1}\right) k_p + \frac{1}{{k_p}/{k_m} + {1}/{l_{mp}} + {2k_pR}/{l_m}} \cdot \frac{1}{{1+1}/{l_{mp}}} k_p \quad (13)$$

for a three-dimensional model [26]. While the theoretical thermal boundary resistance for the composite was on the scale of 10^{-9} m^2-K/W, the values fit to the experimental results for continuous microstructures reported by Ishimoto *et al.* and Garcia *et al.* were on the scale of 10^{-6} to 10^{-5} m^2-K/W [26].

The results reported by Zhu *et al.* were supported by additional experimental work by Gao *et al.* on the spark plasma sintering fabrication process described by Li *et al.* and

further analysis on new composites fabricated by pressureless sintering. To rationalize differences between the experimental results and theoretical predictions, Gao *et al*. found that both the interfacial thermal resistance and the composite's components' densities were integral to the bulk thermal conductivity. After finding the BeO density to be in the range of 70 to 80% of the theoretical density, the fit interfacial thermal resistance was also reported on the scale of $10^{-6} - 10^{-5}$ m^2-K/W, in agreement with Zhu *et al.* Gao *et al.* also presents TEM micrographs showing a bonded, crystalline UO_2-BeO interface clear of contamination or reaction productions. The literature demonstrates both the utility of analytical expressions in quantifying unknown variables, such as the interfacial thermal resistance and component thermal conductivity, [25-26,31-32,41,54] and in constructing explicit terms for critical parameters to the thermal conductivity enhancement [26].

The previous work by Zhu *et al.* and Gao *et al.* have quantified the interfacial thermal resistance by fitting analytical expressions to the experimental results for continuous microstructures. When comparing the analytical fit to the experimental results using Bruggeman's equation, Ishimoto *et al.* found that the error for the dispersed microstructures was $\pm$5%; however, for continuous microstructures assuming a lamellar BeO shape, a maximum error of 20% was reported. By fitting the shape parameter in Bruggeman's equation, the error could be reduced to 10% for the continuous microstructure. While for near spheres the analytical results are insensitive to the shape factor, the predicted composite thermal conductivity changes rapidly with small changes in the shape factor near lamella [40]. The results suggest that a more accurate interfacial thermal resistance could be obtained from a dispersed microstructure composite where the

analytical expressions are less sensitive to shape and the microstructures are more easily described by quantitative stereology.

This section has provided a brief summary of the literature on theoretical, computational, experimental, and analytical methods to quantify the interfacial thermal resistance. The existing literature supports the assertion that the interfacial thermal resistance is a critical feature in the analysis of the thermal conductivity of a UO_2-BeO composite, as suggested by Latta, Revankar, and Solomon [16]. The theoretical and computational approaches utilized to quantify the interfacial thermal resistance did not report meaningful improvements in the analytical model accuracy. The experimental methods applied to continuous microstructures have resulted in significantly higher values for the interfacial thermal resistance, improving model accuracy; however, the conclusions of Ishimoto *et al.* and Zain-ul-abdein *et al.* suggest the measurement is sensitive to the shape descriptors of the microstructure, features not fully analyzed in the reported literature.

With the interfacial thermal resistance, computational simulations of domains inaccessible to experimental methods can perform invaluable research to both validate analytical models and in future work evaluating the composite fuel. While beyond the scope of the work performed here, using mesoscale modeling, several systematic studies have extended the analytical equations for effective thermal conductivity at grain boundaries. The approach simplifies Eq. 8 to a single phase

$$\frac{k_{eff}}{k_0} = \frac{1}{1+\frac{k_0 R_k'}{d}} \quad , \tag{14}$$

where k_{eff} is the effective thermal conductivity, k_0 is the thermal conductivity of the grain interior, R_k' is the effective grain boundary thermal resistance, d is the grain size. Within this formulation, the effective grain boundary thermal resistance can encapsulate not only the grain boundary thermal resistance but other boundary features such as grain boundary-restricted pores. Using this approach, the authors simplified expressions for the effective grain boundary resistance, dependent only on the critical features, grain boundary resistance and the grain boundary pore coverage [96-98]. Complementary work for composite interfaces could bridge the understanding of the individual contributions of the boundary and contact resistance to interfacial thermal resistance.

Computational models of the fuel may also be deployed to validate analytical models for complex conditions, such as the continuous composite microstructures of interest. While determining the shape factors of an interconnected three-dimensional matrix of BeO is challenging to control and measure experimentally, the simulation can be tailored to run purely theoretical scenarios. In this way, the validity of an analytical model can be tested and the influence of microstructural features explored, such as shape and dimension. For example, while analytical expressions predict a dependence, the results reported by Zhou *et al.* and Latta *et al.* showed no impact of the UO_2 granule shape or the simulation dimension on the simulated results; however, the simulations by Zhou *et al.* and Latta *et al.* did not incorporate an interfacial thermal resistance which has since been demonstrated to be critical.

In simulating microstructures of UO_2-BeO composites, Badry *et al.* (including this author) incorporated the interfacial thermal resistance into a phase field model, explored

the influence of simulation dimension, and simulated novel microstructure geometries. While ANSYS has historically been the standard for finite element analysis, the open source code MOOSE specifically undertakes the multiscale, multiphysics challenges facing the nuclear industry [99-102]. Representations of the simulated dispersed and continuous microstructures are shown in Fig. 2.6. For the dispersed configuration, the particle radius was 12.6 nm for the 5 vol.% case and 17.84 nm for the 10 vol.% case. The continuous microstructure was obtained by constructing Voronoi diagrams. The grain size (UO_2) was 100.6 nm for the 10 vol.% case and 174 nm for the 6 vol.% case [27].

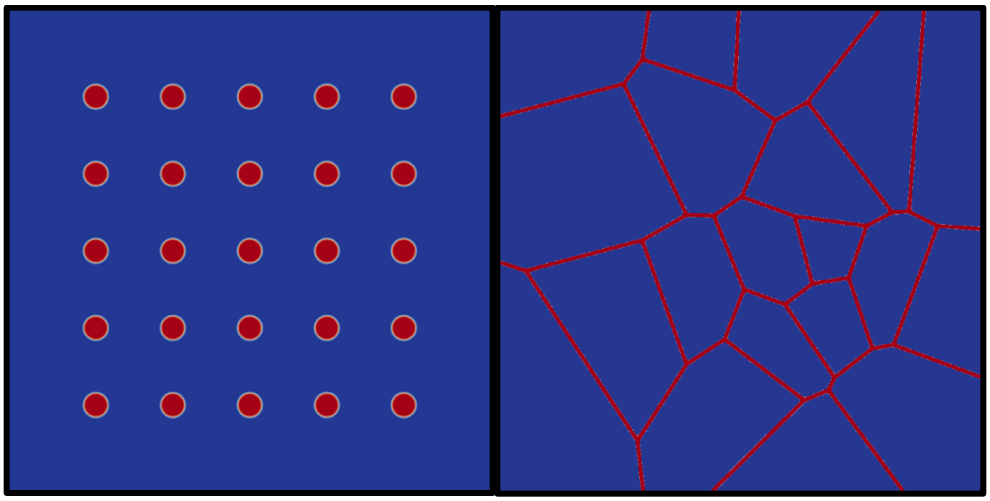

Figure 2.6 Demonstrative two-dimensional phase field model representing the dispersed (left) and continuous (right) UO_2-BeO microstructures simulated by Badry *et al.* with the blue representing the UO_2 and the red representing the BeO, Reprinted with permission from Springer Nature* [27]

* Reprinted with permission from "An Experimentally Validated Mesoscale Model of Thermal Conductivity of a UO_2 and BeO Composite Nuclear Fuel" by F. Badry, R. Brito, M.G. Abdoelatef, S. McDeavitt, and K. Ahmed, 2019. *JOM Journal of the Minerals, Metals and Materials Society*, 71, 4829-4839, Copyright 2019 by Springer Nature.

The work quantified the interfacial thermal resistance between beryllium oxide and uranium dioxide by fitting a value to the experimental data at a single temperature for a dispersed microstructure, fabricated using the methodology described by Garcia *et al*. as a precursor to the samples discussed in Chapter 4. The fit value, on the order of 10^{-10} m^2-K/W, improved the accuracy to within the experimental error across all modeled two-dimensional microstructures and temperatures [27]. The fit value is far lower than other experimental methods (10^{-6} to 10^{-5} m^2-K/W) and between the theoretical predictions reported by Zhu *et al.* (10^{-9} m^2-K/W) and Liu and Zhou (10^{-11} m^2-K/W) [24-26]. The uniform spacing and size of the BeO granules in the simulated microstructure, as compared to the random spacing and widely distributed size in the experimental microstructure shown at high and low magnification in Fig. 2.7, is expected to contribute to the error in the reported interfacial thermal resistance value.

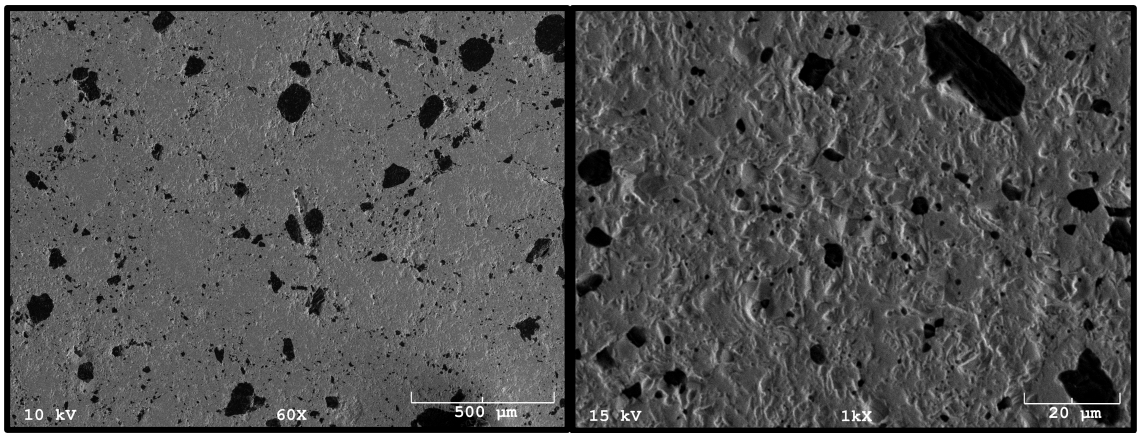

Figure 2.7 SEM micrograph of UO_2 (gray) with 15 vol.% BeO (black) dispersed at 60x (left) and 1000x (right) magnification demonstrating the random distribution of particles with a wide distribution of sizes shown at the two magnifications.

Badry *et al.* also performed two- and three-dimensional simulations of the dispersed microstructure computing an increasing error with increasing concentration of BeO, eclipsing the experimental error at around 10 vol.%. The three-dimensional simulations, comparable to the experimental microstructure, had a universally higher thermal conductivity than the two-dimensional simulations. When the two-dimensional simulations were corrected to account for the difference, the agreement between the simulated and experimental results improved, especially at higher BeO concentrations. Curiously, the two-dimensional results for the continuous microstructure were consistent with the experimental data uniformly across the BeO concentrations studied. Three-dimensional simulations of the continuous microstructure were not reported [27].

The relative importance of the simulation dimension is debated in the literature. As previously discussed, Latta, Revankar, and Solomon, Zhou *et al.*, and Boey *et al.* have reported results supporting they are independent for the continuous microstructures simulated; although, an interfacial thermal resistance was not implemented [16,49-50]. Recalling, Latta, Revankar, and Solomon and Zhou *et al.* also simulated that the thermal conductivity was independent of the shape of the UO_2 granules, while Ishimoto *et al.* found the thermal conductivity of the continuous microstructure was highly dependent on the shape of the BeO phase [16,40,49]. Bakker, Teague *et al.*, Millett and Tonks, Millett *et al.*, and Badry *et al.*, however, have shown the contrary [27,97-98,103-104]. Badry *et al.* found that for UO_2-BeO composites the inclusion concentration controlled the magnitude of the influence of simulation dimension, a finding supported generally by the analytical expressions compared by Bakker [27,103]; however, Teague *et al.* found that

the magnitude could not be predicted as explicitly as suggested by Bakker [104]. Millett and Tonks and Millett *et al*. demonstrated that three-dimensional simulations captured the of influence of pore size, not otherwise captured in two-dimensional simulations, in addition to the effect of concentration [97-98]. Similarly, the influence of inclusion size on the effective thermal conductivity is only apparent when the interfacial thermal resistance is accounted for [28-33,54].

The literature appears to conclude a definitive, while difficult to universally define, dependence of the thermal conductivity on simulation dimension for dispersed microstructures; however, the evidence for continuous microstructures is less compelling, though suggestive of no dependence. With the indication that the interfacial thermal resistance is critical to the understanding of heat transfer in UO_2-BeO composites, the lack of implementation in the simulations by Latta, Revankar, and Solomon and Zhou *et al.* may interfere with the understanding of the roles of dimension and shape in simulating the thermal conductivity. The analytical expressions proposed by Zhu *et al.* for two- and three-dimension continuous microstructures in Eq. 12 and 13 will be of interest to validate against the variety of geometries and dimensions of simulated microstructures, both with and without an implemented interfacial thermal resistance [26]. Regardless, it is clear that the interfacial thermal resistance is a necessary initial step to understanding the role of simulation dimension and granule shape and size in the composite thermal conductivity which will aid in the informed design of the microstructure for optimized thermal properties.

This review has considered the historical development of the fabrication of UO_2-BeO composites for application as an LWR nuclear fuel. Prior investigations of the composite achieved microstructures with improved the bulk thermal conductivity. Even modest improvements in the thermal conductivity, on the scale of the spread of the reported literature, resulted in fuel performance consistent with an accident tolerant fuel. Identifying the critical features responsible for spread of results is key to the informed design of the composite microstructure and ultimate optimization of the thermal conductivity.

Previous studies simulating the experimentally achieved UO_2-BeO microstructures were inconsistent in accuracy and highlighted the role of the interface in heat transfer. Theoretical, computational, experimental, and analytical methods to quantify the interfacial thermal resistance have been presented along with applications of the interfacial thermal resistance in modeling of composite microstructures. By incorporating the effects of the interfacial thermal resistance, physically justified and adaptable models to describe the composite thermal conductivity have been developed. For the UO_2-BeO composite system, the implementation of the interfacial thermal resistance improved the agreement between the simulations and the experimental results; however, this present work presents a methodology targeted to improve error by fabricating and characterizing a comparably simple and robust composite microstructure tailored to enable the measurement of the interfacial thermal resistance rather than as an accident tolerant fuel.

Previous work studying UO_2-BeO composites reinforces the need for a thorough understanding of the composite physical properties and emphasizes the role the interfacial thermal resistance plays in unifying the relationship between microstructure and bulk properties. This work quantifies the interfacial thermal resistance between UO_2 and BeO by developing a well-characterized database of dedicated samples contributing to the core of the informed design of the microstructure for improved thermal conductivity. In the chapter that follows, this dissertation presents a methodology developed to fabricate and characterize microstructures for quantifying the interfacial thermal resistance by a combined experimental and analytical method and an analytical model for the thermal conductivity of the composite microstructure, implementing the interfacial thermal resistance. As a result, practical limits may be set to inform the design of the composite microstructure for improved thermal conductivity in application as an accident tolerant fuel.

3. METHODOLOGY

The methodology to quantify the interfacial thermal resistance by the flash method and then implement it in a validated analytical model is given in the following sections. In Section 3.1, the experimental fabrication process is described to produce dense, uniform, spherical granules of BeO dispersed in a UO_2 matrix. The procedure follows the stages described by Garcia *et al.*, where continuous UO_2-BeO microstructures were produced, using identical source powders [34]. In Section 3.2, the experimental methods to characterize the resultant composite samples are detailed to include density by the immersion method and pycnometer and thermal diffusivity by light flash analysis. Then, the methodology to convert the thermal diffusivity to thermal conductivity at a uniform porosity is also covered. Finally, in Section 3.2, the combined experimental and analytical flash method is justified to calculate the interfacial thermal resistance. In Section 3.3, the methodology to characterize the microstructure by microprobe and convert the observed, two-dimensional sections to the three-dimensional microstructural features is discussed.

Theoretical, computational, experimental, and analytical methods to quantify the interfacial thermal resistance were presented in Chapter 2. To maintain processing alignment with industry practice, the UO_2-BeO composite under study here was fabricated by sintering; however, interface defects are not unusual in sintered compacts and the thermal contact resistance contribution to the interfacial thermal resistance is expected to be nonnegligible. While all the methodological categories have the capacity to quantify the thermal boundary resistance, many have limited functionality to capture the thermal

contact resistance. The acoustic mismatch (AM), diffuse mismatch (DM), and lattice dynamics (LD) models generally assume a perfect interface, and the thermal contact resistance is ignored. Overall, theoretical approaches and LD and MD models to compute the interfacial thermal resistance are unable to account for true physical realities such as surface oxidation, roughness, and debonding in the proposed application of the UO_2-BeO composite studied here.

As indicated in Chapter 2, experimental methods can target the direct measurement of the thermal boundary resistance or the interfacial thermal resistance [58]. The thermal conductivity results reported by Ishimoto *et al.*, Sarma *et al.*, Garcia *et al.*, Gao *et al.*, and Li *et al.* display a wide variety of improvement that could not be reconciled by simulations of the composite without the incorporation of a hypothesized interfacial thermal resistance [3,16,34,40]. With the incorporation of this interfacial thermal resistance, analytical results for dispersed microstructures reveal the granule size as a critical feature in the microstructures impacting the effective thermal conductivity [28-33]. The processing of UO_2-BeO composites may impact the magnitude of the thermal contact resistance or critical features with poorly understood influence; thus, experimental methods offer a unique approach to directly measure the interfacial thermal resistance not available by other methods. Of the experimental methods reviewed in Chapter 2, the flash method is well suited to the requirements of the application and was selected for this study. Suitably, the scale of the experimental measurement is appropriate for the analytical model of interest.

A benefit of the flash method is that it can be applied directly to as fabricated microstructures of interest; however, an analytical expression must relate the effective thermal conductivity to the component thermal conductivities, the interfacial boundary resistance, the composition, and particulate shape descriptors. While expressions exist for percolated microstructures in the investigations given in the literature review, the results vary dependent on the developmental approach [26,28-33]. Ishimoto *et al.* associated a 20% error between experimental results and the analytical expression used when the shape descriptors of the continuous BeO phase were not optimized [40]. Direct measurement of the shape descriptors for this microstructure is not trivial.

Dilute, dispersed microstructures, more easily described analytically, however, can be manufactured using the same processing procedures as the continuous UO_2-BeO microstructures. The dilute, dispersed microstructures are not of interest as a nuclear fuel concept, rather are fabricated specifically to measure the interfacial thermal resistance. This work simplifies the microstructure while maintaining the processing procedures utilized to fabricate the continuous microstructures. The interfacial thermal resistance can then be precisely quantified while maintaining the direct link to UO_2-BeO composites for accident tolerant fuel applications. Ishimoto *et al.* reported a 5% error between experimental results and the analytical expression for dispersed microstructures, so this work significantly improves measurement accuracy [40].

Following the methodology used by Nan, Li, and Birringer, Eq. 8 can solve for the interfacial thermal resistance and the component thermal conductivity with flash results from a minimum of three experimental microstructures [32]. This approach determines

not only the interfacial thermal resistance, but also the thermal conductivity of the UO_2 and BeO in application, both factors identified by Latta, Revankar, and Solomon and Gao *et al.* as contributing to the error in previous work [16,25]. To use this method, the experimental work must determine the effective thermal conductivity and the particulate inclusion concentration and diameter, as suggested by Eq. 8.

3.1. Experimental Materials, Methods, and Analysis

Garcia *et al.* systematically evaluated the powder processing and sintering of co-continuous UO_2-BeO compacts using methods aligned with industry practice [34]. The procedure recommended by Garcia *et al.*, grounded in the framework developed by Sarma *et al.*, is as follows: pre-compact milled UO_2 powder at 680 MPa, break apart the pre-compacted powder using a mortar and pestle, sieve the resultant granules to between 53 and 500 μm, self-mill, introduce the BeO powder, compact to between 200 and 225 MPa, and sinter at 1873 K for 4 to 6 hours under an Ar-5% H_2 atmosphere [3,34]. This work follows this framework, as applicable, to form dense microstructures with spherical, dispersed particulate inclusions of BeO by sintering. A summary of the fabrication process is shown in Fig. 3.1. By striving to use the same procedure as recommended for the co-continuous microstructures, this work maintains a connection to the interfacial thermal resistance in the co-continuous microstructures despite fabricating a dilute, dispersed microstructure. In this way, the fabrication of the UO_2-BeO dispersed composite remains suitable for industry implementation, LFA measurement of the thermal diffusivity, quantitative stereology of the microstructure, and the application of the effective medium approximation employed by Nan, Li, and Birringer [31-32].

Figure 3.1 Pellet fabrication flow chart for dispersed UO_2-BeO composite compacts with two parallel granulation steps for UO_2 (blue) and BeO (red) prior to final compaction (purple) and sintering (gray)

The as-received depleted UO_2 powder was supplied by International Bio-Analytical Industries Inc (Boca Raton, FL) and the as-received BeO powder was obtained from Acro Organics (Geel, Belgium). Both powders are from the same batch as reported by Garcia *et al.* in the continuous microstructures. The as-received powders required additional processing prior to compaction and sintering. The milling of the powders followed the processes described by Garcia *et al.* [34]. The jet milling procedure for the BeO powder was performed using a Model 00 Jet-O-Mizer by Fluid Energy with a

tungsten carbide liner with pressurized ultra-high purity argon gas at 0.55 MPa as the feed and 0.69 MPa as the grinding propellant. The UO_2 powder was ball milled with yttria-stabilized zirconia milling balls in an alumina jar (Model 774 Roalox Alumina-fortified grinding jar) on a rotary jar mill (U.S. Stoneware CV-80461). The ball-milled UO_2 powder was reduced in an Ar-5% H_2 atmosphere at 873 K for 3 hours in a Materials Research Furnace M-5X12 (MRF) prior to granulation to remove excess oxidation accumulated in storage.

It was desirable to form spherical granules of both components of the composite with a narrow size distribution to ensure a uniform microstructure. To form spherical granules, an aqueous PEG-8000 binder was introduced to the powders in a mortar and pestle to account for approximately 4 vol.% prior to sintering using a density of 1.125 g/cm^3 for the PEG-8000, 3.010 g/cm^3 for the BeO, and 10.963 g/cm^3 for the UO_2. Deionized water was added to the PEG-8000 powder to just achieve solubility at approximately 30/70 mass ratio of PEG-8000 to water. The powder mixture was compacted in a 13 mm split-sleeve, single-action die to 90 kN. Next, the powder compact was crushed in a mortar and pestle and self-milled on the rotary mill for approximately 2 hours to form the spherical granules. The granules were hand sieved to collect diameters between 425 μm and 300 μm and between 250 μm and 150 μm.

Using the granules within the stated diameter bins, samples with three particulate concentrations and two average particulate diameters were manufactured. The concentrations of 5, 10, and 15 vol.% were fabricated, well below the 40 vol.% upper limit set by Nan, Li, and Birringer [32], but distinct with respect to the accuracy of the

experimental measurement. The individual component mass was selected to result in a dense cylindrical pellet roughly 4 mm thick and 13 mm in diameter of the given concentration of BeO granules. To lubricate the granules during final compaction, 1 vol.% of zinc stearate was added to the UO_2 granules using a density of 1.1 g/cm^3 for the zinc stearate and tumbled to mix. Then, the BeO granules were carefully introduced and mixed to disperse but reduce loss of powder from the granules.

To form the final compact, the powders were introduced to a 15 mm single-action die lubricated by LPS-2 Heavy-Duty Lubricant and compacted to 25 kN using a Carver Press. The pressed compact was sintered in the MRF furnace on an alumina plate covered by a crucible under an Ar-5% H_2 atmosphere at 1963 K for up to 14 hours. The temperature profile is shown in Fig. 3.2. The hold temperatures at 433 K, 573 K, and 973 K were selected to burnout the water solvent, adsorbed water, and binder in controlled stages to maintain compact integrity. The final sintering temperature was programmed as 1963 K; however, thermocouple readings were nearer to 1923 K. The soak time varied to accommodate scheduling, but Garcia *et al.* showed 6 hours was sufficient to densify the composite [34].

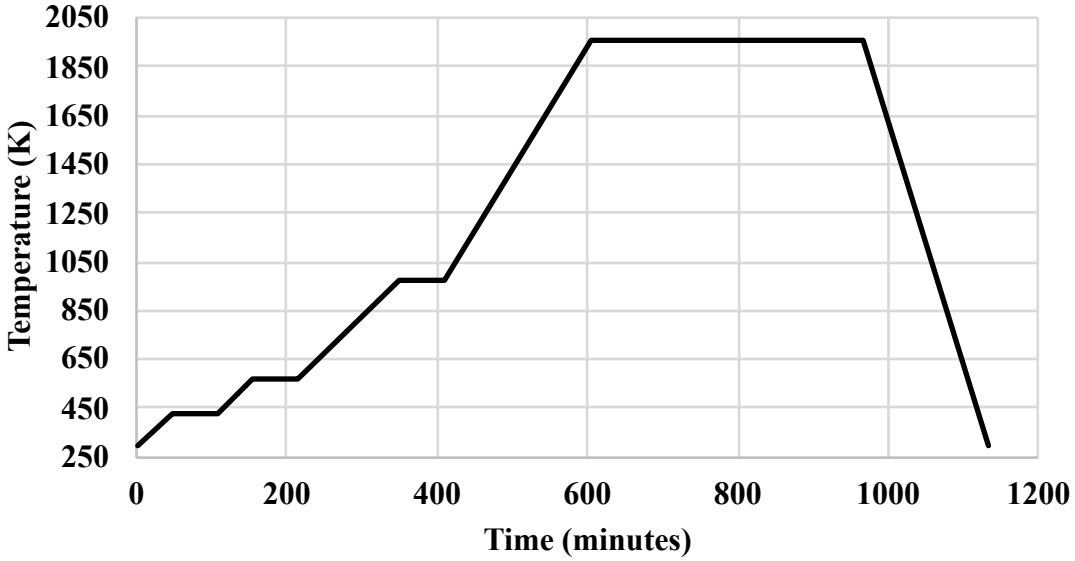

Figure 3.2 The sintering temperature profile for dispersed UO_2-BeO composite compacts featuring three burnout steps prior to a final soak temperature of 1963 K

Following sintering, the samples were sectioned into 3 cylindrical discs for further analysis using a Buehler Isomet Low Speed Saw equipped with a diamond blade lubricated by DIACUT Cutting Fluid from PACE Technologies. Approximately 1 mm was sectioned off of either side, with one side archived and the interior side of the other was used for microstructural analysis. The remaining 2 mm was used for physical property analysis, to include density and thermal diffusivity measurements.

3.2. Thermal Diffusivity and Physical Property Measurement

To apply the inverse method described by Nan, Li, and Birringer, the effective thermal conductivity of the composite is calculated from the measured thermal diffusivity by Eq. 5 when the specific heat and density are known. The specific heat is determined by volumetric weighting of the component properties, an approach shown to be accurate for UO_2-BeO composites by Garcia *et al*. using differential scanning calorimetry (DSC) [34].

The temperature-dependent specific heat equation suggested by Fink is used to describe the properties of the UO_2 component. The general equation in units of J/mol-K is

$$C_p(T) = \frac{C_1\theta^2 e^{\theta/T}}{T^2\left(e^{\theta/T}-1\right)^2} + 2C_2T + \frac{C_3E_a e^{-E_a/T}}{T^2}, \quad (15)$$

where C_1 is 81.613, θ is 548.68, C_2 is 2.285×10^{-3}, C_3 is 2.360×10^{7}, E_a is 18531.7, and T is the temperature in K [19]. For the temperature-dependent specific heat equation for BeO, the same general function given in Eq. 15 was fit to the data available in the CINDAS database [20]. The resulting variables for the best fit to the BeO data are C_1 is 42.403, θ is 810.96, C_2 is the 4.056×10^{-3}, C_3 is 2.748×10^{-2}, and E_a is 46000.

To determine the density and thermal diffusivity of the UO_2-BeO composites, cylindrical samples of dimensions less than 15 mm in diameter and roughly 2 mm in thickness were fabricated to be compatible with both the NETZSCH LFA 447 NanoFlash and the Quantachrome UltraPYC 1200e sample holder dimensions. Heterogenous materials with particulate inclusion sizes up to 25% of the sample thickness have been shown in other investigations to reflect the bulk thermal diffusivity as measured by light flash analysis (LFA) [86-87]. The ratio of the particulate inclusion diameter (upper limits of 425 and 250 μm) and LFA sample thickness (2 mm) in this work will be below 25% and thus appropriately reflect the results of bulk samples.

Sintered samples were prepared for LFA and pycnometer by a rough polishing within 0.0005 in of parallel, as measured by a micrometer. The density of each disc was measured using three independent methods to evaluate the porosity in the sample. The first density value was simply from the sample dimensions, geometry, and mass. Following polishing, the sample's thickness (t) and diameter (d) were measured 5 times

with a Mitutoyo Digimatic Caliper and the average values used to estimate the volume of the cylinder. The mass (m_d) was measured using a METTLER TOLEDO XSR105 balance. The geometric bulk density (ρ_G) was then determined by the equation

$$\rho_G = \frac{m_d}{\pi t\left(\frac{d}{2}\right)^2}. \quad (16)$$

The density and porosity associated with the geometric bulk density are the true density and both the open and closed porosity in the compact, as well as the volume of defects resulting in a geometry differing from a perfect cylinder, such as chipping, dishing, and hourglassing.

The second density method to determine the sample density used the Quantachrome UltraPYC 1200e pycnometer to measure the solid volume with nitrogen as the working gas. The sample density is calculated as the quotient of the mass and the measured volume. To accommodate the sample diameter, the large cell with an accuracy of ±0.1% was used and calibrated with the small calibration sphere provided, which had the closest volume to the sample being analyzed. The final reported values are the average of 8 consecutive runs with a deviation of less than 0.17% which was shown to provide consistent results following system equilibration. The density and porosity associated with the pycnometer measurement are highly precise and accurate but measure only the true density and the closed porosity in the compact.

The third method to determine the sample density was an immersion method using an OHAUS Density Determination Kit with ethanol as the working fluid. By measuring the dry mass (m_d), the immersed mass (m_i) using the kit, the wetted mass (m_w) using an airtight container, and the density of the working fluid (ρ_{fl}), the bulk or envelope density

(ρ_B), the solid density (ρ_S), and the open porosity (P_o) can be calculated using the equations

$$\rho_B = \frac{m_d \cdot \rho_{fl}}{m_w - m_i}, \tag{17}$$

$$\rho_S = \frac{m_d \cdot \rho_{fl}}{m_d - m_i}, \tag{18}$$

$$P_o = \frac{m_w - m_d}{m_w - m_i}. \tag{19}$$

As shown in Eq. 17, 18, and 19, the immersion method is flexible in the density and porosity that can be calculated from the dry, immersed, and wetted mass; however, the viscosity of the working liquid and user error contribute to error in the immersed and wetted mass measurement. The final reported values in Chapter 4 are the average of 3 measurements to reduce the error and the final solid density can be compared to the values measured by the pycnometer, a more precise and accurate method for the solid density.

While the changes in density with temperature are small over the range studied here, the expression for UO_2 reported by Fink was implemented in the calculation of the density ($\rho(T)$) over the range studied as

$$\rho(T) = \rho(273)\left(\frac{1}{9.973\times10^{-1} + 9.082\times10^{-6}T - 2.705\times10^{-10}T^2 + 4.391\times10^{-13}T^3}\right)^3, \tag{20}$$

where T is the temperature in K and $\rho(273)$ is the density at the reference temperature of 10.963 $\mathrm{g/cm^3}$ [19]. The specific heat and density of UO_2 plotted from Eq. 15 and Eq. 20 are shown in Fig. 3.3. An expression for the linear thermal expression of BeO ($\frac{\Delta L}{L}$) from a CINDAS literature review was implemented to account for changes in density with temperature with the equation

$$\frac{\Delta L}{L} = -0.157 + 4.433 \times 10^{-4}T + 3.276 \times 10^{-7}T^2 - 2.754 \times 10^{-11}T^3, \quad (21)$$

where T is the temperature in K and the ΔL is measured from the reference temperature of 293 K [20]. The reference density ($\rho(293)$) used was 3.010 g/cm^3 as reported by Bellamy, Baker, and Livey [105] and the calculation was performed by

$$\rho(T) = \frac{\rho(273)}{1+\left(\frac{\Delta L}{L}\right)^3}. \quad (22)$$

The specific heat and density of BeO plotted from Eq. 15, Eq. 21, and Eq. 22 are shown in Fig. 3.4.

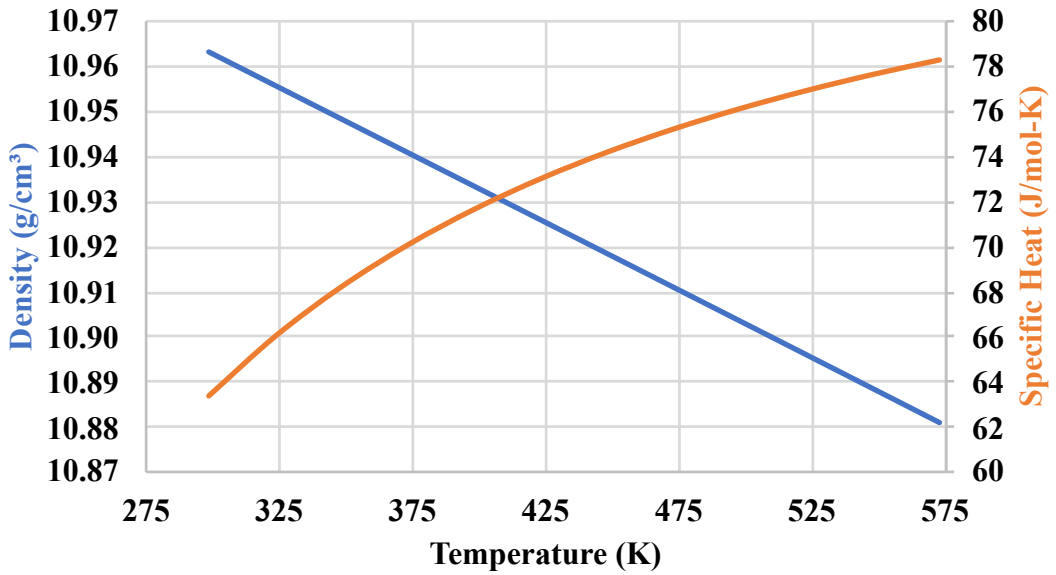

Figure 3.3 The specific heat and density of UO_2 used to compute the thermal conductivity over the temperature range of interest in the present work [Based on 19]

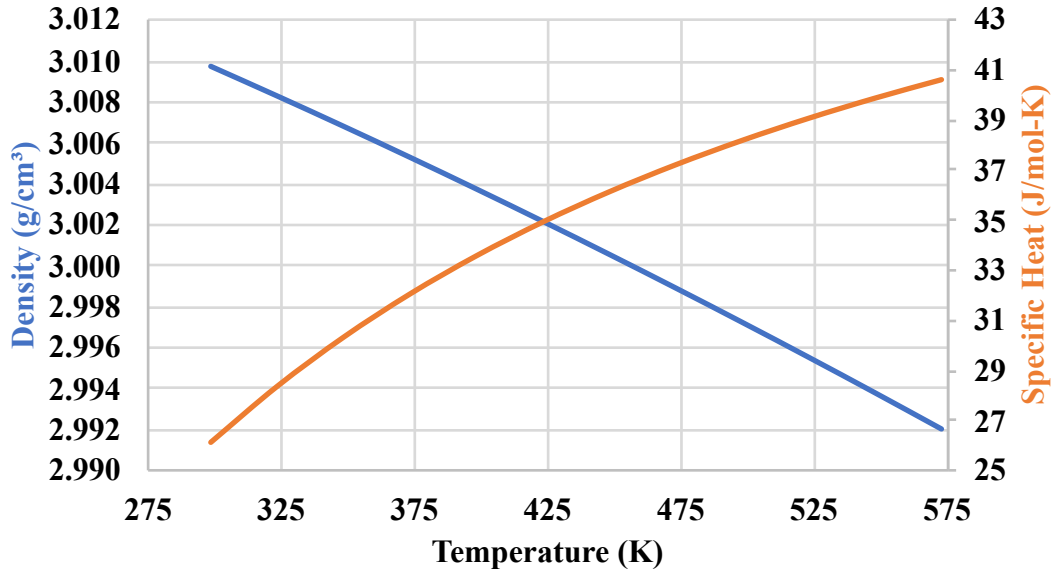

Figure 3.4 The specific heat and density of BeO used to compute the thermal conductivity over the temperature range of interest in the present work [Based on 20]

The composite reference density, also referred to here as the theoretical density, was calculated as the volumetric weighted average of the component properties described by Eq. 20 and Eq. 22. For a given sample, the fraction of the theoretical density was calculated as the quotient of the solid density measured by pycnometer and the composite reference density. The pycnometer density is the most precise method and the value is expected to accurately reflect the sample volume interrogated by the LFA analysis. The thermal conductivity was then calculated with the density represented as the product of the fraction of the theoretical density and the composite reference density at the temperature of interest.

To estimate the thermal conductivity using Eq. 6, the methodology to determine the specific heat and density have been described. The thermal diffusivity was then measured by LFA. Following sectioning, polishing, and the measurement of the sample

density, the sample was coated with a thin layer of graphite (Sprayon Dry Film Graphite Lubricant, LU 204) to improve signal absorption and emission. The thermal diffusivity was measured from 298 K to 573 K, the limits of the instrument, at 25 K increments, and calculated by the Cowan model within the software provided by Netzsch [80-81]. The average of three measurements is reported and used to calculate the thermal conductivity using Eq. 6.

For comparative purposes and the evaluation of the analytical expressions for composite thermal conductivity, expressions for the thermal conductivity of the composite components are also of interest. The expression for the thermal conductivity in W/m-K of 95%TD UO_2 (k_{95}) recommended by Fink given by the form

$$k_{95} = \frac{100}{A+Bt+Ct^2} + \frac{100D}{t^{5/2}} e^{-E/t} , \quad (23)$$

where A is 7.5408, B is 17.692, C is 3.16142, D is 64, E is 16.35, and t is the temperature in K divided by 1000 [19]. The thermal conductivity in W/m-K of 98%TD BeO is fit to the recommended data in CINDAS using the same functional form but A is 0.07363, B is 0.5221, C is 1.4877, D is 66.1654, and E is 13.3107 [20]. The results of the expressions are shown in Fig. 1.1, for reference.

For comparative purposes, the calculated thermal conductivities (k_P) are corrected to represent a uniform closed porosity. The Brandt and Neuer correction given by

$$k_{100} = \frac{1}{1-(2.6-0.0005 \cdot T)P} k_P , \quad (24)$$

where P is the measured porosity and T is the temperature in K, is commonly used for UO_2 and the UO_2-BeO composite in the literature, although a review of the applicability

to the composite has not been completed [106]. Compared to the Maxwell-Garnett correction

$$k_{100} = \frac{1+\frac{1}{2}P}{1-P} k_P, \tag{25}$$

which can be deduced from Eq. 7 and Eq. 8 when the particle thermal conductivity is set to zero [88-90], the Brandt and Neuer correction predicts a larger reduction in thermal conductivity for a given porosity, as shown in Fig. 3.5. Figure 3.5 shows, for the region of interest to the samples produced, correcting to no porosity leads to an approximately 5% difference between the two porosity corrections at 450 K.

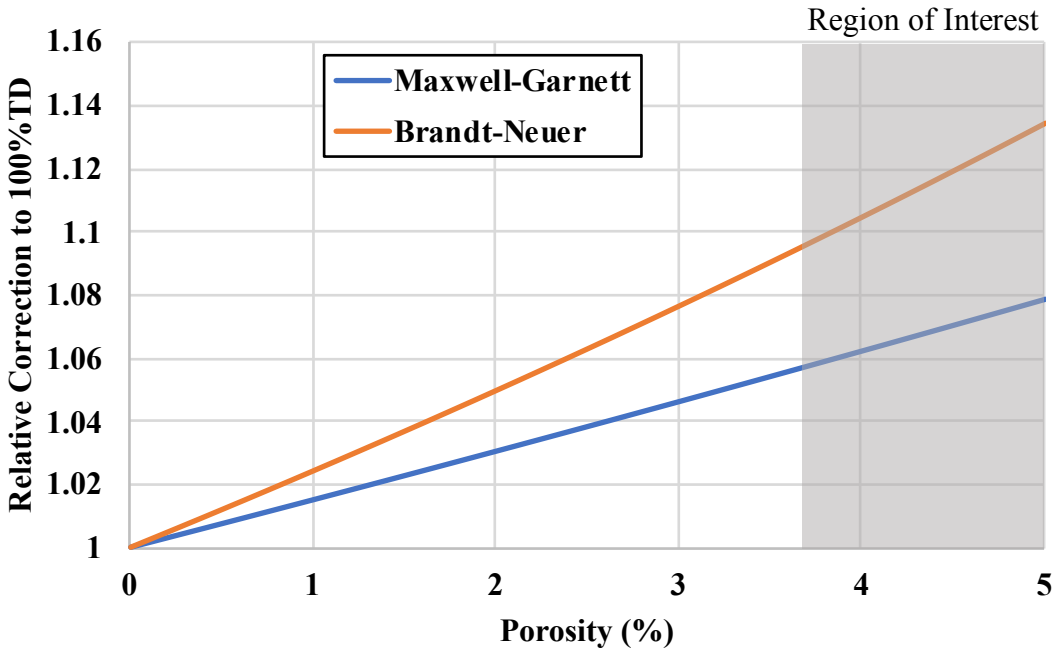

Figure 3.5 Comparison between the Maxwell-Garnett general porosity correction for thermal conductivity and the Brandt-Neuer correction at 450 K developed for UO_2 when correction to 100%TD with the region of interest to this work indicated in gray

Alternatively, the calculated thermal conductivities can be corrected to 95%TD, a commonly reported porosity, near the experimental porosity values. As shown in Fig. 3.6, the resulting difference between the Maxwell-Garnett and Brandt and Neuer corrections for the region of interest is less than 2%, at most. Thus, to follow with convention and minimize any potential error associated with using an unverified expression, this work corrects the experimental thermal conductivity values to a uniform 95%TD using the Brandt and Neuer correction.

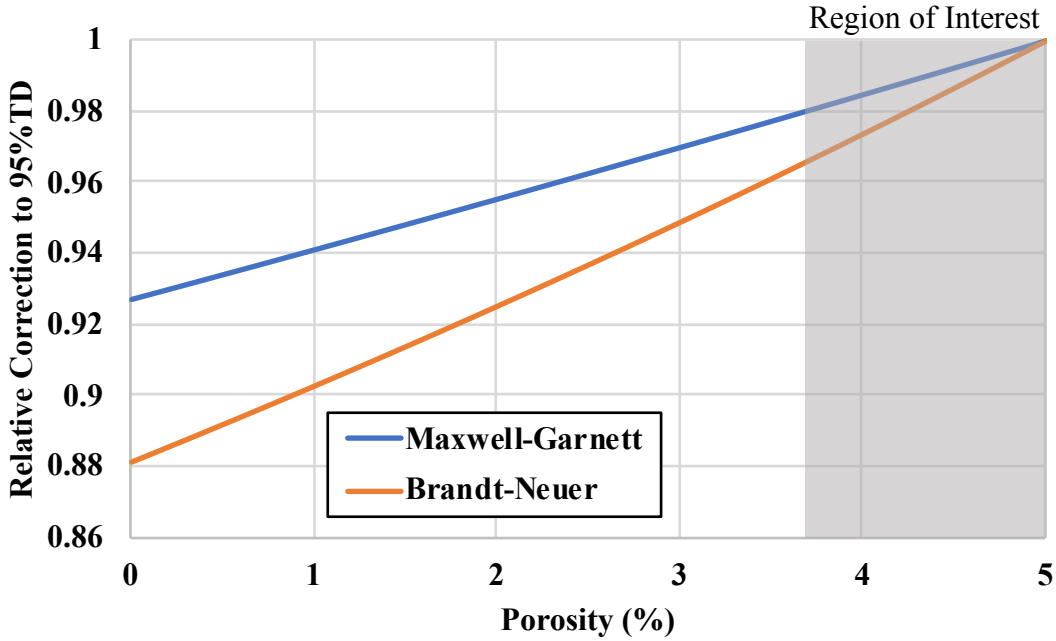

Figure 3.6 Comparison between the Maxwell-Garnett general porosity correction for thermal conductivity and the Brandt-Neuer correction at 450 K developed for UO_2 when correcting to 95%TD from a porosity nearby with the region of interest to this work indicated in gray

To establish the influence of the open porosity on the reported thermal conductivity, a simplified expression, originally reported by Niesel, and later compared to UO_2 by Ondracek and Schulz, given by

$$(1-P)(k_0-k)\left[\frac{1-(\cos\alpha_0)^2}{k(1-F_0)+k_0F_0}+\frac{(\cos\alpha_p)^2}{k_0(1-2F_0)+2kF_0}\right]-P\left[\frac{1-(\cos\alpha_p)^2}{1-F_p}+\frac{(\cos\alpha_p)^2}{2F_p}\right]=0, \quad (26)$$

is used incorporating the open porosity (P) as measured by the immersion method. Equation 26, simplified from the implicit expressions reported by Niesel by assuming nonconducting pores, corrects the thermal conductivity of a dense sample (k_0) to one with interconnected porosity (k) accounting for the matrix (subscript 0) and pore (subscript p) shape (F) and orientation ($(\cos\alpha)^2$)[94,107]. This work considers two cases where the interconnected porosity can be described as spherical and randomly oriented and both the shape and orientation factors are 1/3 resulting in the expression

$$\frac{k}{k_0}=1-\frac{3}{2}P \quad (27)$$

and the case where the interconnected porosity can be described as thin discs oriented perpendicular to the field with both the shape and orientations factors approach 0 resulting in the expression

$$\frac{k}{k_0}=\frac{4-7P}{4+2P}. \quad (28)$$

For both cases, the shape and orientation factors for the matrix have been assumed to be spherical and randomly oriented.

With the physical property analysis detailed and the microstructure analysis in the following section, the inverse method described by Nan, Li, and Birringer can be applied

to calculate the thermal conductivity of the individual components in the composite and the interfacial thermal resistance. From Eq. 8., repeated here,

$$\frac{k_{eff}}{k_m} = \frac{k_p\left(1+\frac{2k_m R_k}{r}\right)+2k_m+2f\left[k_p\left(1-\frac{k_m R_k}{r}\right)-k_m\right]}{k_p\left(1+\frac{2k_m R_k}{r}\right)+2k_m-f\left[k_p\left(1-\frac{k_m R_k}{r}\right)-k_m\right]} \tag{29}$$

a system of equations can be constructed from the fabrication details, f, the volume fraction of particles, and r, the radius of the particles, and experimental results, k_{eff}, the effective thermal conductivity of the composite. Any three of the independent equations associated with the experimental samples can be used to determine the variables treated as unknown, k_p, the thermal conductivity of the particles, k_m, the thermal conductivity of the matrix, and R_k, the interfacial thermal resistance. Alternatively, the literature correlations can be used for the thermal conductivity of the particles and matrix and the interfacial thermal resistance can be determined from the full set of independent equations; although, the thermal conductivity of the particle will differ from the literature reported values for the bulk below a critical diameter [31-32]. A comparison of the results of the different approaches will be considered in future work.

Nan, Li, and Birringer approximated the uncertainty in the interfacial thermal resistance fit by the sum of uncertainty induced by each experimental measurement's uncertainty [31-32]. By varying the composite thermal conductivity, granule radius, and granule concentration by the uncertainty of each respective measurement, the influence on the interfacial thermal resistance and matrix and particle thermal conductivity can be recorded. The sum of the uncertainties is reported as the uncertainty for the fit measurement. The uncertainty for the composite thermal conductivity was calculated as

±5% using the propagation of error for Eq. 6 with the uncertainty of ±3% for the thermal diffusivity as reported by Netzsch for the instrument and ±1% for density and ±4% for the specific heat, as reported by Fink [19]. The uncertainty for the granule concentration was taken to be ±3%, the maximum deviation from the target concentration. The uncertainty for the granule radius of ±4% was calculated by half the range of the individual sample data sets described in detail in Chapter 5.

This section has detailed the experimental and analytical methodology to fabricate and analyze the microstructure and physical properties of dispersed UO_2-BeO composites to calculate the interfacial thermal resistance and the component thermal conductivity in application, two factors identified in the literature as critical [16,25]. The limited particle diameter range and fabrication of multiple concentrations seeks to ensure a reliable experimental measurement of the interfacial thermal resistance as compared to previous work on less ideal microstructures [31-32,40]. The experimental design has been such to preserve the applicability of the measurement to the continuous microstructures desired as an accident tolerant fuel.

3.3. Microstructure Characterization Procedure

From each sectioned sample, a circular, edge section was mounted in a ring mold with Buehler EpoKwick epoxy with the interior surface exposed for analysis. Following curing, the cross-section was polished up to 0.25 μm with Buehler MetaDi monocrystalline diamond suspension. Polished samples were coated by a LADD carbon evaporator at the Texas A & M University Materials Characterization Core Facility (RRID:SCR_022202). The samples were imaged by a Cameca SXFive Electron

Microprobe also at the Texas A & M University Materials Characterization Facility. Micrographs were collected using a 15 kV accelerating voltage, a 20 nA current, and the backscatter electron detector mode, to eliminate the influence of surface defects on the quantification of the particle inclusion diameters.

Quantitative image analysis was performed by ImageJ 1.51 developed by the U.S. National Institute of Health [108]. Selective color change processing was applied to large scale image features—defects like pullout, cracks, and scratches, and epoxy at the sample edge—which had a similar size and gray level to the BeO granules. BeO granules that partially intersected the image frame were also excluded. Using the software to isolate a single color channel and set the image scale, the threshold was set from 0 (black) and up to preferentially distinguish discrete areas of BeO within the UO_2 matrix without introducing noise on the same scale as the smallest BeO particle. For a given image, small variations in the upper threshold limit changed the selected area by less than 0.1%. The area of the discrete granules was then individually evaluated by the software with areas below an individually selected cutoff filtered to eliminate noise. The diameter of the granule can then be calculated by assuming a circular cross-section.

While the electron microprobe produced high resolution and contrast micrographs for quantitative image analysis, the main disadvantage of this method to determine the particle size is that the diameter from a two-dimensional section is sampled from a cross-section of the three-dimensional granule and is statistically skewed smaller than the actual distribution of diameters. The topic has been of interest across disciplines and extensively studied statistically and experimentally [35-39,109-115] and reviewed by Cuzzi and Olson

[35]. The process of unfolding or inverting the binned data from the two-dimensional to the three-dimensional diameter followed here is as described by Cuzzi and Olson, with improvements by Benito *et al.* [115] using the provided MATLAB functions with minor adaptations to notation to accommodate this work.

The process can be understood by the "forward problem," as phrased by Cuzzi and Olson, where a known true diameter distribution (N_V) can be transformed into a distribution of apparent diameters (N_A) measured from a section of the original distribution. When the distribution is binned with bin boundaries (D and d, respectively) the process can be summarized as

$$N_A(d_i) = \sum_{j=i}^{N} F_{ij} N_V(D_j) \tag{30}$$

where the bin boundaries are the same and the matrix F_{ij} accounts for the experimental realities of the measurement of the diameter by sectioning, discussed in the following paragraph. The opposite of the "forward problem" recovers the true diameter distribution from the distribution of apparent diameters, referred to as "unfolding" by some accounts [111-114], can be understood from the inverse of matrix F_{ij}, thus the inversion technique [35].

Assuming the granules can be approximated as spheres, an assumption the microstructure here was designed to support, four experimental realities are considered in the recovery of the true sphere diameter from the apparent circle diameter. First, the observed apparent circle diameter is likely non-diametric, increasing the apparent population of smaller circle diameters. For a monodisperse powder, it has been shown the apparent circle diameter can be transformed to the true sphere diameter by a factor of $4/\pi$;

however, for a distribution of powder sizes, the inversion is not as simple [109-110]. The second experimental artifact addressed is that for a given section of the volume, a large sphere is more likely to be sampled than a smaller sphere. The final two experimental effects are that thin, transparent sections from some sample fabrications measure the diameter from a projection of a section with a certain thickness, and the other that a section near the edge of the powder radius may result in a section on the order of the resolution of the instrument [35]. Of the four effects, the first two are expected to significantly impact the inversion of the observed circle diameters to the real sphere diameters, while the last two will have limited impact on the results for a bulk ceramic imaged by microprobe.

The elements of F_{ij} are thus calculated for arithmetic binning by

$$F_{ij} = \begin{cases} \Delta\sqrt{(j-1/2)^2-(i-1)^2} - \sqrt{(j-1/2)^2-i^2}, & \text{if } i \neq j \\ \Delta\sqrt{(j-1/2)^2-(i-1)^2}, & \text{if } i = j \end{cases} \tag{31}$$

where Δ is the bin width, and for geometric binning by

$$F_{ij} = d_i\left[\sqrt{1-c^{2(i-j-1)}} - \sqrt{1-c^{2(i-j)}}\right] \tag{32}$$

where c is a constant ratio between a successive bin and the present bin. The derivation of the terms is left to be described by the original literature. The solution to the linear system in Eq. 30 is determined by the optimization scheme reported by Benito *et al.* which restricts the solution to nonnegative values, consistent with the physical reality of the solution [115].

To recover the three-dimensional size distribution from the observed two-dimensional sections here, the area data obtained from ImageJ is fit to a model to smooth the distribution, as recommended in the literature, and accepted if the Kolmogorov-

Smirnov test fails to reject the null hypothesis at the default 5% significance level. The fit continuous distribution function and data is binned using Scott's normal reference rule as a guideline which calculates the bin width (h) by the equation

$$h = \frac{3.49\sigma}{\sqrt[3]{N}} \tag{33}$$

where σ is the standard deviation and N is the number of data points; however, bin width selection is generally flexible and the fit distribution imparts greater tolerance to decreased bin width [116].

The area data is converted to diameter by assuming a circular cross-section and transforming the bin edges accordingly. The histogram resulting from the apparent area data weighted by number is termed N_A. Following the inversion by the scheme described by Benito *et al.*, the histogram reflects the expected distribution obtained from the true volume data weighted by number and is termed N_V. The contributions to the improvement in thermal conductivity, however, are better described by the volume occupied by a particle ensemble. Thus, the true, volume-weighted data, V_V, is determined by the equation

$$V_V(d_i) = N_V(d_i) \cdot \frac{4}{3}\pi \left(\frac{d_i + d_{i-1}}{4}\right)^3 \Big/ \sum_i V_V(d_i) \cdot \Delta \tag{34}$$

where d is the bin upper edge and Δ is the bin width. The average particle size, $\bar{d}$, is then determined by the equation

$$\bar{d} = \sum_i V_V(d_i) \cdot \Delta \cdot \frac{d_i + d_{i-1}}{2} \Big/ \sum_i V_V(d_i) \cdot \Delta \tag{35}$$

Equation 34 and Eq. 35 can also be adapted from arithmetic to geometric binning to provide adequate resolution at the lower diameter range by using the variable bin width described by the ratio c described in Eq. 32. Using $\bar{d}$ and the experimental data for k_{eff} and f corrected to 95%TD, the interfacial thermal resistance, R, and the component thermal conductivities, k_m and k_p, are determined by fitting Eq. 29 by a robust nonlinear least-squares method.

The methodology to fabricate and characterize dispersed UO_2-BeO composite microstructures has been described in the preceding chapter. The approach reduces the error identified in the literature review by fabricating a well-characterized microstructure while preserving the fabrication process. The interfacial thermal resistance reported here thus contributes to the informed microstructure design for optimized thermal conductivity. The following chapter presents the results of the fabrication process, the thermophysical property measurements, micrographs of the microstructure, and the image analysis data obtained from the micrographs. The results will be discussed in Chapter 5 to calculate the interfacial thermal resistance, implement in an analytical model of the microstructure, and discuss the relevance to the previous literature.

4. RESULTS

The first set of results, reported in Section 4.1, aimed to evaluate the quality of the fabricated UO_2-BeO composites prior to the application of analytical methods to infer physical properties. The fabrication by co-sintering, characterization of the density by various methods and the thermal diffusivity by light flash analysis and of the microstructure are reported in the following subsections. From the reported properties in Section 4.1, the thermal conductivity was calculated and corrected to a uniform porosity. Micrographs of the microstructure and the quantitative stereology data are also presented in Section 4.2. Finally in Section 4.3, the analytical expression reported by Zhu *et al.* for the continuous microstructures is validated against the available data.

4.1. Thermal and Physical Property Analysis

Two sets of samples of UO_2 and composites of 5, 10, and 15 vol.% BeO in UO_2 were fabricated using the procedure given in Section 3.1 with BeO granule diameters between 425 μm and 300 μm, the larger granule size indicated by the L-series of samples, and between 250 μm and 150 μm, the smaller granule size indicated by the S-series of samples. Based on the final powder mass, the experimental samples are all expected to be within 0.3 vol.% of the stated BeO concentration. The intended concentrations and the associated theoretical density for the composites are given in Table 1. The dispersed, granulated BeO microstructure in a matrix of UO_2 is shown in Fig. 4.1 with an abbreviated identifier. The final set of composite disks used for this study were mechanically robust, pictured following sectioning by diamond saw and largely free of defects, such as cracks,

chips and voids, although some grain or granule pullout was observed upon polishing. Previous work fabricating dilute, dispersed UO_2-BeO composites exhibited comparatively large fractions of open porosity which influenced the thermal diffusivity measurement or wide particle size distributions difficult to summarize as a single granule radius.

Table 1 Theoretical density data for the samples produced as calculated using a volumetric weighting of the reference densities for UO_2 and BeO

Sample Identifier	BeO Concentration	Theoretical Density (g/cm^3)
L-0	0 vol.%	10.96
L-5	4.9 vol.%	10.57
L-10	9.7 vol.%	10.19
L-15	14.7 vol.%	9.80
S-0	0 vol.%	10.96
S-5	5.0 vol.%	10.56
S-10	10.0 vol.%	10.17
S-15	14.9 vol%	9.78

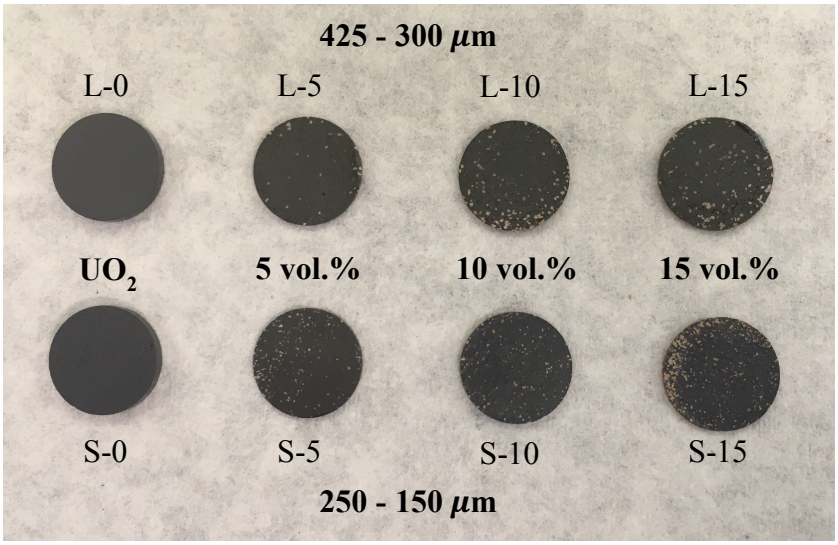

Figure 4.1 The samples fabricated for this work with those fabricated by the larger granules on the top with increasing BeO concentration from left to right and those fabricated with the smaller granules on the bottom row

The physical property measurements were collected in the center, approximately 2 mm thick, polished section of the full as-fabricated sample with roughly 1 mm of thickness removed from both sides. The average of the measured dimensions and the dry mass, average of the measured immersed mass, and average of the measured wetted mass are reported in Table 2. The density of ethanol, the working fluid, was measured as 0.7882 g/cm^3. The sample densities, as measured by the methods described in Section 3.2, are reported in Table 3 relative to the theoretical density in Table 1.

Table 2 The mass and dimension measurements of the UO_2-BeO composites used to calculate the density by the geometry, pycnometer, and immersion method

Sample	Average Thickness (mm)	Average Diameter (mm)	Dry Mass (g)	Immersed Mass (g)	Wetted Mass (g)
L-0	1.88	12.75	2.4692	2.2824	2.472
L-5	1.90	12.90	2.4064	2.2170	2.413
L-10	2.01	12.97	2.4969	2.2964	2.506
L-15	2.10	13.06	2.4982	2.2921	2.509
S-0	1.90	12.73	2.5013	2.3121	2.505
S-5	2.03	12.84	2.5928	2.3896	2.598
S-10	1.75	12.95	2.1669	1.9910	2.173
S-15	2.05	13.14	2.4399	2.2314	2.449

Table 3 The experimental densities measured from the geometry and by pycnometer and immersion methods presented as the percent of the theoretical density given in Table 1

	Geometry	Pycnometer	Immersion		
Sample	Bulk Density	Solid Density	Bulk Density	Solid Density	Open Porosity
L-0	93.8%	95.3%	93.4%	95.0%	1.7%
L-5	91.6%	96.0%	91.6%	94.7%	3.3%
L-10	92.3%	97.7%	92.0%	96.3%	4.5%
L-15	90.6%	99.2%	92.6%	97.5%	5.0%
S-0	94.3%	94.9%	93.5%	95.0%	1.7%
S-5	93.4%	95.8%	93.1%	95.2%	2.3%
S-10	92.4%	96.3%	92.5%	95.5%	3.1%
S-15	89.7%	96.3%	90.5%	94.3%	4.1%

The results show a solid density aligned with the industry goal for fuel of 95% of the theoretical density and within the range indicated in Fig. 3.5 and 3.6. Complementary techniques for measuring the bulk and solid densities were largely in good agreement, within 2% of one another, indicating near cylindrical geometry and accuracy of the immersion method, respectively. In general, the measured solid density increased with the addition of increasing concentrations of BeO, although not enough to compensate for the increasing open porosity. Similarly, by pycnometer, the composites formed with the larger granules had a higher solid density than those formed with the smaller granules; however, they also had a higher open porosity with the introduction of the BeO. The low uncertainty associated with the density correlations utilized and the immiscibility of UO_2 and BeO support the observed trends accuracy.

The thermal diffusivity of the samples, measured by LFA and without porosity correction, are presented in Fig. 4.2 and Table 4. Using Eq. 6 and the correlations presented for the specific heat and density in Chapter 3, the thermal conductivities of the composites are calculated and presented in Fig. 4.3 without porosity correction. The thermal conductivity values presented in Fig. 4.4 and Table 5 are corrected to 95% of the predicted theoretical density using Eq. 24 and the solid density as measured by pycnometer for the experimental porosity. When corrected to a uniform porosity, the results for the small and large granules diverge, questioning the suitability of the large granule samples for determining the interfacial thermal resistance by the flash method. A comparison of the L-series and S-series results are discussed in detail in Section 5.1 concluding the L-

series are inappropriate for inclusion in the present work. For this reason, the microstructure characterization results in Section 4.2 focus on the S-series of samples.

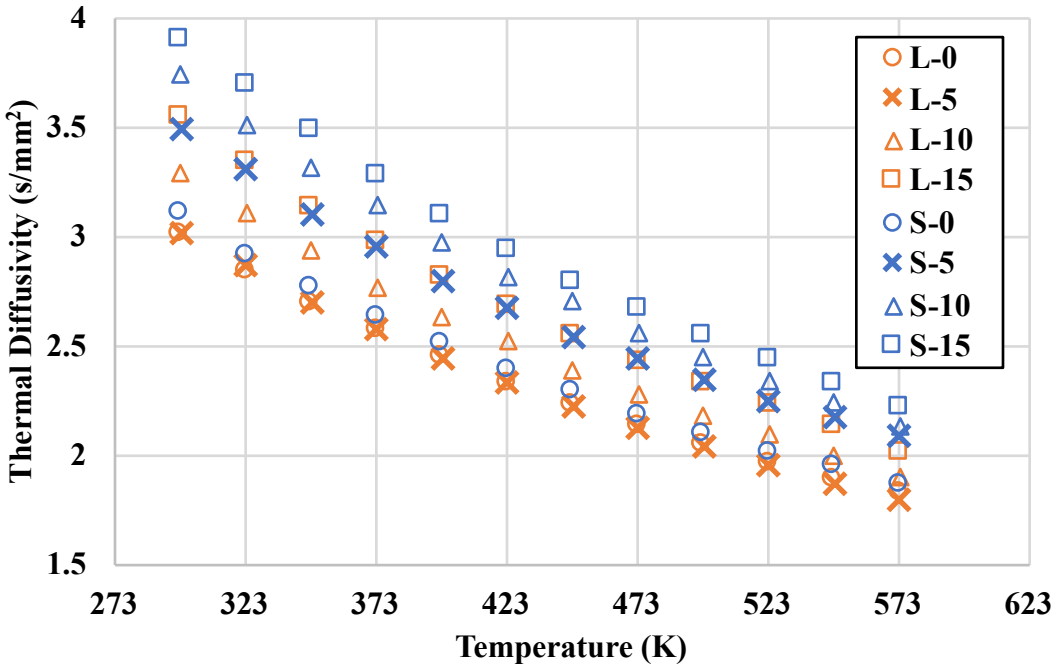

Figure 4.2 The thermal diffusivity of the UO_2 and dispersed BeO composites with a carbon coating as measured by LFA

Table 4 The thermal diffusivity values (s/mm^2) measured by LFA for the UO_2 and dispersed BeO composites with carbon coating displayed in Fig. 4.2

Temperature (K)	L-0	L-5	L-10	L-15	S-0	S-5	S-10	S-15
298	3.02	3.02	3.30	3.55	3.12	3.49	3.75	3.91
323	2.84	2.87	3.11	3.34	2.92	3.31	3.52	3.70
348	2.69	2.71	2.94	3.14	2.77	3.11	3.32	3.49
373	2.57	2.58	2.78	2.98	2.64	2.96	3.14	3.28
398	2.45	2.45	2.64	2.82	2.51	2.80	2.97	3.10
423	2.34	2.34	2.53	2.68	2.39	2.68	2.82	2.94
448	2.23	2.23	2.39	2.55	2.29	2.55	2.70	2.80
473	2.14	2.13	2.29	2.43	2.19	2.45	2.56	2.67
498	2.05	2.04	2.19	2.33	2.10	2.35	2.45	2.55
523	1.97	1.95	2.10	2.23	2.02	2.25	2.35	2.44
548	1.89	1.87	2.00	2.13	1.95	2.18	2.25	2.33
573	1.83	1.80	1.91	2.01	1.87	2.09	2.14	2.22

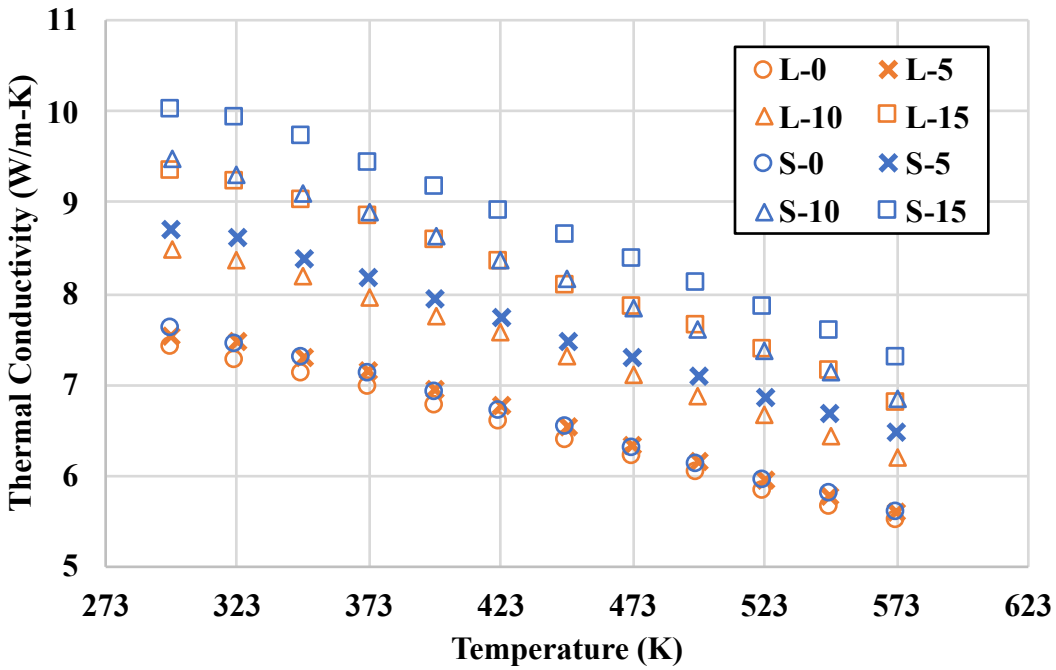

Figure 4.3 The thermal conductivity of the UO_2 and dispersed BeO composites calculated using Eq. 6

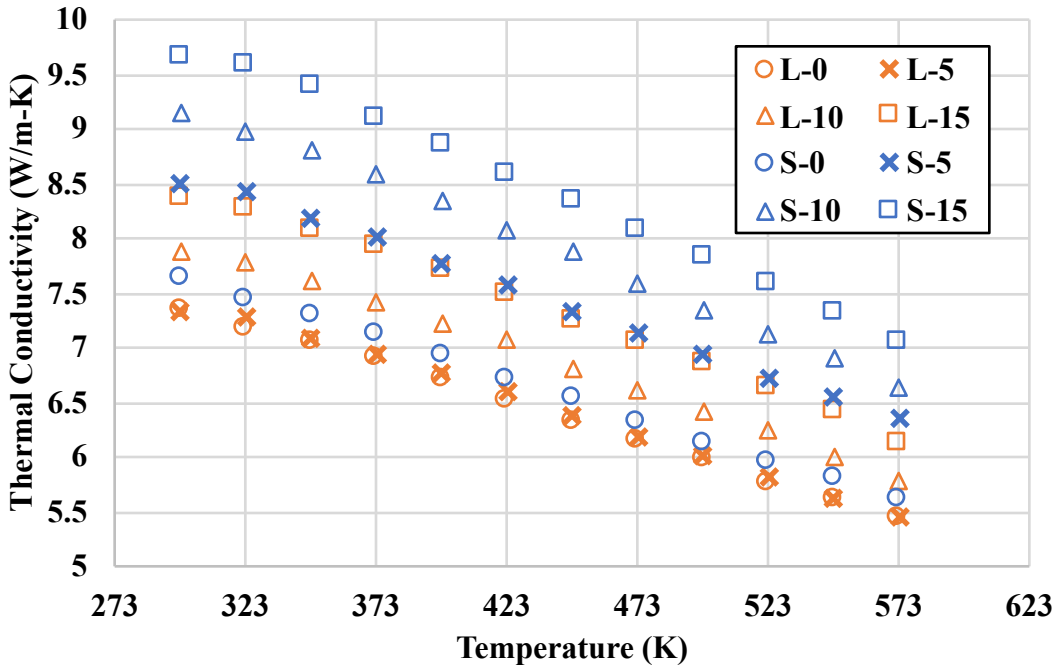

Figure 4.4 The thermal conductivity of the UO_2 and dispersed BeO composites corrected to a uniform 95%TD using Eq. 24

Table 5 The thermal conductivity values (W/m-K) of the UO_2 and dispersed BeO composites corrected to a uniform 95%TD using Eq. 24 displayed in Fig. 4.4

Temperature (K)	L-0	L-5	L-10	L-15	S-0	S-5	S-10	S-15
298	7.33	7.35	7.88	8.36	7.63	8.51	9.15	9.65
323	7.19	7.29	7.78	8.26	7.45	8.42	8.99	9.58
348	7.04	7.10	7.62	8.07	7.30	8.19	8.80	9.39
373	6.90	6.95	7.41	7.93	7.12	8.02	8.59	9.11
398	6.71	6.76	7.23	7.70	6.93	7.78	8.33	8.85
423	6.52	6.60	7.07	7.49	6.71	7.57	8.08	8.59
448	6.33	6.38	6.82	7.26	6.54	7.33	7.88	8.33
473	6.15	6.18	6.62	7.05	6.32	7.14	7.58	8.08
498	5.97	6.01	6.43	6.86	6.13	6.94	7.35	7.82
523	5.77	5.81	6.24	6.64	5.96	6.73	7.13	7.58
548	5.60	5.63	6.01	6.43	5.81	6.56	6.91	7.33
573	5.45	5.46	5.78	6.11	5.62	6.35	6.63	7.06

4.2. Microstructure Characterization and Quantitative Stereology

To quantify the granule diameter, the composite microstructure was imaged using a Cameca SXFive Electron Microprobe. The composite microstructure imaged by backscatter electron (BSE) and secondary electron (SE) modes is shown in Fig. 4.5. The SE micrograph is primarily sensitive to the surface topography of the sample with an additional contribution of the atomic mass. It is apparent from the micrograph that the surface topography obscures the feature of interest here, the granule area. The BSE mode is primarily sensitive to the atomic mass of the interaction volume with an additional contribution of the surface topography. BSE micrographs at two contrast levels are also shown in Fig. 4.5. Compared to SE mode, BSE mode is less effected by the surface topography and can clearly capture the granule area. At lower contrast, pores and surface topography are visible within each phase; however, the high contrast image is more ideal for quantitative stereology, filtering features that are not BeO without impacting the granule area measurement.

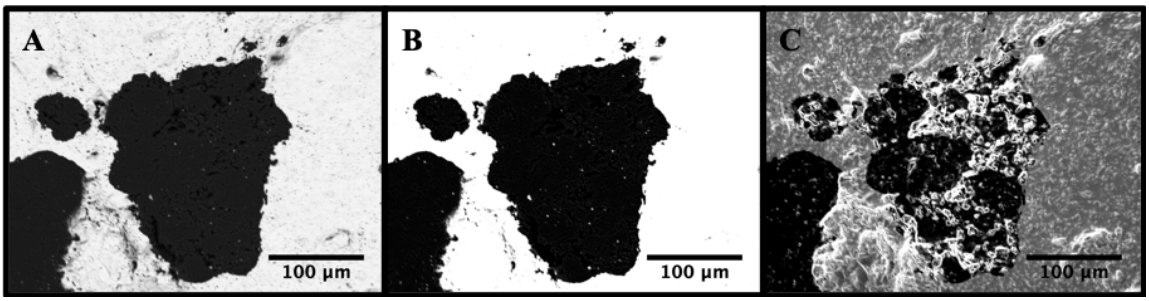

Figure 4.5 Micrographs of a BeO granule (dark) in a UO_2 matrix (gray or white) imaged at low contrast in BSE mode (A), at high contrast in BSE mode (B), and in SE mode (C) showing the impact of imaging mode on the evaluation of the BeO granule size

More illuminating micrographs of the UO_2 and BeO phases are shown in Fig. 4.6 and Fig. 4.7 separately because the high atomic number contrast leads to varying optimal microscope settings. The UO_2 phase in samples S-0 and S-5 are shown in SE and BSE modes in Fig. 4.6 to be similarly high density with the surface texture limiting the utility of quantitative analysis of the porosity. The BeO phase is shown only in BSE mode in Fig. 4.7. High brightness and contrast were required to distinguish between the BeO phase, texture, and pores rendering SE mode too bright with the contribution of the edge effects. Disregarding the visible texture, the BeO phase is also shown to be high density; however, local areas of lower density are visible, potentially due to poor powder packing accumulated during self-milling.

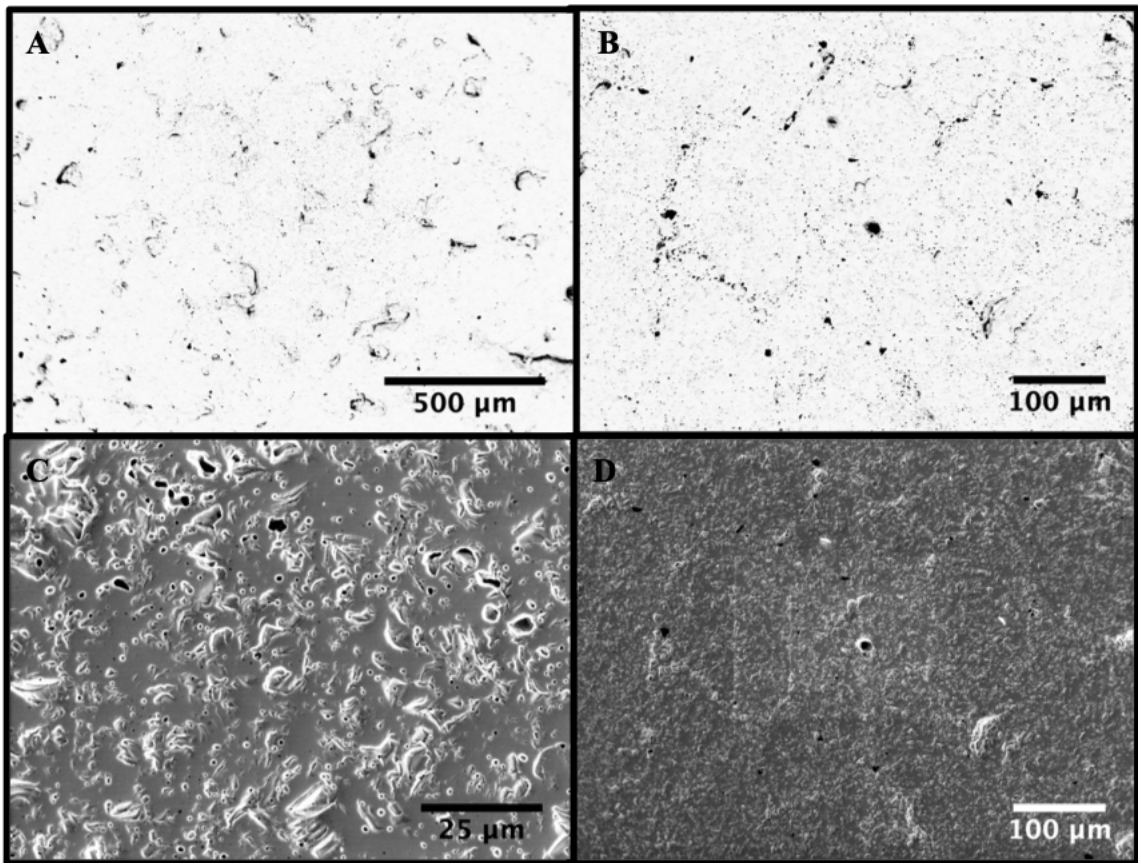

Figure 4.6 Micrographs of UO_2 in BSE mode (A,B) and SE mode (C,D) of S-0 (A,C) and S-5 (B,D) at varying magnifications showing the qualitative similarity in resultant microstructure and the impact of imaging mode on UO_2 micrographs

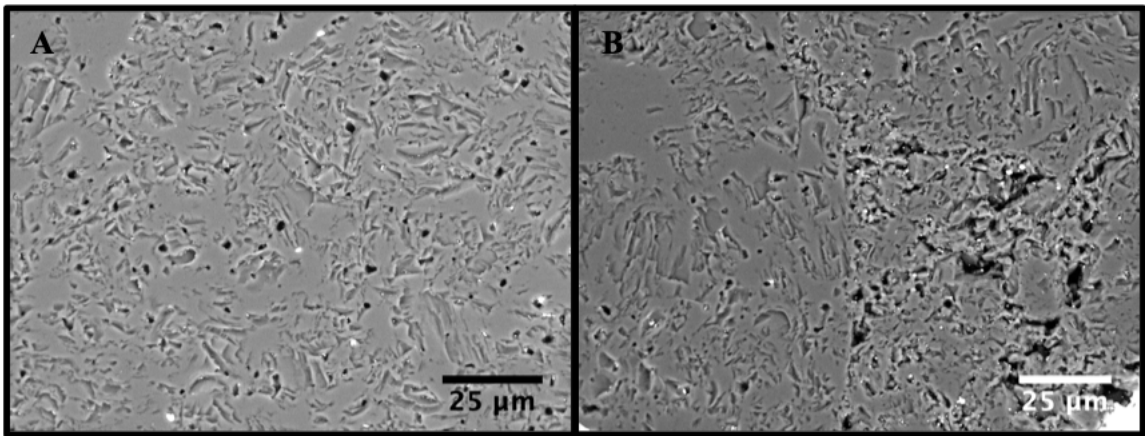

Figure 4.7 BSE micrograph of a BeO granule showing high density area (A) and a comparatively lower density area (B)

The origin of the surface texture on an otherwise well-polished sample is unclear but is pervasive enough to limit the utility of secondary electron micrographs for quantitative stereology. Backscatter electron mode shows high contrast between the UO_2 and BeO phases. The high contrast BSE images collected across the microstructure are demonstrated in Fig. 4.8. Prior to analysis in ImageJ, a selective color change process was performed to ensure singular counting of BeO granules and elimination of features with the same gray level. Figure 4.9 shows an original micrograph and the micrograph following image processing.

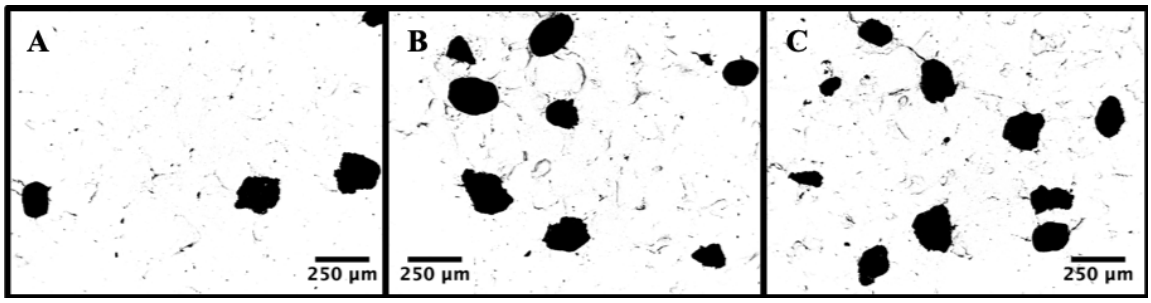

Figure 4.8 High contrast, BSE micrographs of S-5 (A), S-10 (B), and S-15 (C) of the UO_2 matrix (white) with BeO granules (black) demonstrating the input files for quantitative stereology in ImageJ

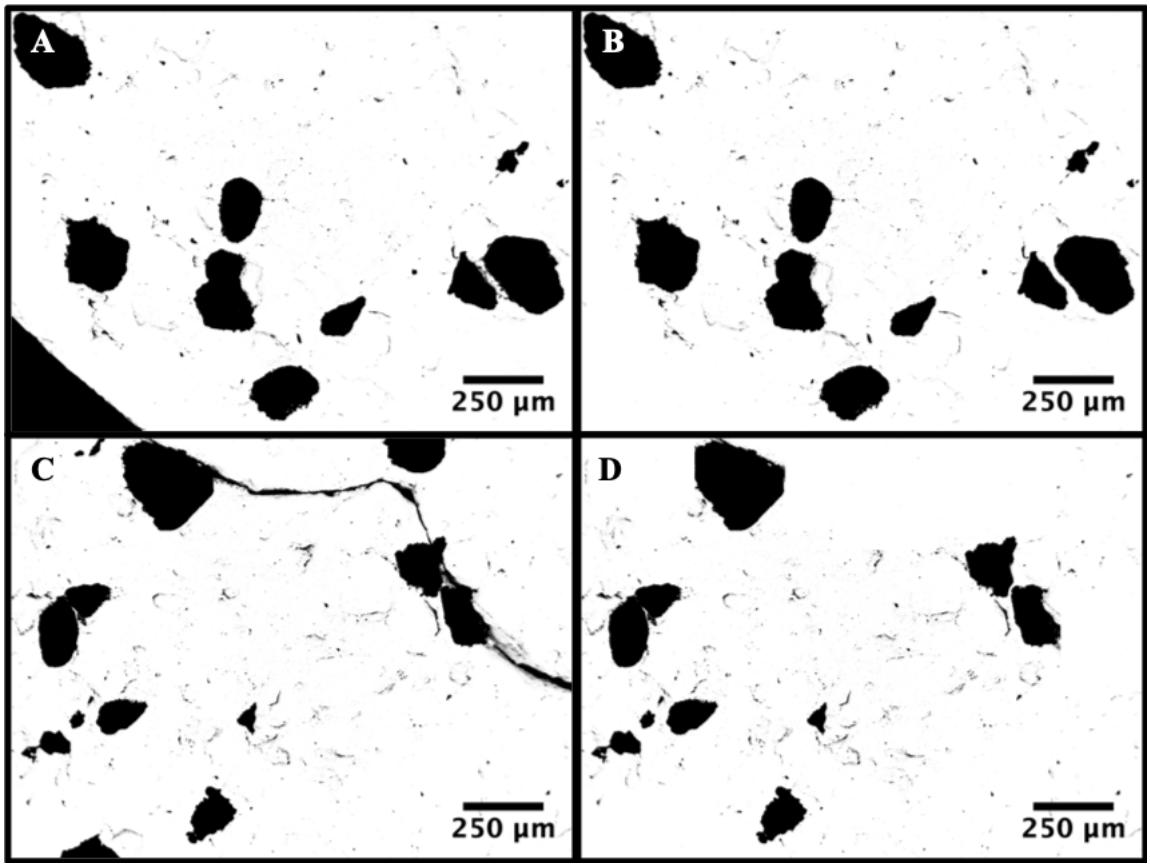

Figure 4.9 Micrographs demonstrating the application of selective color change processing on features with the same gray level as BeO, such as epoxy at the sample edge (from A to B) and sample defects (from C to D), and to remove particles intersecting the frame

The results of the quantitative stereology performed by ImageJ are presented in Fig. 4.10. For each sample and for all of the BeO granule area data, the empirical cumulative distribution function is plotted both against the as-measured area and the equivalent diameter. The total number of sampled granule cross-sections for each sample is presented in Table 6. From the data, Scott's normal reference rule suggests using 7, 11, 12, and 16 histogram bins to represent the distributions of S-5, S-10, S-15, and all of the data, respectively [116]. The resulting histogram for each sample is presented in Fig. 4.11.

The data sets' means, medians, and ranges and the histograms' modes are reported in Table 6 for comparison. The mode is reported as the midpoint between the bin edges of the bin with the largest frequency, with the exception of S-5 where the bin with the second largest frequency is reported. The first largest frequency bin for S-5 is the first bin; however, it is expected to be due to the smaller sample size. The bins are also presently weighted by number, while a volume-weighted frequency would suppress the first bin and be more representative of the contribution to thermal conductivity.

Table 6 The summary statistics for the BeO granules size for the S-5, S-10, and S-15 samples and the entire data set

	S-5	**S-10**	**S-15**	**ALL**
N	213	386	464	1063
Range (μm)	17.5-310.7	23.7-400.3	21.0-424.1	17.5-424.1
Mean (μm)	157.5	168.8	166.1	165.4
Median (μm)	152.9	153.0	150.0	151.8
Mode (μm)	164.1	143.5	172.2	157.3

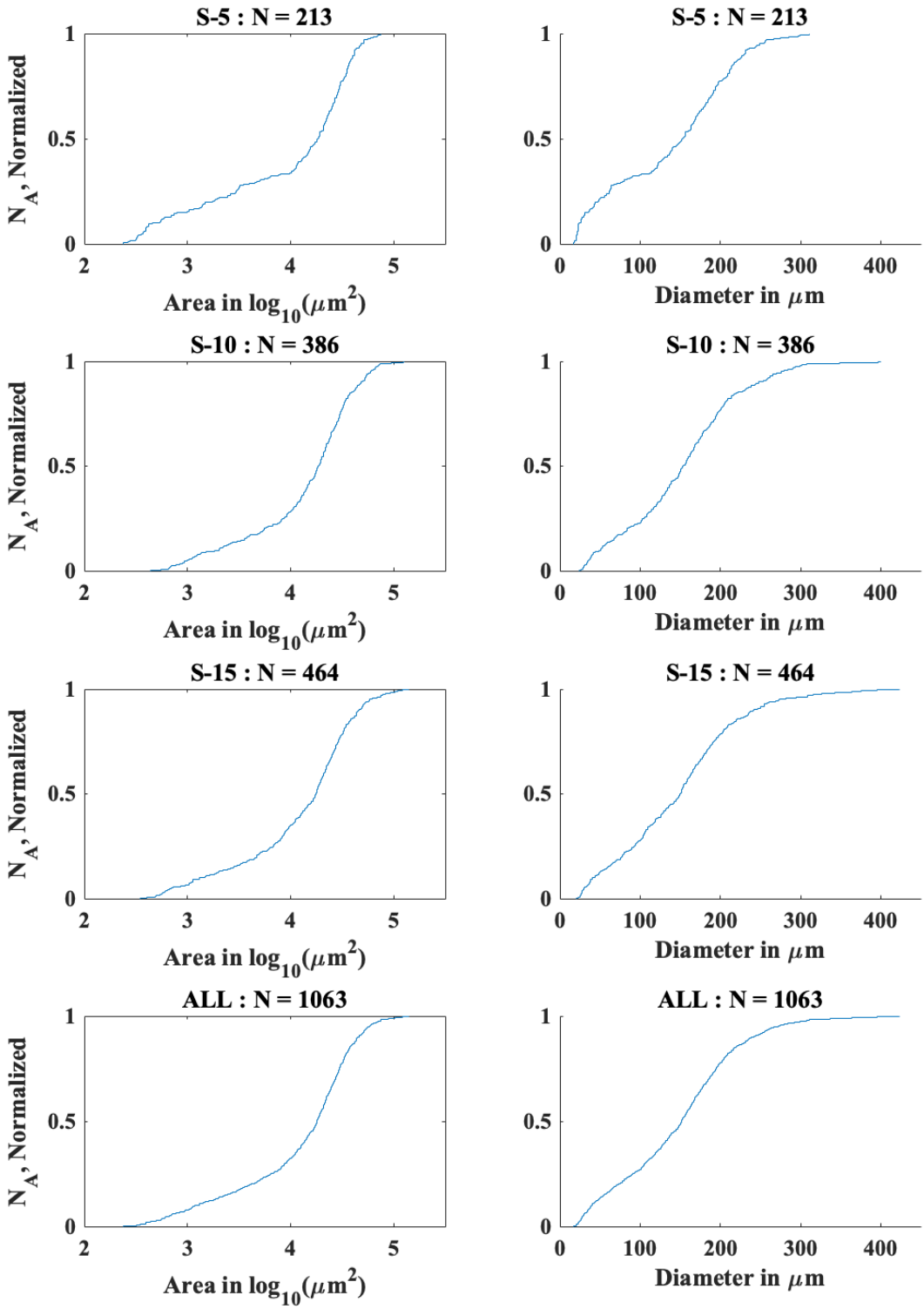

Figure 4.10 The empirical cumulative distribution functions for the BeO granule size for the S-5, S-10, and S-15 samples and the entire data set against the measured area (left) and the equivalent diameter (right) normalized to unity

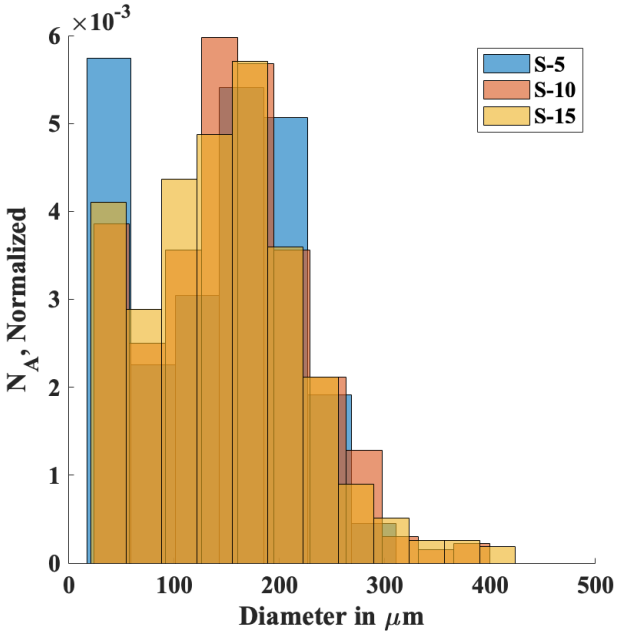

Figure 4.11 The data for each sample binned according to Scott's normal reference rule and normalized to compare the distribution of equivalent diameters observed

The raw data shows reasonable agreement between the observed granule sizes for the three samples. As the BeO concentration increases, the range extends to larger values, suggesting some agglomeration of granules; however, the other summary statistics do not consistently trend similarly. After an initial increase in the mean, the mean decreases for S-15, despite having the largest range. The median of the data sets does not change significantly. The changes in the mode value in Table 6 are likely more related to the location and width of the bins for each data set rather than the underlying data as they nearly overlap in Fig. 4.11. The lowest concentration sample does have a higher share of small particles; however, it also has the lowest sample size. If the granule size distributions are expected to be indistinguishable, the full data set can be used to represent all of the samples. The histogram of the full data set is shown in Fig. 4.12.

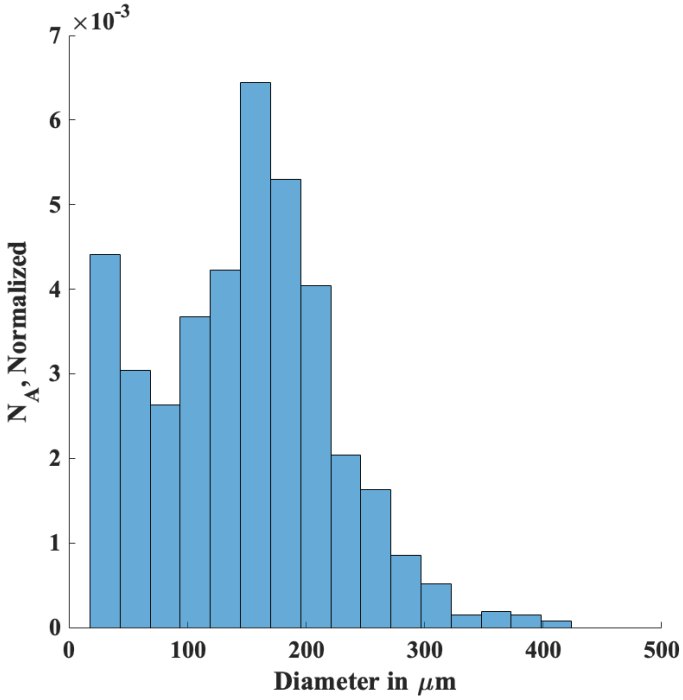

Figure 4.12 The data for all of the sampled granule cross-sections binned according to Scott's normal reference rule and normalized to compare to the individual sample distributions and smooth statistical fluctuations associated with low sample sizes

Using the inversion technique described by Eq. 30 and 31 and the method to convert the number-weighted data to volume-weighted by Eq. 34, the true distribution is calculated from Fig. 4.11 and 4.12. The results for each sample and the full data set are shown in Fig. 4.13-4.16. The number-weighted distribution (left) is binned with both arithmetic and geometric spacing to resolve the distribution for smaller diameters.

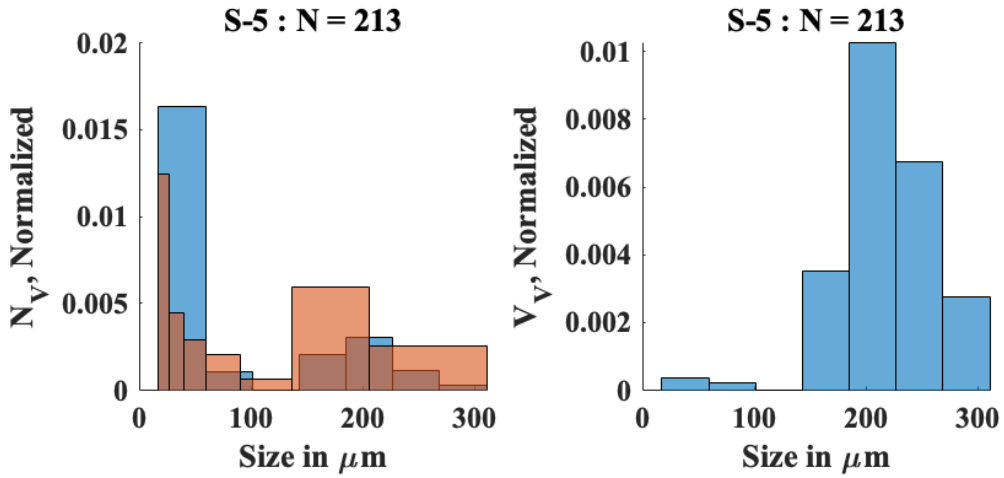

Figure 4.13 The true diameter distribution for S-5 recovered from the observed apparent diameter distribution by stereological inversion displayed with each granule weighted equally (left) with equally spaced arithmetic binning, and geometric binning for resolution at lower diameters, and with granule frequency weighted by volume (right)

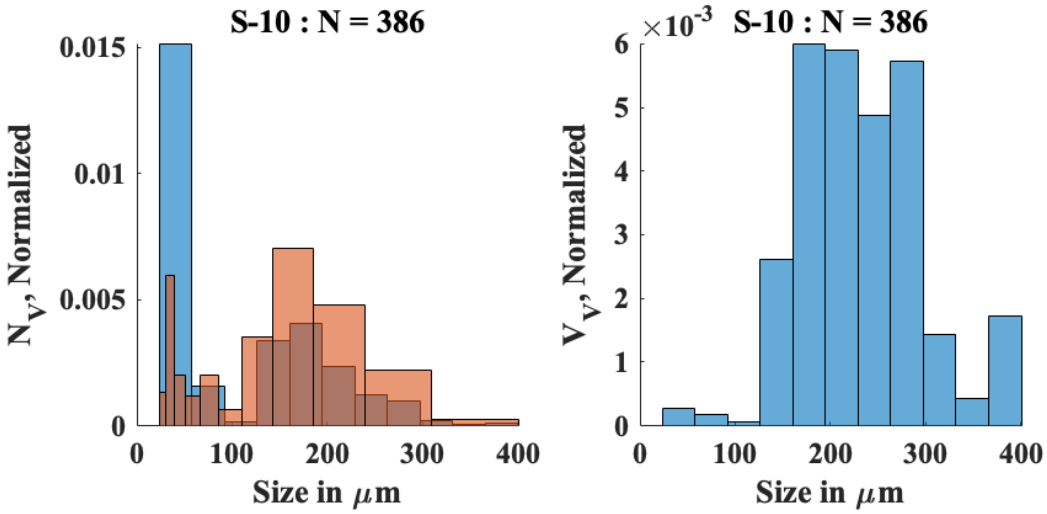

Figure 4.14 The true diameter distribution for S-10 recovered from the observed apparent diameter distribution by stereological inversion displayed with each granule weighted equally (left) with equally spaced arithmetic binning, and geometric binning for resolution at lower diameters, and with granule frequency weighted by volume (right)

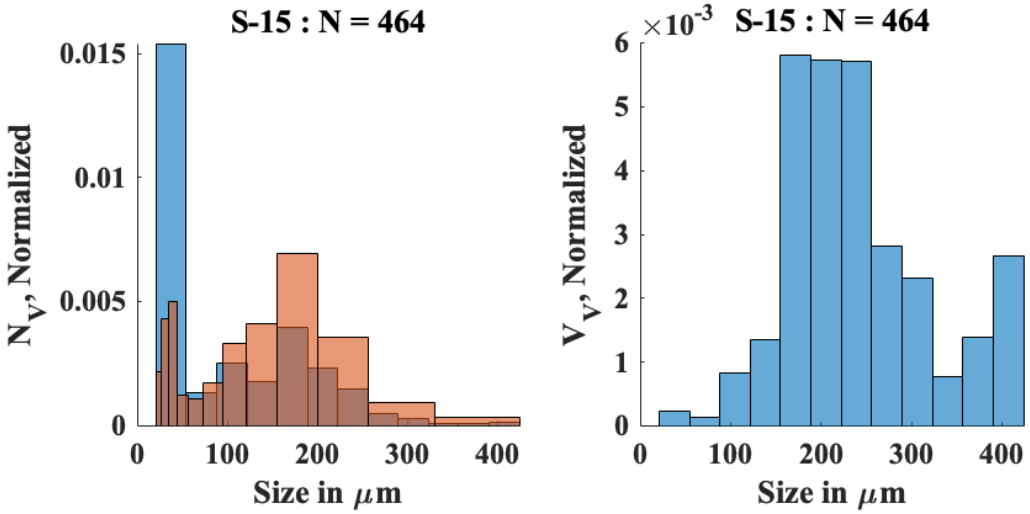

Figure 4.15 The true diameter distribution for S-15 recovered from the observed apparent diameter distribution by stereological inversion displayed with each granule weighted equally (left) with equally spaced arithmetic binning, and geometric binning for resolution at lower diameters, and with granule frequency weighted by volume (right)

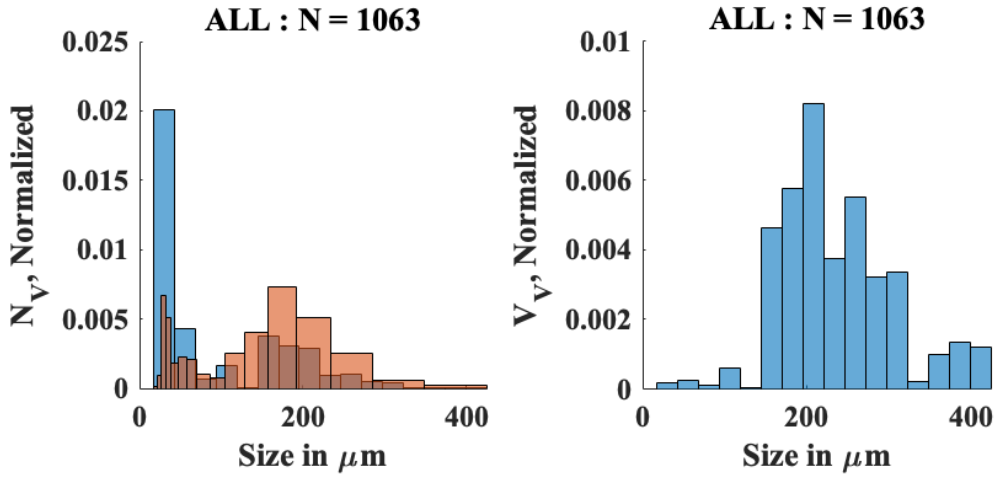

Figure 4.16 The true diameter distribution recovered from the observed apparent diameter distribution of all the observed data displayed with each granule weighted equally (left) with equally spaced arithmetic binning, and geometric binning for resolution at lower diameters, and with granule frequency weighted by volume (right)

The results of the inversion procedure, converting the apparent diameter distributions in Fig. 4.11 and Fig. 4.12 to the true diameter, show an increase in the count

of low diameter granules across all of the samples; however, the granules occupy a negligible volume, with the majority of the volume between the targeted sieve size of 150 to 250 µm. The number-weighted true distribution for each sample can be compared directly in Fig. 4.17 and the volume-weighted true distribution in Fig. 4.18. The mean diameter for each volume-weighted histogram and mode is reported in Table 7. Only the bin edges and histogram frequency pass through the inversion process, so a specific median value is not reported and the sample size (N) and range do not change.

Table 7 The summary statistics for the true BeO granule size for the S-5, S-10, and S-15 samples and the entire data set following stereological inversion

	S-5	**S-10**	**S-15**	**ALL**
Mean (µm)	221.0	234.7	243.3	237.1
Mode (µm)	206.0	177.8	172.18	208.1

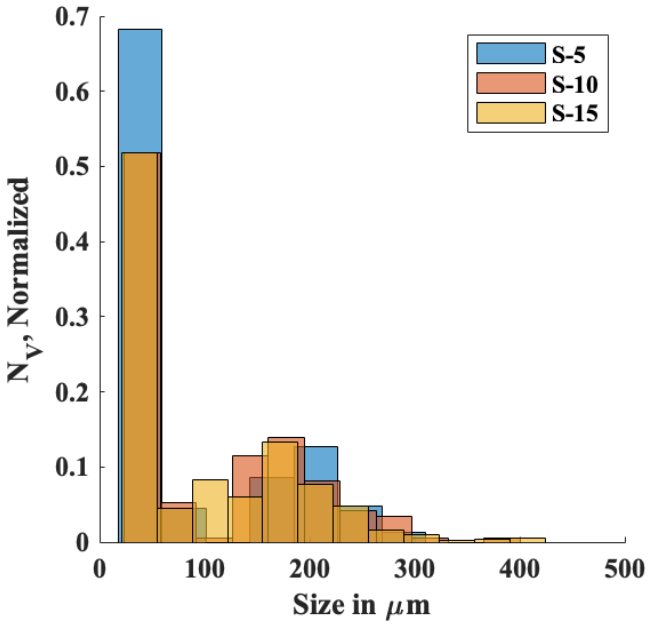

Figure 4.17 A comparison of the number-weighted true diameter frequency of each of the UO_2-BeO samples fabricated

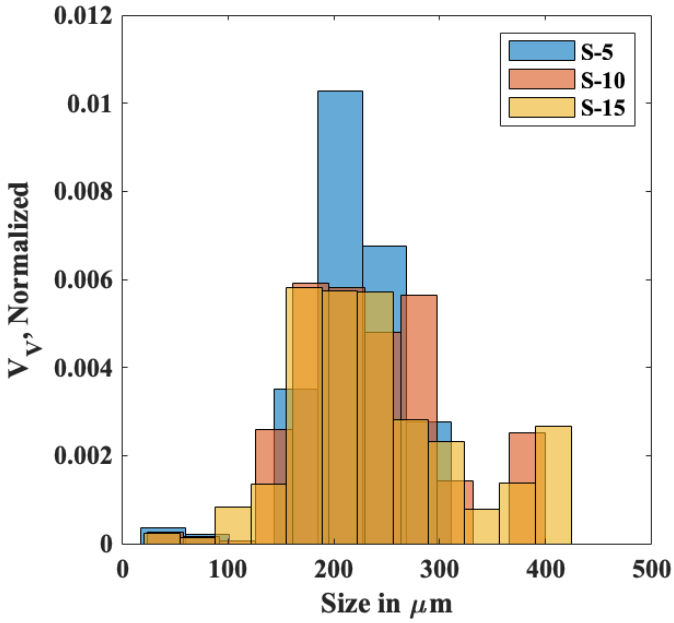

Figure 4.18 A comparison of the volume-weighted true diameter frequency of each of the UO_2-BeO samples fabricated

4.3. Analytical Model of the Continuous Microstructure by Equivalent Resistance

The results reported thus far are discussed further in Chapter 5 and analyzed to determine the true particle diameter relevant to the thermal conductivity of the composite. With the reported results and the true particle diameter, the interfacial thermal resistance can be determined by Eq. 29. To understand the impact of the interfacial thermal resistance on the design of the continuous microstructure, however, the analytical expressions reported by Zhu *et al.* in Eq. 12 and Eq. 13 can be further validated by the reported results [16,27,49].

In the literature, Zhu *et al*. proposes an analytical model, given in Eq. 12 and Eq. 13, for the UO_2-BeO continuous microstructures; however, it is only validated against the results reported by Latta, Revankar, and Solomon. Recalling Latta, Revankar, and

Solomon simulated only two-dimensional, single geometry microstructures with no implemented interfacial thermal resistance, the literature neglects to validate the expression against simulation dimension, granule shape, or implementation of interfacial thermal resistance [26]. As reviewed in Chapter 2, the literature considers the impact of simulation dimension and granule shape unresolved, but the impact of the interfacial thermal resistance and the interplay with particle size is critical to capture to support an informed microstructure design.

The results as reported by Badry *et al.*, which this author contributed to, did not initially align well with the sharp-interface construction of the expression in Eq. 12. This work applied the method of equivalent resistance, the same method to develop Eq. 12 and Eq. 13, to a phase-field equivalent featuring a distinct interface region with the same width and thermal properties as the simulated domain. The model geometry can be seen in Fig. 4.19 showing a square geometry with side length l_m of UO_2 with thermal conductivity k_m surrounded by a thin region of BeO with thickness l_p and thermal conductivity k_p. An interface region of thickness l_i and thermal conductivity k_i separates the two on both sides. In the simulations reported by Badry *et al.*, the interface thickness was 1 nm and the thermal conductivity of the interface was represented by the equation

$$k_i = 0.95 k_m \left(\frac{k_m'}{k_m}\right)^3 \tag{36}$$

where k_m' represents the thermal conductivity at the reference temperature (573 K) that 0.95 was fit [27]. The terms in Eq. 36 excluding k_m outside of the exponent are represented

as r_f in the figure and subsequent equations. Using the method of equivalent thermal resistance, the two-dimensional expression to represent the Badry *et al.* data was derived

$$k_{eff} = \frac{r_f k_m}{l_m+l_p+2} + \frac{r_f k_m k_p l_p}{r_f k_m (l_m+l_p+1)+k_p} + \frac{r_f k_m k_p}{r_f k_m l_m + k_p l_p + 2k_p} + \frac{r_f l_m k_p k_m^2}{r_f k_m k_p l_m + 2k_m k_p + r_f l_p k_m^2} \quad (37)$$

with each term representing the contribution of a horizontal section of the model geometry in Fig. 4.19. For example, the first term represents the thin, continuous section of interface at the top of the model geometry while the last term represents the large area at the bottom of the model geometry of UO_2, interface, BeO, interface successive layers.

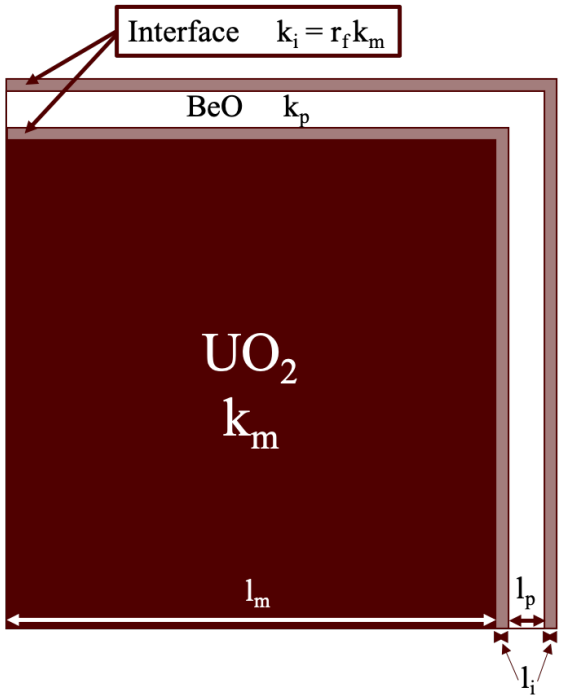

Figure 4.19 The model geometry for the application of the equivalent thermal resistance method to phase-field simulations of UO_2-BeO composites with continuous microstructures and an interfacial thermal resistance implemented in the interface region

Additional analysis of the results reported by Zhou *et al.* was also required to support the validation of the method of equivalent thermal resistance for representation of

continuous UO_2-BeO microstructures. Zhou *et al.* reports three model geometries included in this work, two-dimensional square, three-dimensional extruded hexagon, and three-dimensional pseudo-close packed octagon. For the two-dimensional square, constructed similarly to Latta, Revankar, and Solomon for comparison to the experimental results reported by Ishimoto *et al.* at 3.2 vol.%, the stated width of the BeO is doubled for this work to reflect the model geometry and result in the correct volume fraction. For both three-dimensional model geometries, Zhou *et al.* reports the model geometry reflects 3.4 wt.% or 9.7 vol.% BeO which are not equivalent. The volume fraction is correctly reported as 11.4 vol.% later, and the model geometries support that 11.4 vol.% was simulated. Additional reported model geometries and BeO concentrations were excluded if the reported model geometries did not result in either reported volume fraction or if the volume fractions were much larger than of interest here [16,27,49].

The results of the respective analytical models plotted in comparison to the simulated results of Latta, Revankar, and Solomon, Zhou *et al.*, and Badry *et al.*, which this author contributed to, are shown in Fig. 4.20. The relevant simulation parameters derived from the literature are given in Table 8, Table 9, and Table 10. For non-square, simulated granules shapes, the model geometries reported in literature were converted to equivalent cubic volumes or square areas. The porosity of the components in the model were also corrected by Eq. 24 for UO_2 and Eq. 25 for BeO to reflect the simulated values. These results add to the validation of the analytical expression the simulation of three-dimensional microstructures, diverse geometries, and an implemented interfacial thermal resistance.

Table 8 The microstructure parameters for the simulations reported by Badry *et al.* for continuous UO_2-BeO microstructures [Adapted from 27]

	2D Voronoi Diagram			
l_m (nm)	168.7		95.4	
l_p (nm)	3.30		3.16	
R (10^{-10} m^2-K/W)	0	1.55	0	1.55
Porosity	0	0	0	0

Table 9 The microstructure parameters for the simulations reported by Latta, Revankar, and Solomon for continuous UO_2-BeO microstructures [Adapted from 16]

	2D Square Grid	
l_m (µm)	157	109
V_P (vol.%)	2.1	4.2
R	0	0
Porosity	0.006	0.013

Table 10 The microstructure parameters for the simulations reported by Zhou *et al.* for continuous UO_2-BeO microstructures [Adapted from 49]

	2D Square Grid	**3D Hexagon**	**3D Octagon**
l_m (µm)	153	18.652	128.775
V_P (vol.%)	3.2	11.4	11.4
R	0	0	0
Porosity	.02	.05	.05

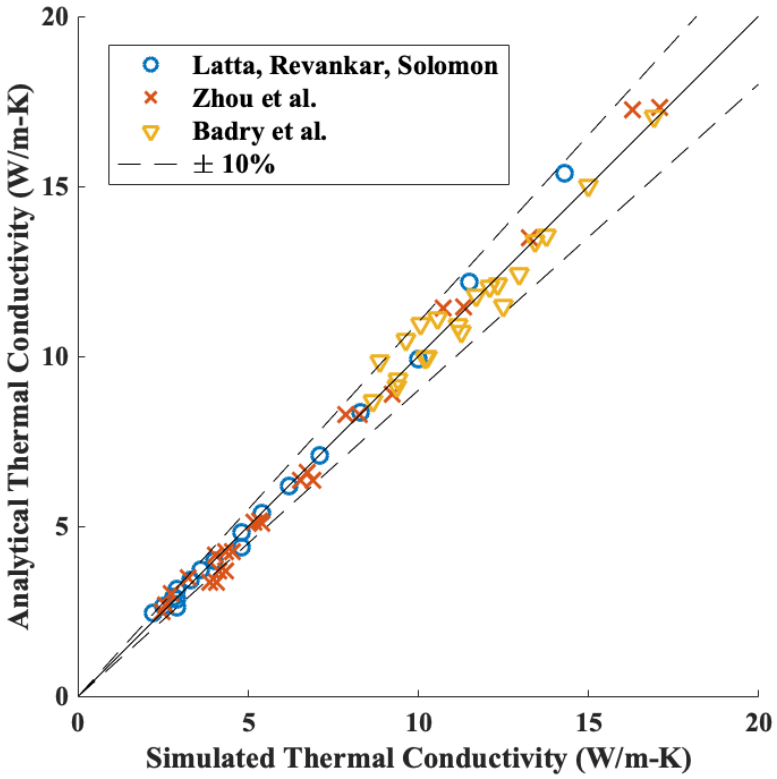

Figure 4.20 A comparison of simulated thermal conductivity results for UO_2-BeO continuous composites and the analytical prediction of the method of equivalent thermal resistance with ±10% around agreement [Adapted from 16,27,49]

5. DISCUSSION

This chapter considers the results presented in Chapter 4 and discusses the implications with respect to the expected outcomes, the desired application in further analysis, and within the literature. As mentioned in the literature review, this work seeks to improve the accuracy of the measurement of the interfacial thermal resistance in UO_2-BeO composites. Chapter 4 reported the cumulative results of the composite thermal conductivity values, highlighting the unexpected divergence between the two series of samples fabricated. Section 5.1 discusses this unexpected result with respect to the analytical methods and advises caution in the applicability of the L-series for the stated application.

In Section 5.2, the results of the quantitative stereology of the BeO granule size are discussed and evaluated by the inversion method. The granule size is necessary to determine the interfacial thermal resistance by the flash method; however, the presented results in Chapter 4 are of two-dimensional cross-sections of the three-dimensional microstructure. The analysis and discussion of these results ultimately provides a single, volume-weighted average granule diameter, grounded by the characterization results. The combination of the fabrication and characterization of this composite for the calculation of the interfacial thermal resistance is original in the literature.

Lastly in Section 5.3, the interfacial thermal resistance and the thermal conductivity of the composite components are calculated by the inverse problem and flash method using the outcomes resulting from the previous discussion. The calculated values

are discussed with respect to the literature to support the claim that this work offers improved accuracy. Finally, with the analytical method for the continuous microstructure identified in Chapter 4 and the calculated interfacial thermal resistance, the impact on the design of the microstructure for improved thermal conductivity is discussed.

5.1. Evaluation of the Thermophysical Properties of the Dispersed Microstructures

The calculation of the thermal conductivity using Eq. 6 is fairly straightforward with the method to determine the composite specific heat validated in the literature [33] and the experimental measurement of the thermal diffusivity reported in Section 4.1. The sample density, and by extension porosity, however, is not as clear, as suggested by the variety of measurement methods, porosity types, and porosity correction expressions in Section 3.2. The discussion focuses on resolving two issues and in the process understanding the results presented in Fig. 4.4: what porosity types contribute to the bulk behavior of the S- and L-series samples and what porosity correction expressions should be applied for uniform comparison between samples?

While the two-phase composite thermal conductivity equation given in Eq. 29 predicts a dependence on granule size, the overall impact should be small compared to the impact of the granule concentration. As shown in Fig. 4.4, the L-series thermal conductivity results are significantly lower than the S-series, with the 5 vol.% L-series exhibiting no improvement over UO_2 and the 15 vol.% L-series exhibiting lower thermal conductivity than the 5 vol.% S-series. While any individual result could be attributed to the interfacial thermal resistance, the lack of a systematic trend suggests otherwise.

Using the thermal conductivity equations for UO_2 and BeO given in general by Eq. 23, and the fabrication details in Table 3, the thermal conductivity of a fully dense composite can be explored for varying interfacial thermal resistance using Eq. 29. Equation 24 and the solid density measurements in Table 3 can adjust the results from Eq. 29 to reflect the closed porosity in each sample. Finally, the open porosity in Table 3 can be accounted for using Eq. 27 and Eq. 28 to consider two potential pore geometries. The results of this cumulative analysis for each sample are presented in Fig. 5.1-5.6.

For each figure, the experimental data is compared to a modeled scenario accounting for varying porosity types. The upper plot considers the modeled, bounding cases of no interfacial thermal resistance and an infinite interfacial thermal resistance for a sample with the given composition. The middle plot, building upon the fully dense predictions plotted as lines in the uppermost plot, corrects for the measured closed porosity. The bottom plot, building on the conditions plotted as lines in the middle plot, corrects for the measured open porosity, considering spherical pores and disc pores for each value of the interfacial thermal resistance. The data points for the experimental results do not vary between plots within the same figure but indicate the results a particular model should approximately return. The interfacial thermal resistance is expected to be close to zero, thus a positive result of this analysis (plotted as lines) would capture the experimental results (plotted as points) between the bounding interfacial thermal resistance values nearer zero; however, within the experimental error, if the analysis under predicts the experimental results, the impact of porosity on the bulk thermal conductivity is being over accounted for.

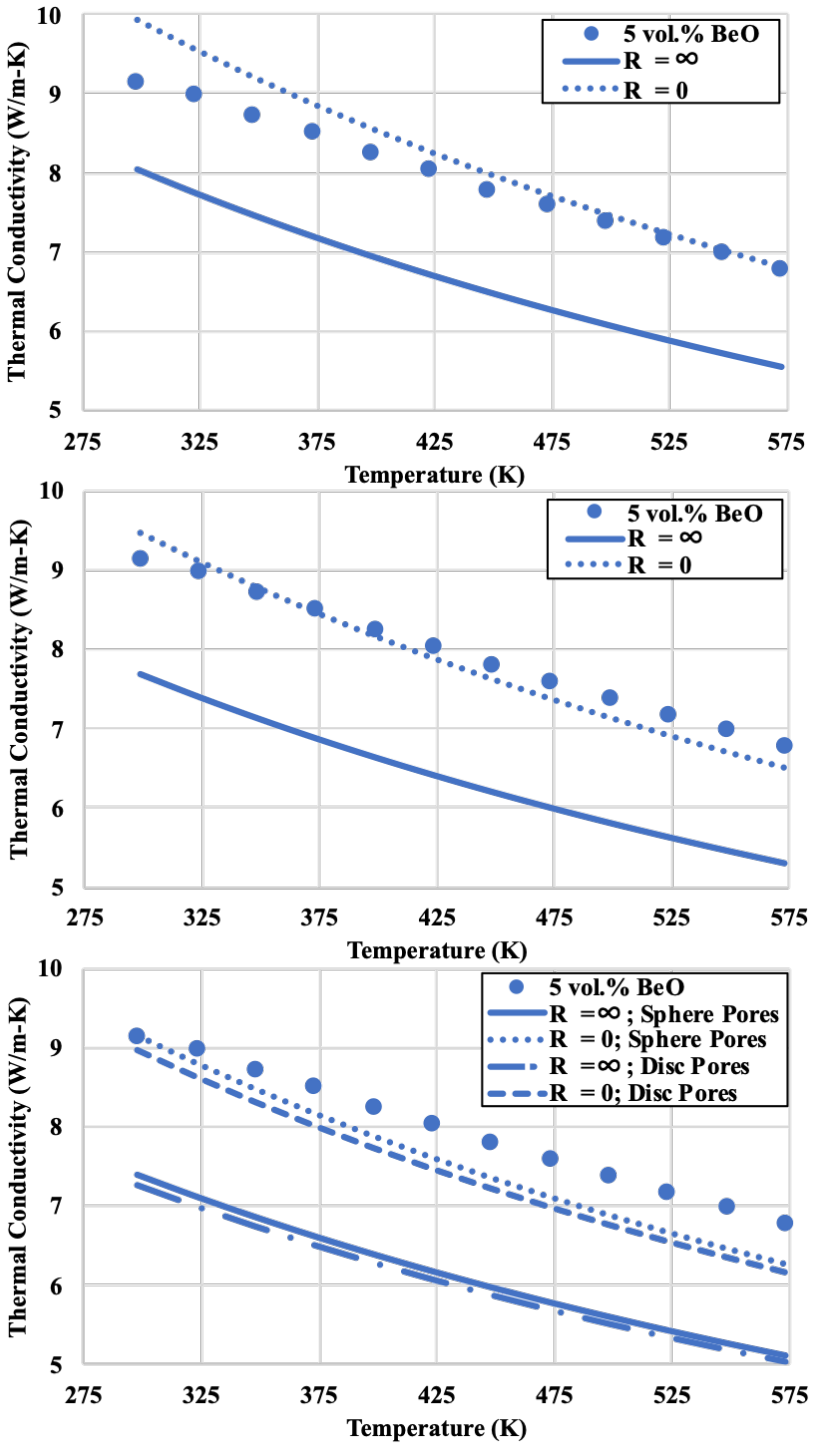

Figure 5.1 The experimental data (points) for S-5 compared to analytical predictions with an interfacial thermal resistance, R, for a fully dense model (top), a model including the closed porosity (middle), and a model including the open porosity (bottom) with two pore geometries

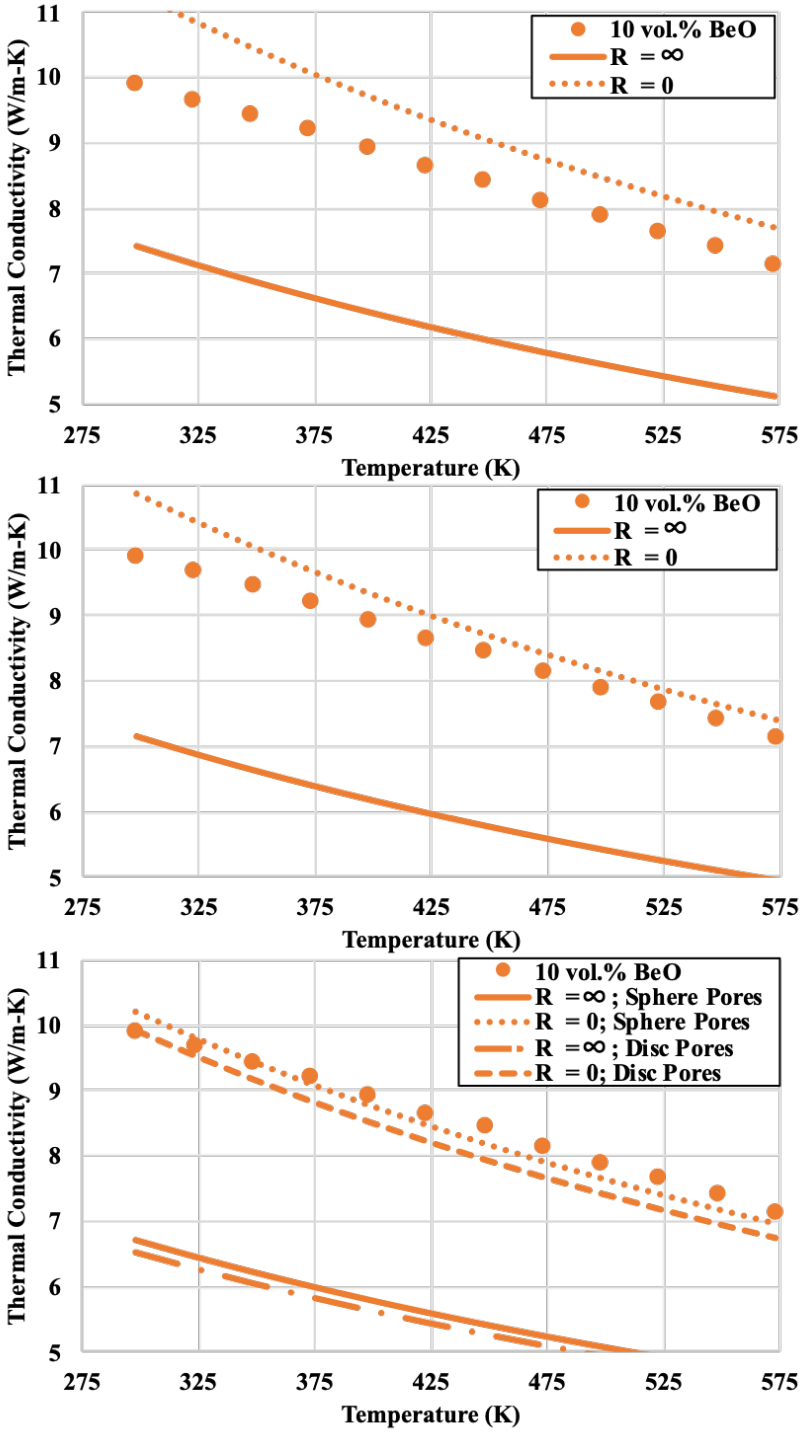

Figure 5.2 The experimental data for S-10 compared to analytical predictions with an interfacial thermal resistance, R, for a fully dense model (top), a model including the closed porosity (middle), and a model including the open porosity (bottom) with two pore geometries

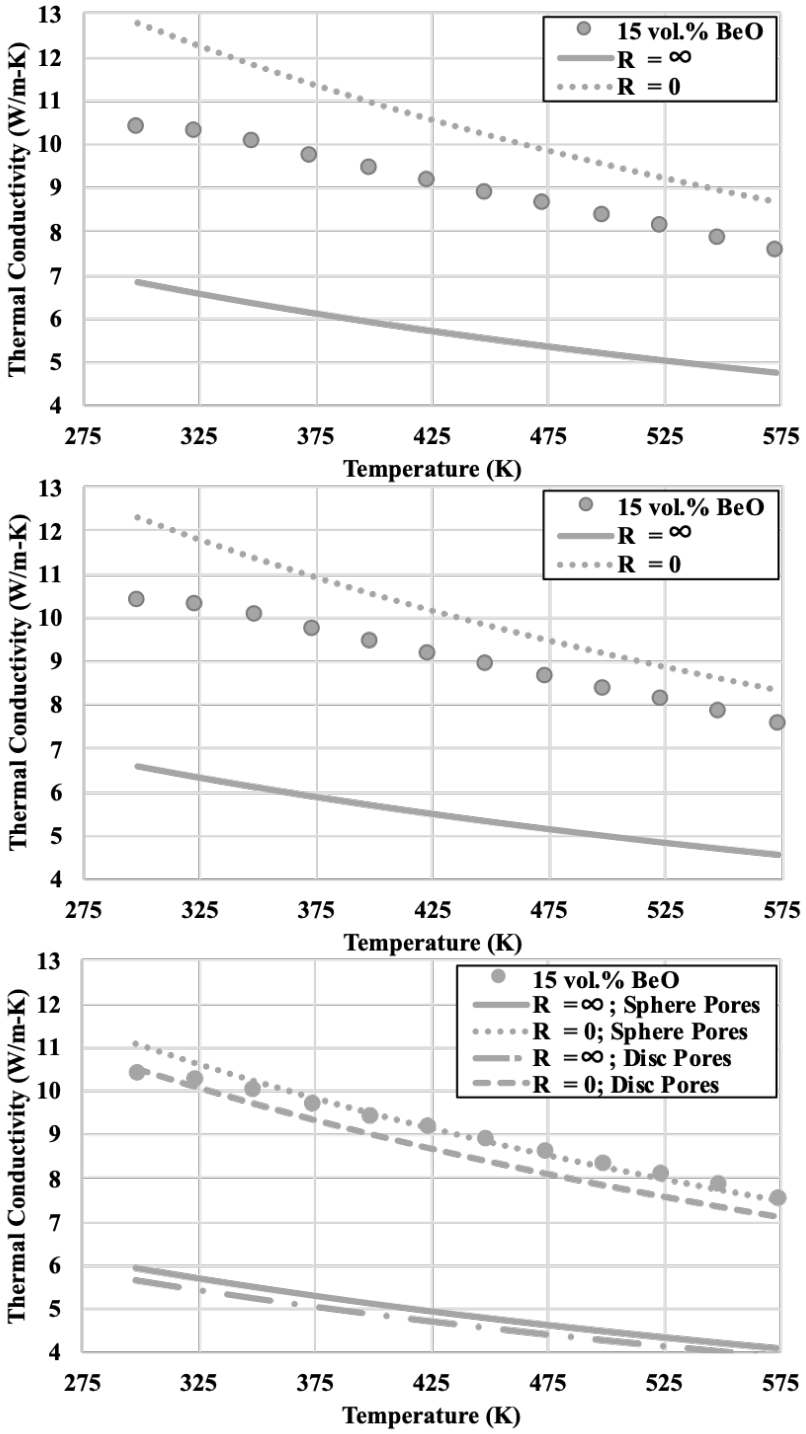

Figure 5.3 The experimental data for S-15 compared to analytical predictions with an interfacial thermal resistance, R, for a fully dense model (top), a model including the closed porosity (middle), and a model including the open porosity (bottom) with two pore geometries

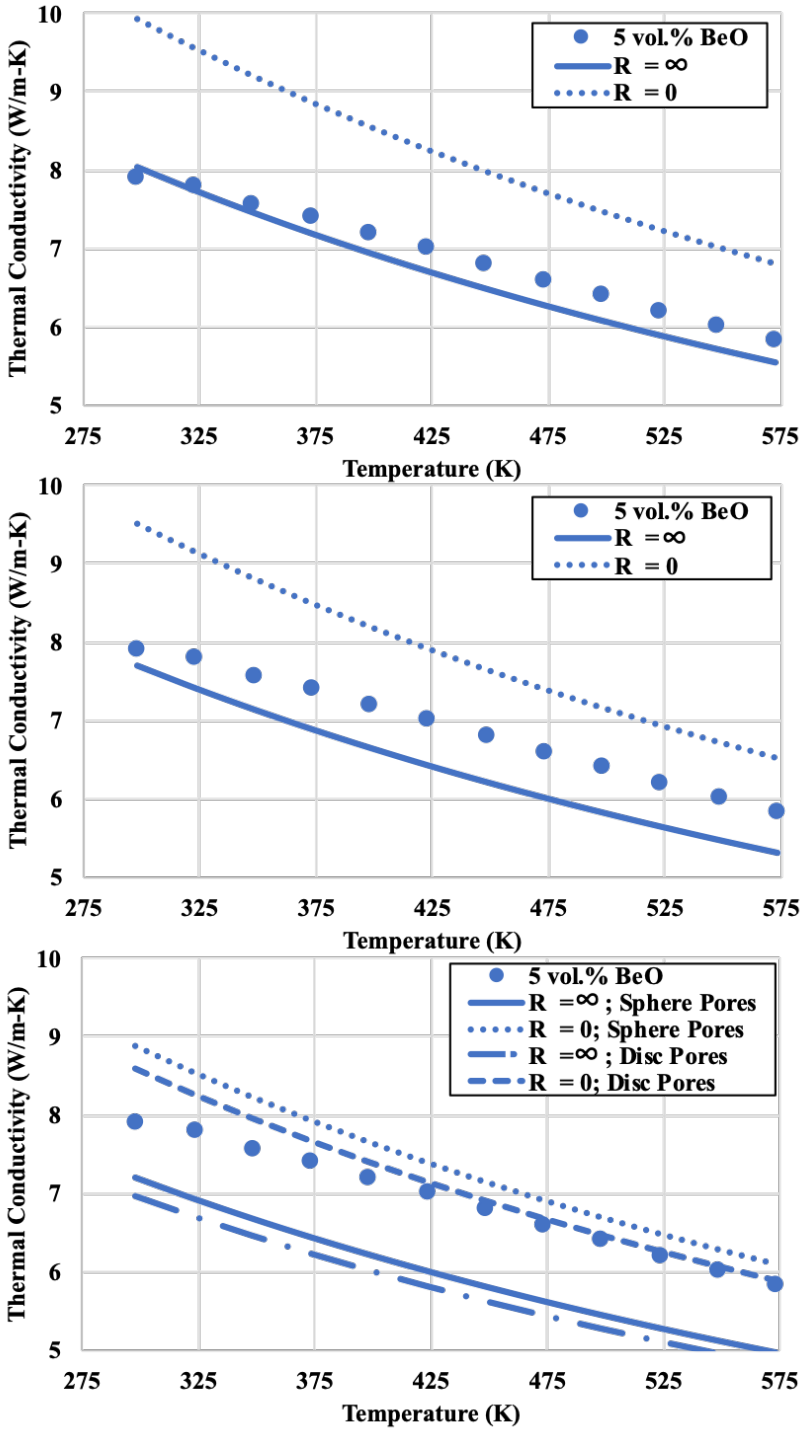

Figure 5.4 The experimental data for L-5 compared to analytical predictions with an interfacial thermal resistance, R, for a fully dense model (top), a model including the closed porosity (middle), and a model including the open porosity (bottom) with two pore geometries

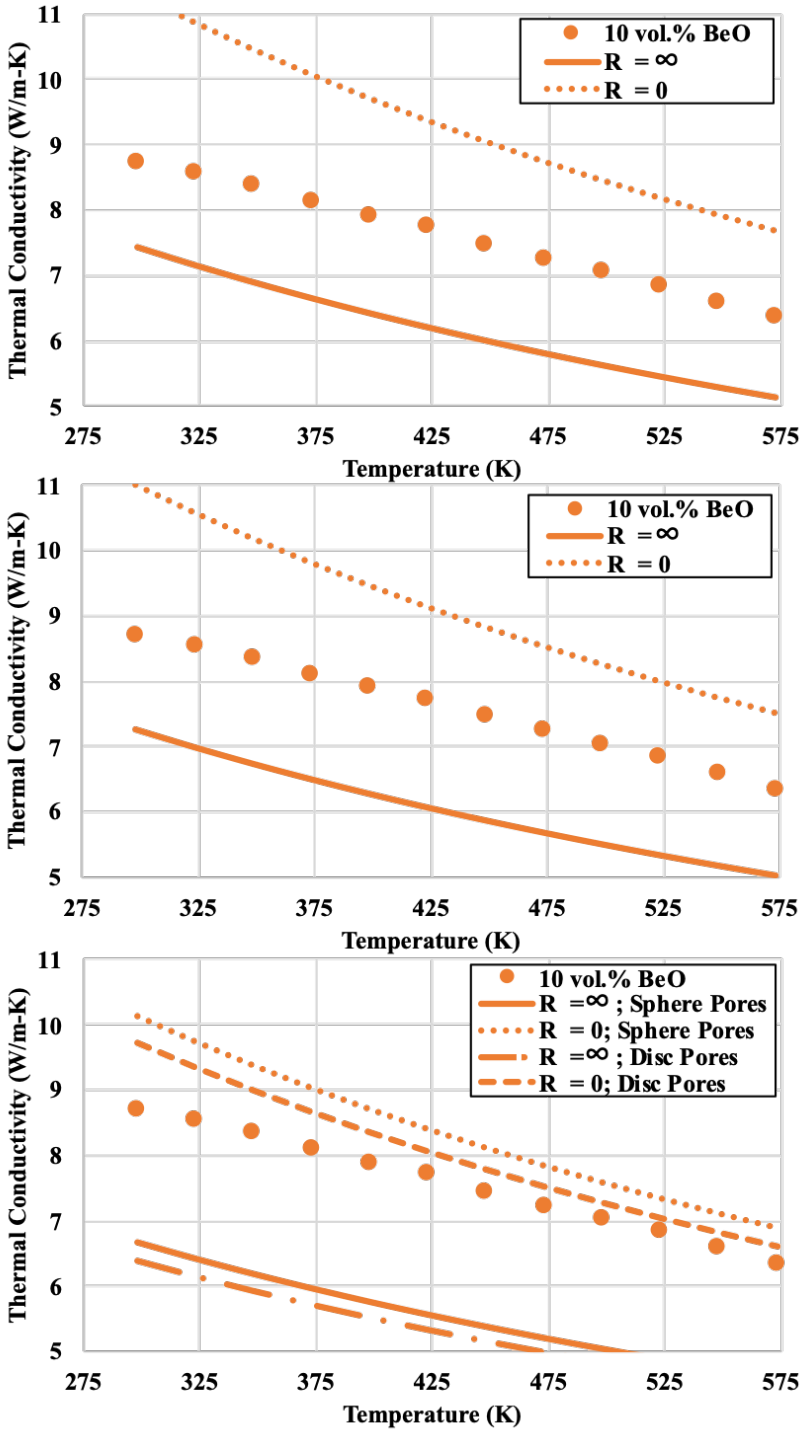

Figure 5.5 The experimental data for L-10 compared to analytical predictions with an interfacial thermal resistance, R, for a fully dense model (top), a model including the closed porosity (middle), and a model including the open porosity (bottom) with two pore geometries

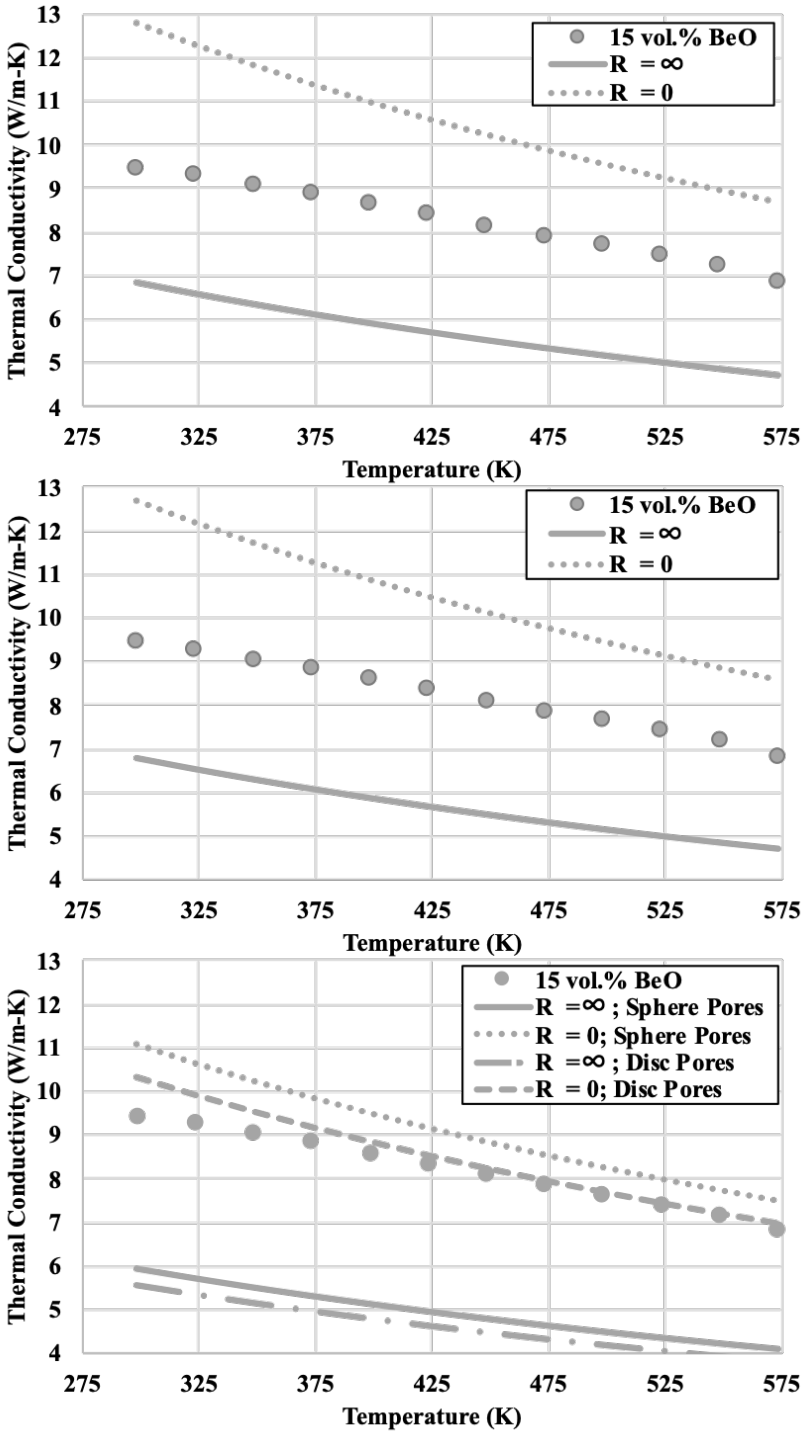

Figure 5.6 The experimental data for L-15 compared to analytical predictions with an interfacial thermal resistance, R, for a fully dense model (top), a model including the closed porosity (middle), and a model including the open porosity (bottom) with two pore geometries

Discussing the S-series in Fig. 5.1-5.3, the analytical predictions exhibit good agreement with the experimental results of S-5, in Fig. 5.1, both without and with correction for the closed porosity, within experimental error. When the open porosity is accounted for, the experimental results exceed the analytical predictions, suggesting the open porosity does not contribute significantly to the bulk thermal conductivity. In Fig. 5.2 and Fig. 5.3, the experimental thermal conductivities trend lower with increasing concentration. By S-15, the fully dense prediction is greater than the experimental data by a margin larger than the experimental error; however, the for all of the S-series a selection of the experimental data is always greater than the open porosity corrected prediction.

Considering the broad assumptions underlying this analysis, the qualitative results should only be interpreted as a guide to understand the influence of porosity in the S-series. The results of Fig. 5.1-5.3 suggest correcting the thermal conductivity in the S-series for the open porosity, as measured in Table 3, would over compensate, especially at the lower concentrations. The apparent downward drift of the thermal conductivity with increasing BeO concentration as compared to the analytical prediction can also be understood as an effect of the interfacial thermal resistance. Figure 5.7 plots Eq. 29 with no interfacial thermal resistance and with a constant interfacial thermal resistance on the order of 10^{-6} showing that with increasing filler volume fraction the improvement gap widens, similar to the results in Fig. 5.1-5.3.

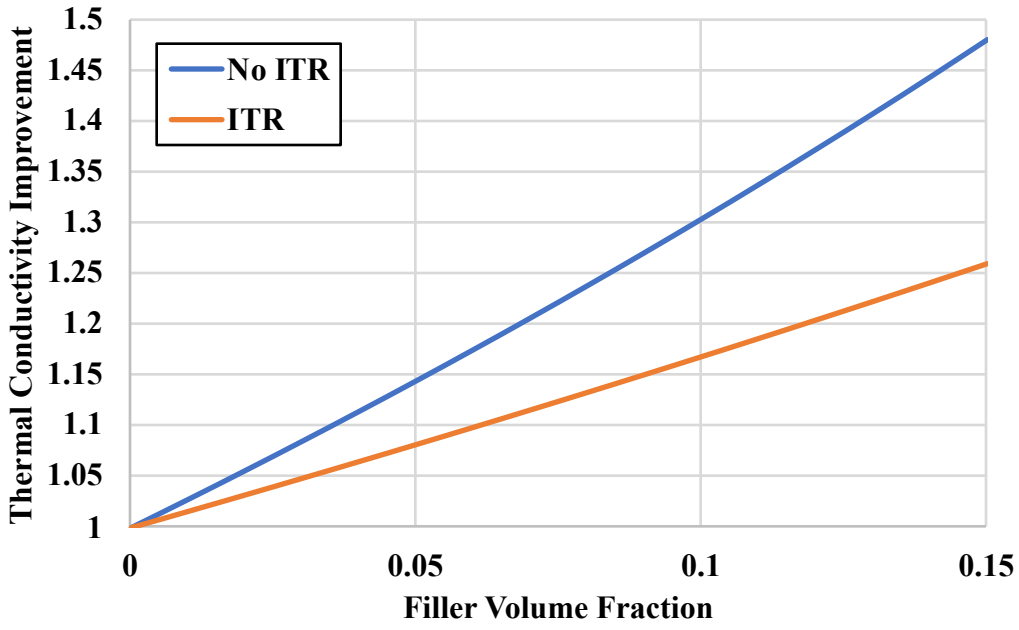

Figure 5.7 The predicted thermal conductivity improvement over UO_2 with BeO granules of increasing filler volume fraction without an interfacial thermal resistance (ITR) and with an interfacial thermal resistance on the order of 10^{-6} demonstrating the increasing difference in prediction with increasing filler volume fraction

Next discussing the L-series results in Fig. 5.4-5.6, it is notable that the thermal conductivity for sample L-5 is lower than that reported by Fink for pure UO_2, suggesting either the interfacial thermal resistance is large or that an open network of disc-shaped pores heavily influence the composite thermal conductivity. If the interfacial thermal resistance was responsible for the behavior in L-5, the thermal conductivities of L-10 and L-15 should continue to decrease, not seen in Fig. 5.4-5.6; however, L-10 and L-15 do align with the analytical predictions for an open network of disc-shaped pores, similar to L-5. Thus, it is expected that the difference between the L-series and S-series shown in Fig. 4.1 is the result of an open porosity network present in the L-series but not as influential in the S-series. This conclusion is consistent with the trends seen in Table 3

where the L-series had higher open porosity, while the S-series had higher closed porosity, although the BeO concentration appears to have a larger impact.

The open porosity network suspected to be present in the L-series can be understood by two complementary factors, sintering defects related to granule size and the thermal diffusivity measurement geometry. It has been reported in the literature that the granule size is directly related to the depth of penetration of surface defects such as stacking faults during compaction which cannot resolve during sintering [117-118]. Interconnected defects concentrated near the sample surface could contribute significantly to the measured open porosity with the penetration depth dependent on the sample series. While the LFA samples were sectioned from the center of a larger sample, open porosity originating from the outer radius would remain.

Related to the compaction defects, the LFA sample holder assembly measures the thermal diffusivity of only the center of 9.8 mm diameter, shown visually in Fig. 5.8. With sample diameters from 12.73 to 13.14 mm, a ring of approximately 1.5 mm thickness along the outer sample rim contributes to the reported density but is not sampled by the LFA. If the open porosity terminates within the unsampled ring, as Fig. 5.1-5.3 suggests is the case with the S-series, the open porosity does not contribute to the reported thermal conductivity; however, if the open porosity terminates in the region sampled by LFA, it does influence the reported thermal conductivity, as evident in Fig. 5.4-5.6 for the L-series where the open porosity is expected to penetrate deeper due to the larger granules.

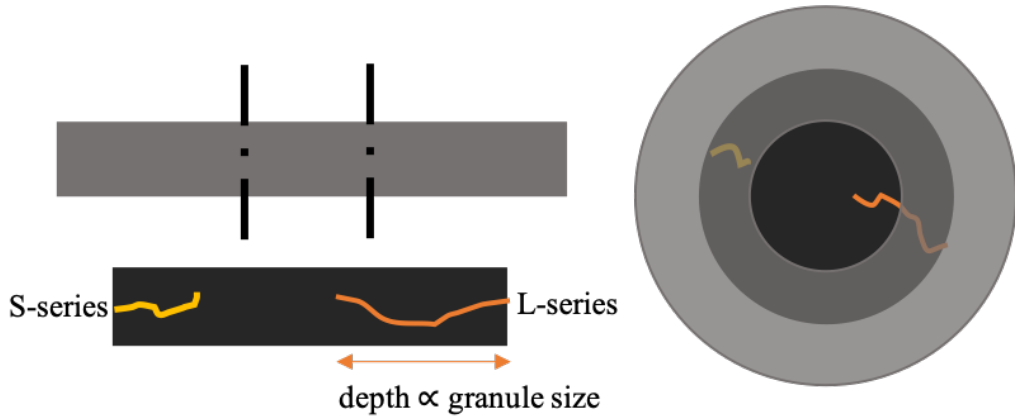

Figure 5.8 Demonstrative diagram of the combined effects of compaction defects differing between the S-series and L-series and the measurement of the thermal diffusivity by LFA shown in cross-section (left) and from the viewpoint of the LFA detector (right)

For the S-series, the data supports the use of the solid density measured by pycnometer to calculate the thermal conductivity from the thermal diffusivity and specific heat. To correct the calculated thermal conductivities to a uniform density for comparison, the Brandt-Neuer expression given by Eq. 24 is used to correct to 95%TD, aligned with convention and shown in Fig. 3.5 and Fig. 3.6. For the L-series, however, the influence of the open porosity on the thermal conductivity is difficult to assess. With measurement accuracy critical to the innovation of this work, additional analysis and discussion regarding the L-series of samples is not completed, as preluded in the results section. By addressing the steps taken to evaluate and standardize the sample porosity across the samples produced, the results reported for the thermal conductivity of the composite S-series samples can be viewed positively in the role as a basis to fit the component and interface properties by the inverse problem and flash method.

5.2. Stereological Inversion of the BeO Granule Size Distribution

The calculation of the interfacial thermal resistance lastly requires the granule radius in Eq. 29. The stereological inversion technique implemented in MATLAB by [115] and developed by others [35-39,109-114] transforms the observed, two-dimensional apparent diameter distribution to the three-dimensional true diameter distribution; however, prior studies have noted the balance between sample size and histogram bin selection and the resulting true distributions [119]. The following discussion considers this balance in the consideration of the full data set to represent the individual sample distributions to expand the sample size and a nonparametric fit to the data to smooth statistical fluctuations and reduce the histogram bin width.

The apparent diameter distribution for each sample in Fig. 4.11 show good qualitative agreement with one another and with the expectations based on the fabrication method. The distributions can be understood as a superposition of two distributions, the sieved primary granules, demonstrating agglomeration at increasing concentrations, and smaller secondary granules originating from the primary, forming during processing. While the secondary particles are large in number, they contribute very little to the volume, as shown in Fig. 4.18 and thus to the thermal conductivity. The average diameter of the distributions is reported as a volume weighted average to reflect this. Unlike the summary statistics reported in Table 6, the average granule diameter for the data following stereological inversion in Table 7 increases with increasing concentration. The average between the distributions varies by approximately 10% likely due to the increasing agglomeration of multiple granules.

A sample cross-section of higher granule concentration, however, also directly features a higher sample size. It is possible the full extent of agglomeration was not observed in the sample S-5. Even with a coarse histogram binning, the inversion procedure for S-5 indicates the sample size is too small, completely consuming the data in the third bin, shown in Fig. 4.13. Similarly, the next to last histogram bin of the true diameter distribution of sample S-10 in Fig. 4.14 is depleted.

To increase the apparent diameter sample size and supported by the granules resulting from the same production method, it is proposed to report a single diameter value representative of all the samples. The all-inclusive apparent diameter distribution is shown in Fig. 4.12 and demonstrates a reasonably smooth description of the granule distribution; however, as shown in Fig. 4.16, even with a larger sample, small statistical fluctuations are amplified during the transformation. Consequently, a fit to the original empirical cumulative distribution functions in Fig. 4.10 is considered.

While several forms of distribution were considered, including traditional powder size distributions such as lognormal and Weibull, only the nonparametric kernel distribution could be fit to all of the data sets and result in the Kolmogorov-Smirnov test failing to reject the null hypothesis at the default 5% significance level. The kernel distribution was fit to the cumulative distribution of the apparent area data directly and transformed to the diameter data plotted in Fig. 5.9 and in later analysis, circumventing issues associated with the bin width of a fit empirical probability density function. The results for each sample are shown in Fig. 5.9. The fit kernel distribution is compared to

the data presented in a histogram in Fig. 5.10 with the same number of bins as suggested by Scott's normal reference rule.

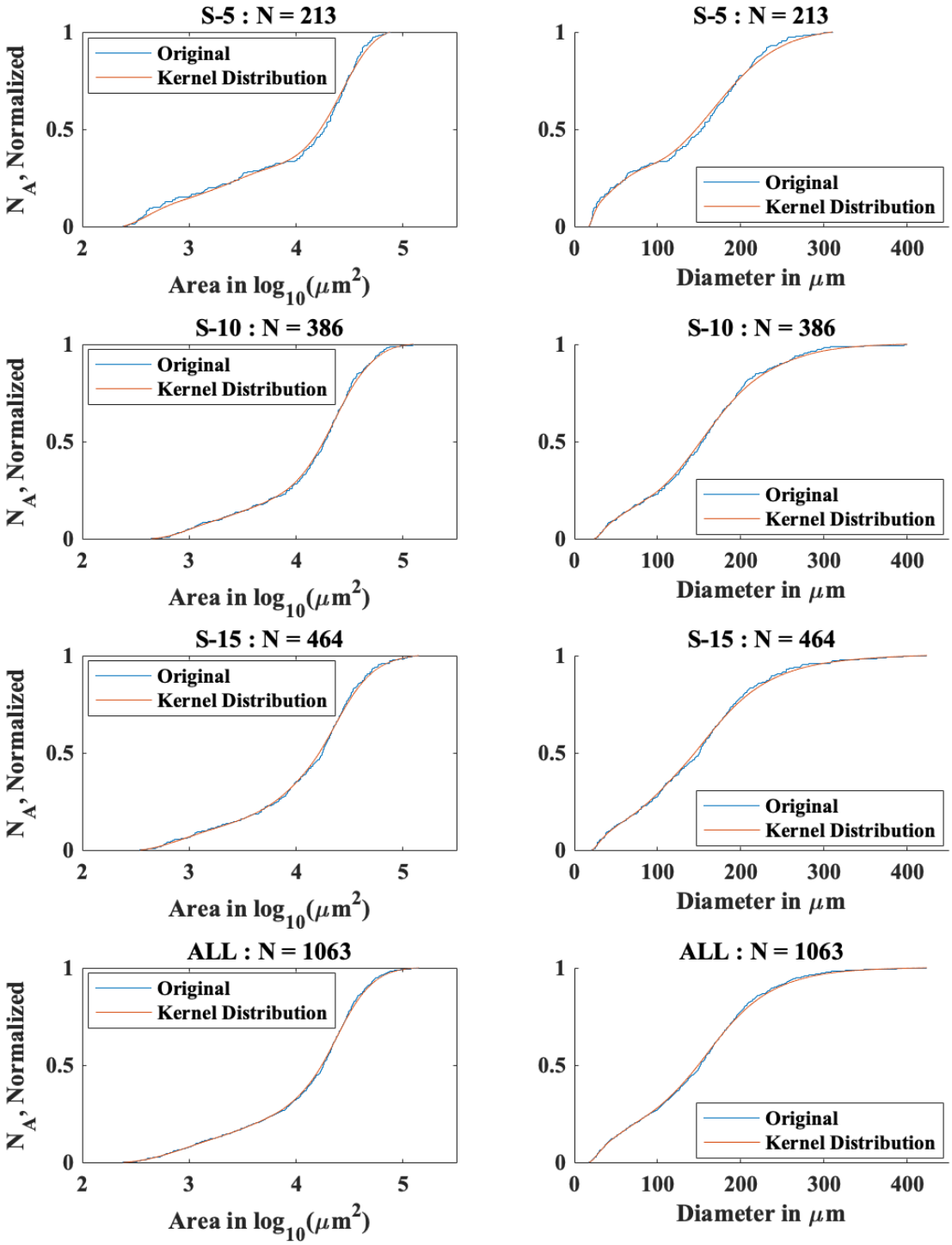

Figure 5.9 The empirical cumulative distribution functions for the BeO granule size for the S-5, S-10, and S-15 samples and the entire data set with the kernel smoothing function used to represent the data during stereological inversion plotted against the measured area (left) and the equivalent diameter (right) normalized to unity

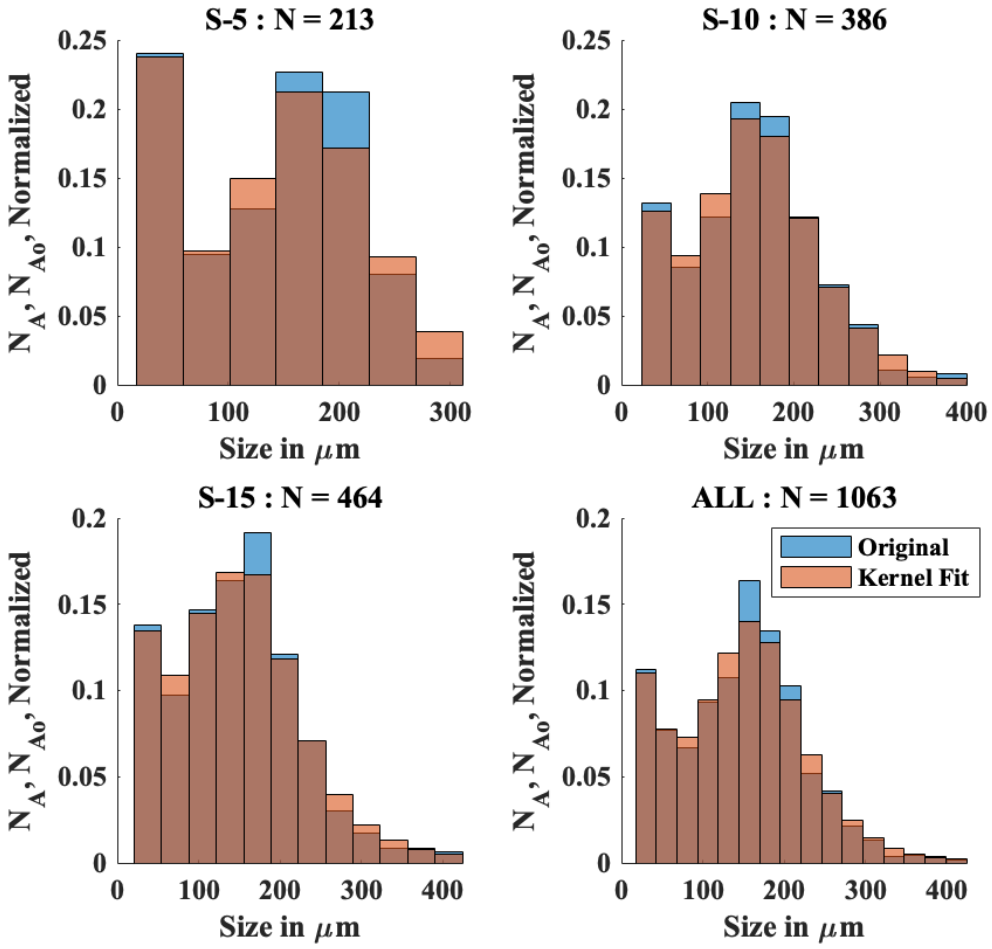

Figure 5.10 The per sample and all-inclusive cumulative distribution function of the granule diameter binned according to Scott's normal reference rule compared to the result of the smoothed kernel distribution binned similarly

The analysis reported in Chapter 4 is repeated with the smoothed kernel distribution fit. Similarly reported in the literature, the smoothed fit supports a finer histogram binning scheme—double the number of histogram bins are presented. Figure 5.11 and Fig. 5.12 show the result of the finer histogram bin width and the smoothed kernel distribution on the apparent diameter distributions. The true diameter distributions,

weighted by number and volume, revealed by stereological inversion for each sample and the all-inclusive data set are shown in Fig. 5.13-5.16. Figure 5.17 and 5.18 directly compare the results for each sample.

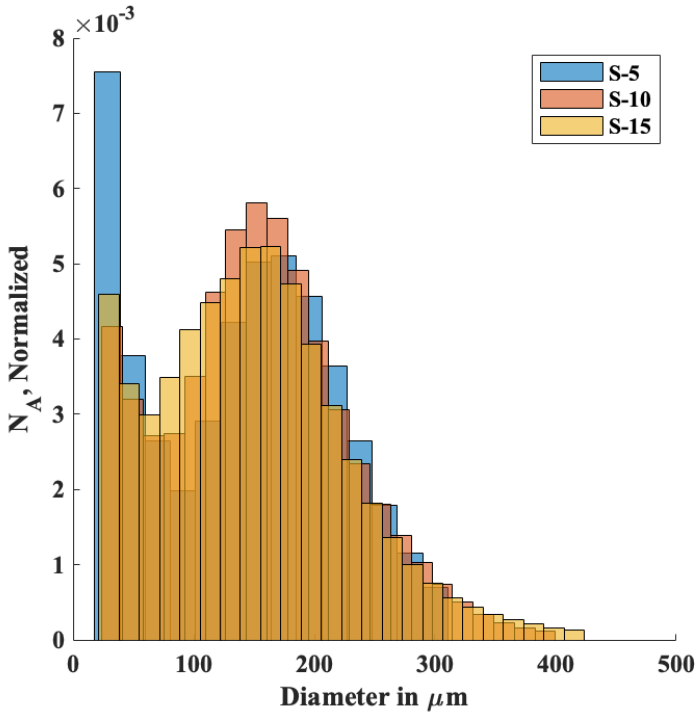

Figure 5.11 The smoothed kernel distribution for each sample binned into twice the number of bins suggested by Scott's normal reference rule and normalized to compare the distribution of equivalent diameters observed

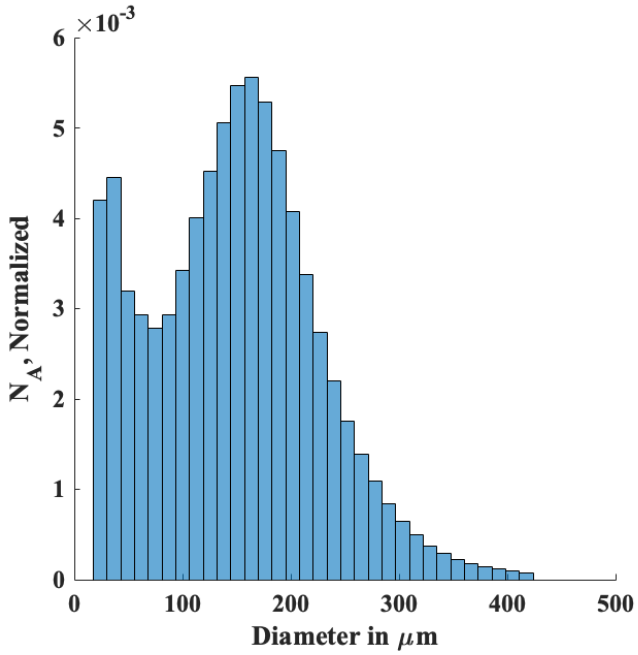

Figure 5.12 The smoothed kernel distribution for the all-inclusive data binned into twice the number of bins suggested by Scott's normal reference rule and normalized to represent the diameter distribution in each sample

As is expected based on Fig. 5.10, Fig. 5.11 and 5.12 show similar features to Fig. 4.11 and Fig. 4.12 with respect to the apparent diameter distributions' relative bin frequencies, skew, and modes. Notably, the histograms demonstrate both less statistical fluctuations and a finer bin width not achievable from the raw data, although the outcome is to be expected from a smoother kernel distribution fit. While not apparent with arithmetic binning for the individual samples, the histogram of the all-inclusive kernel distribution begins to indicate the presence of the predicted secondary particle distribution in Fig. 5.12.

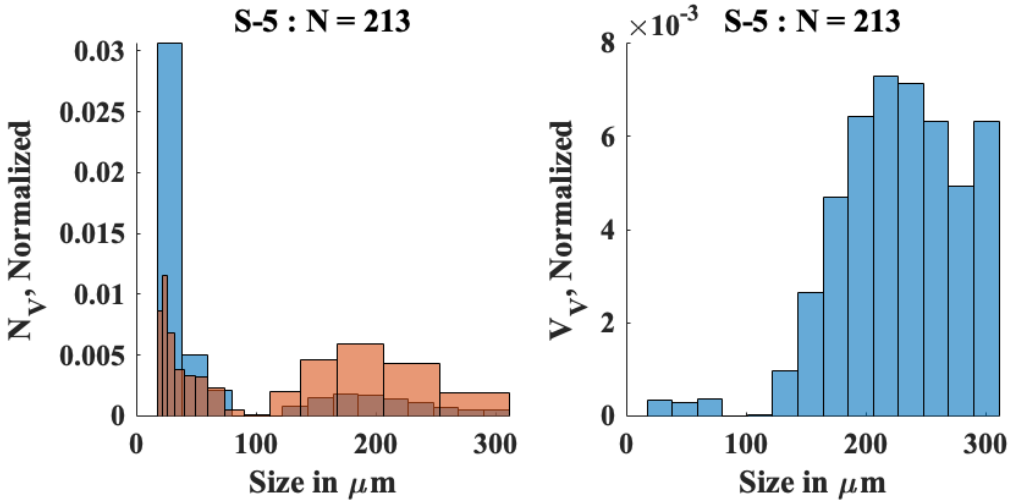

Figure 5.13 The true diameter distribution for S-5 recovered from the smoothed kernel apparent diameter distribution by stereological inversion displayed with each granule weighted equally (left) with equally spaced arithmetic binning, and geometric binning for resolution at lower diameters, and with granule frequency weighted by volume (right)

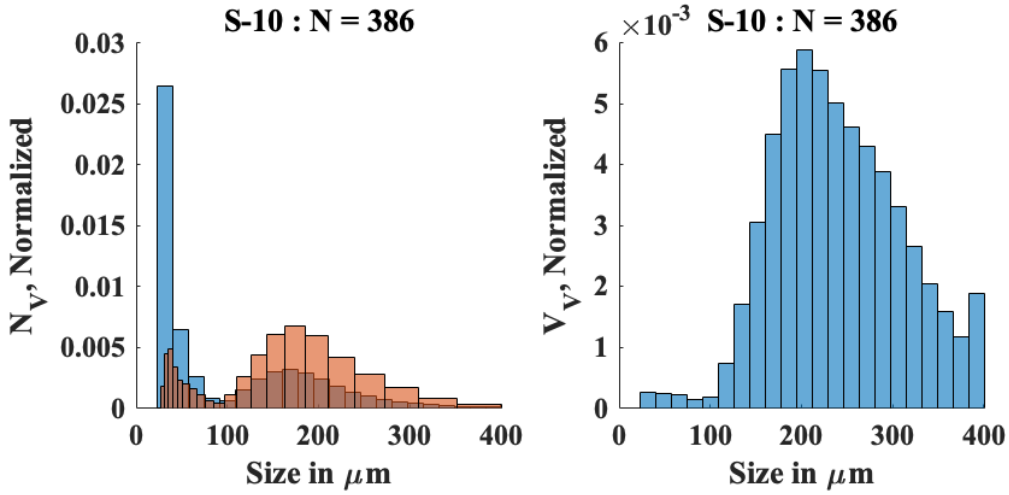

Figure 5.14 The true diameter distribution for S-10 recovered from the smoothed kernel apparent diameter distribution by stereological inversion displayed with each granule weighted equally (left) with equally spaced arithmetic binning, and geometric binning for resolution at lower diameters, and with granule frequency weighted by volume (right)

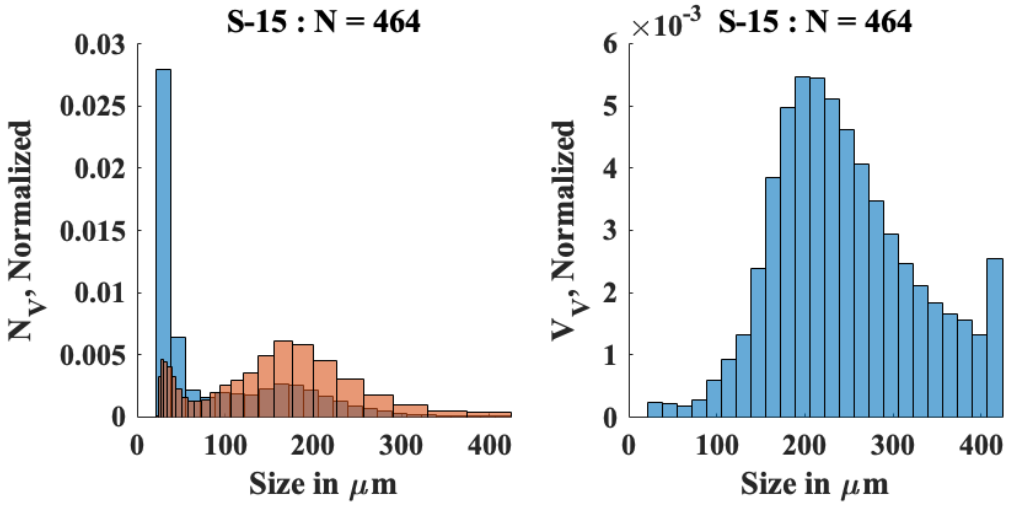

Figure 5.15 The true diameter distribution for S-15 recovered from the smoothed kernel apparent diameter distribution by stereological inversion displayed with each granule weighted equally (left) with equally spaced arithmetic binning, and geometric binning for resolution at lower diameters, and with granule frequency weighted by volume (right)

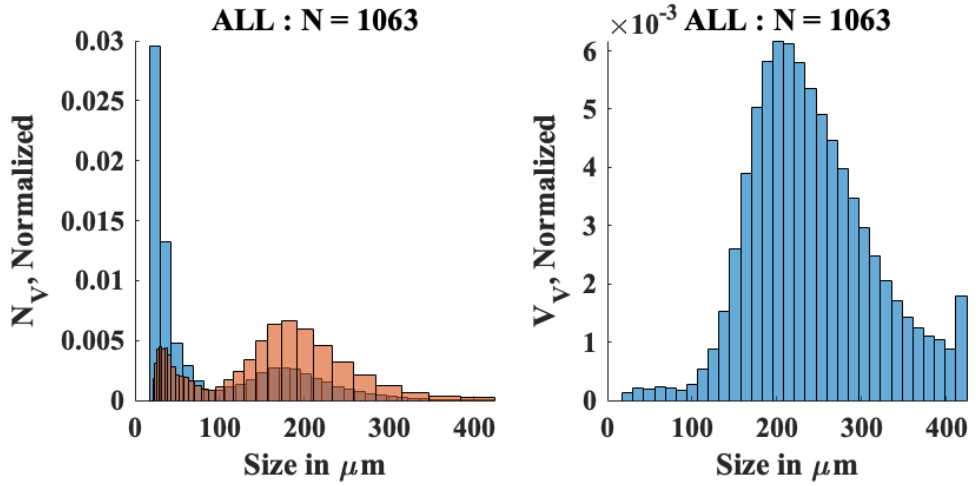

Figure 5.16 The true diameter distribution recovered from the smoothed kernel apparent diameter distribution for the all-inclusive data set by stereological inversion displayed with each granule weighted equally (left) with equally spaced arithmetic binning, and geometric binning for resolution at lower diameters, and with granule frequency weighted by volume (right)

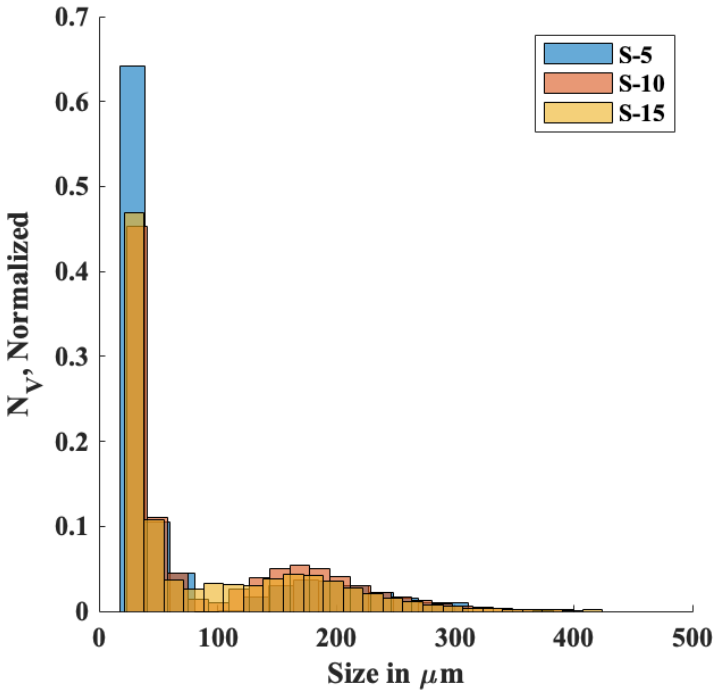

Figure 5.17 A comparison of the number-weighted true diameter frequency of each of the UO_2-BeO samples fabricated and fit by a smoothed kernel distribution

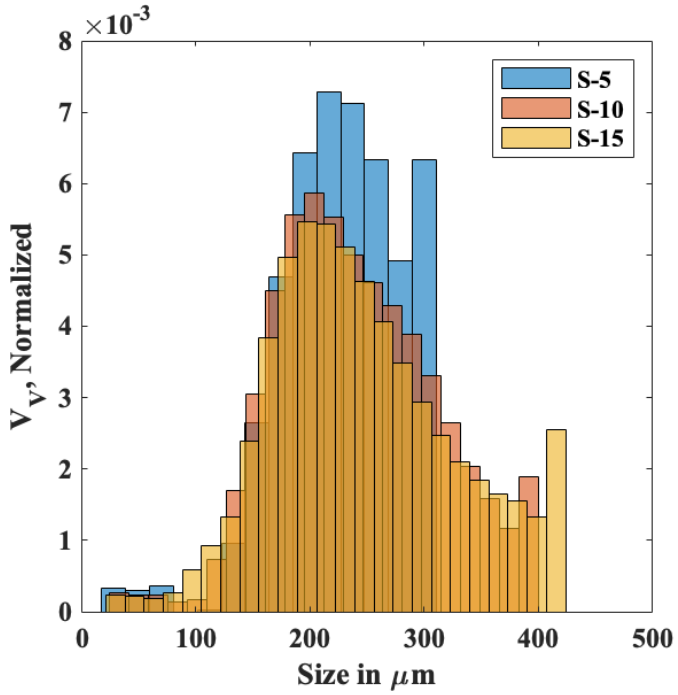

Figure 5.18 A comparison of the volume-weighted true diameter frequency of each of the UO_2-BeO samples fabricated and fit by a smoothed kernel distribution

Compared to the raw data inversion, the stereological inversion of the smoothed kernel fit to the individual sample apparent diameter data and the all-inclusive apparent diameter data demonstrates a smoother and more parametric form around the expected size range of 150 to 250 μm in the true diameter distribution. The number-weighted distributions in Fig. 5.13-5.16 tend to be more developed, showing the features of the secondary distributions of granules in the geometric binning scheme; however, S-5 still features zero frequency bins. The volume-weighted distributions smoothly transition across the bins except for the final bin which is distinctly increased in all the distributions. The feature was also evident in the volume-weighted true diameter distributions based on the raw data in all but the S-5 distribution in Fig. 4.13-4.16. It is expected to be evidence of the agglomeration of granules exaggerated by the volume-weighted transformation of the histogram.

The qualitative features of the true diameter distributions derived from the smoothed kernel fits shown in Fig. 5.13-5.16 are very similar to one another and the raw data true diameter distributions in Fig. 4.13-4.16; however, the true diameter distributions derived from the smoothed kernel fits gain a higher resolution view of the granule size distribution. While the smoothed kernel fit did not eliminate the zero frequency bins in the S-5 series results, indicative of a low sample size, the individual sample distributions are well represented by the all-inclusive data results.

The summary statistics for the distributions and the all-inclusive distribution are presented in Table 11. Shortcomings of the raw data results presented in Chapter 4, including small sample sizes and statistical fluctuations exaggerated by histogram binning

and stereological inversion, improved by fitting a smoothing kernel distribution to an all-inclusive data set representing all of the samples. To calculate the interfacial thermal resistance, a 242.2 μm granule diameter will be implemented in Eq. 29 to represent the true diameter distribution in the S-series of samples.

Table 11 The summary statistics for the true BeO granule size for the S-5, S-10, and S-15 samples and the all-inclusive data set following a fit of a smoothed kernel distribution and stereological inversion

	S-5	**S-10**	**S-15**	**ALL**
Mean (μm)	228.7	241.1	247.2	242.2
Mode (μm)	216.5	203.5	197.4	201.8

5.3. Calculation and Implementation of the Interfacial Boundary Resistance

Using the composite thermal conductivity data for S-5, S-10, and S-15 in Fig. 4.4 and Table 5 and the granule filler diameter "unfolded" from a smoothed kernel fit to the all-inclusive empirical cumulative distribution function for the area data set in Table 11, a series of three equations from Eq. 29 and three unknowns, the matrix and particle thermal conductivities and the interfacial thermal resistance, can be fit. At each temperature measured, the nonlinear least squares solver was seeded with the thermal conductivity of S-0 for the matrix thermal conductivity, the thermal conductivity of BeO from Eq. 23 for the particle thermal conductivity, and 5×10^{-9} for the interfacial thermal resistance. The solution was constrained to positive values less than 1.5 of the thermal conductivity of each component and 1×10^{-4} for the interfacial thermal resistance. The data and the fit solution for each temperature are shown in Fig. 5.19. The values for the matrix and particle

thermal conductivity and interfacial thermal resistance to construct the fit solutions are given in Table 12.

Adopting the approach used by Nan, Li, and Birringer to scope the uncertainty in the measurements described in Chapter 3, the interfacial thermal resistance is expected to have a ±14% uncertainty composed of ±6% uncertainty resulting from the uncertainty in the composite thermal conductivity, ±4% from the granule radius, and ±4% from the granules concentration. The uncertainty in the fit beryllium oxide thermal conductivity is expected to be ±1%, resulting from small contributions from each experimental measurement. The uncertainty in the fit uranium dioxide thermal conductivity is expected to be ±5% solely from the contribution from the uncertainty in the composite thermal conductivity.

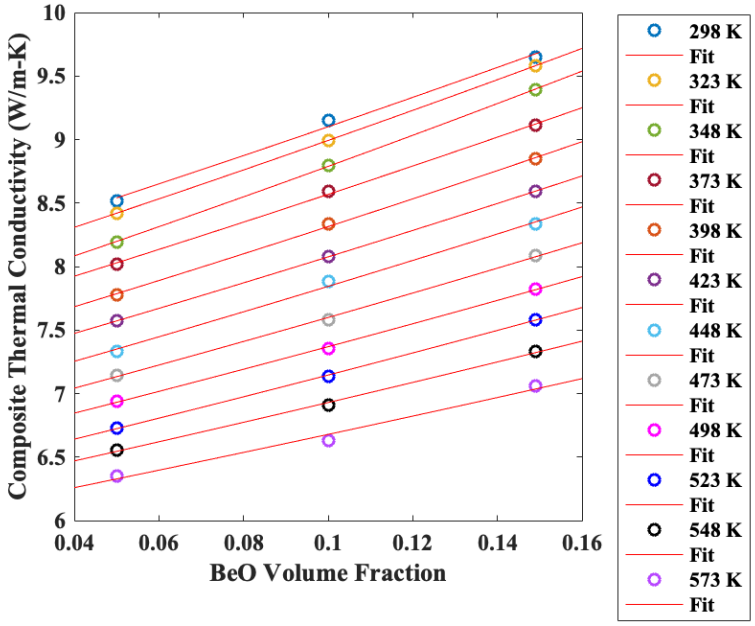

Figure 5.19 The experimental thermal conductivity of UO_2-BeO composites compared with the fit solutions to Eq. 29 solving for the in-application thermal conductivity of UO_2 and BeO and the interfacial thermal resistance

Table 12 The values for the variables in Eq. 29 solved by a nonlinear least square fit to determine the thermal conductivity of the composite components in application and the interfacial thermal resistance between them

Temperature (K)	**Interfacial Thermal Resistance (m^2-K/W)$\times 10^{-6}$**	**BeO Thermal Conductivity (W/m-K)**	**UO_2 Thermal Conductivity (W/m-K)**	**R^2**
298	4.10	272.84	8.00	0.994
323	3.93	249.52	7.87	~1
348	3.68	228.72	7.64	~1
373	4.12	207.74	7.51	0.998
398	4.15	190.70	7.28	0.999
423	4.35	175.88	7.09	~1
448	4.39	162.35	6.88	0.996
473	4.66	150.19	6.69	0.999
498	4.98	139.27	6.51	0.999
523	5.13	129.61	6.32	0.999
548	5.68	120.47	6.17	0.997
573	6.25	112.00	5.99	0.988

The solution to the inverse problem plotted in Fig. 5.19 shows good agreement with the experimental data, with the R^2 values all near unity in Table 12. The thermal conductivity of each component of the composite are also near the data from the literature. The comparison of the fit particle thermal conductivity and Eq. 23 is shown in Fig. 5.20. The comparison of the fit matrix thermal conductivity, Eq. 23, and the thermal conductivity of S-0 at three different fractions of theoretical density are shown in Fig. 5.21.

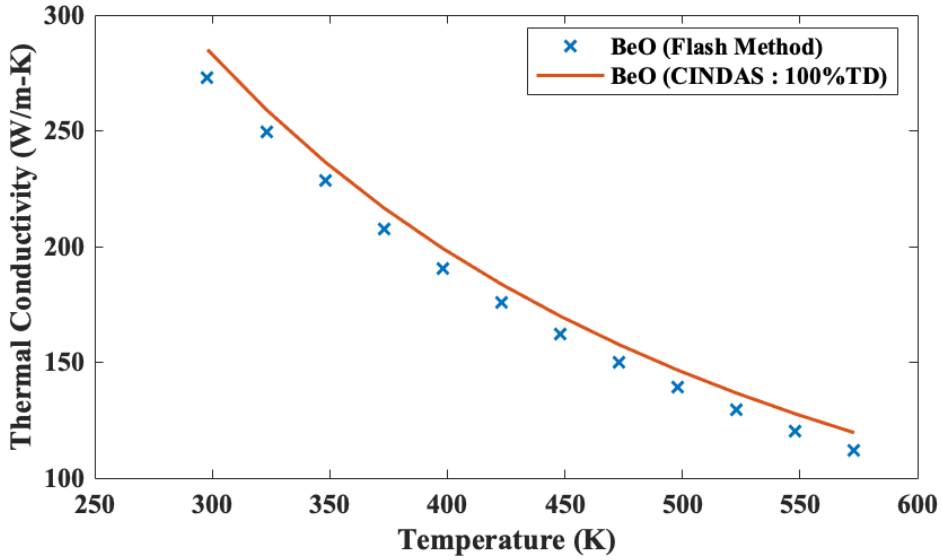

Figure 5.20 Comparison of the beryllium oxide thermal conductivity from literature to the values fit to the composite thermal conductivity data for the beryllium oxide granules in application [Adapted from 20]

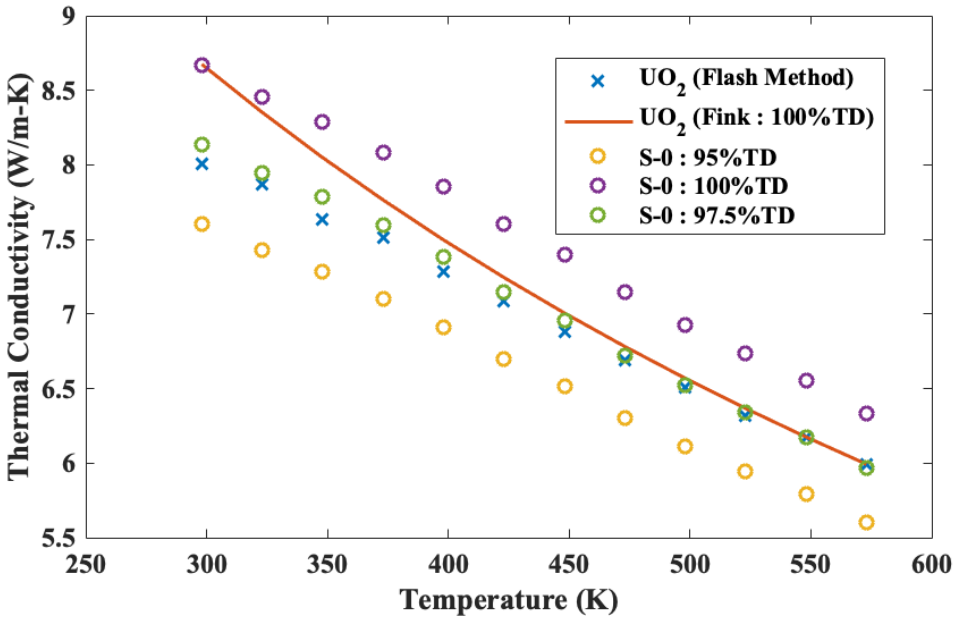

Figure 5.21 Comparison of the uranium dioxide thermal conductivity from literature to the values fit to the composite thermal conductivity data for the uranium dioxide matrix in application and the S-0 thermal conductivity reported at various fractions of theoretical density for scale [Adapted from 19]

While the literature suggests the component thermal conductivities will not necessarily equate to their bulk, polycrystalline counterparts, the results in Fig. 5.20 between the fit granule thermal conductivity and the literature thermal conductivity given by Eq. 23 show good agreement. In the literature, the particle or filler thermal conductivity can vary widely, even approaching that of a single crystal [31-32,54]. The results reported by Gao *et al.* exhibited the opposite trend revealing instead that the theoretical density of the continuous BeO network was as low as 73% in the fabricated composite [25]. If Eq. 23 is taken to represent the thermal conductivity of a fully dense granule, Eq. 25 predicts the granule is approximately 97% of theoretical density.

Whereas the uncertainty in the beryllium oxide thermal conductivity fit is expected to by ±1%, the uranium dioxide thermal conductivity fit was more sensitive to variations in the experimental data, with an expected uncertainty of ±5%. In considering the calculated thermal conductivity of the UO_2 matrix, shown in Fig. 5.21, at elevated temperatures the matrix conductivity is nearly equivalent to the fully dense expression given by Eq. 23, which is known from microscopy to not be the case. For comparison, sample S-0, a pure UO_2 sample of the same S-series, is shown for a range of porosity values corrected by Eq. 24. The plot shows that, among comparably sourced, fabricated, and analyzed experimental data, the fit matrix thermal conductivity agrees well with the expected results. If the S-0 data is taken to represent the thermal conductivity of a fully dense matrix, Eq. 24 predicts the granule is also approximately 97% of theoretical density.

While the results of the non-linear least squares fit for the component thermal conductivity align with the expected values based on the measured density and observed

micrographs, the measurement of the interfacial thermal resistance is sensitive to the matrix and granule thermal conductivity values. The interfacial thermal resistance value may value widely under an alternative approach, such as using literature correlations for the thermal conductivity of UO_2 and BeO and fitting only the interfacial thermal resistance. The 14% uncertainty in the interfacial thermal resistance measurement is intended to encompass the variation in approach, but alternative calculation methods of the interfacial thermal resistance will be of substantial interest in future work.

The discussion of the results of the solution to the inverse problem reinforces the credibility of the method, demonstrating not only R^2 values near unity, but predicting sensible thermal conductivity values for the particles and the matrix. Finally, the fit interfacial thermal resistance values are considered. Figure 5.22 shows the calculated results among the reported literature values determined by theoretical methods, such as the acoustic mismatch model by Liu and Zhou or diffuse mismatch model by Zhu *et al.*, combined simulated-experimental methods by Badry *et al.* the combined experimental-analytical methods by Gao *et al.* [25] and the results in the literature for a BeO film on Si [120], a classic resistive case of copper and diamond [54], and two cases near the reported result, Bi_2Te_3-Sb_2Te_3 [121] and a high pressure metal contact resistance [122]. In Fig. 5.23, a higher resolution comparison is considered for the combined experimental-analytical methods performed here, in Table 12, and in Gao *et al.* [25].

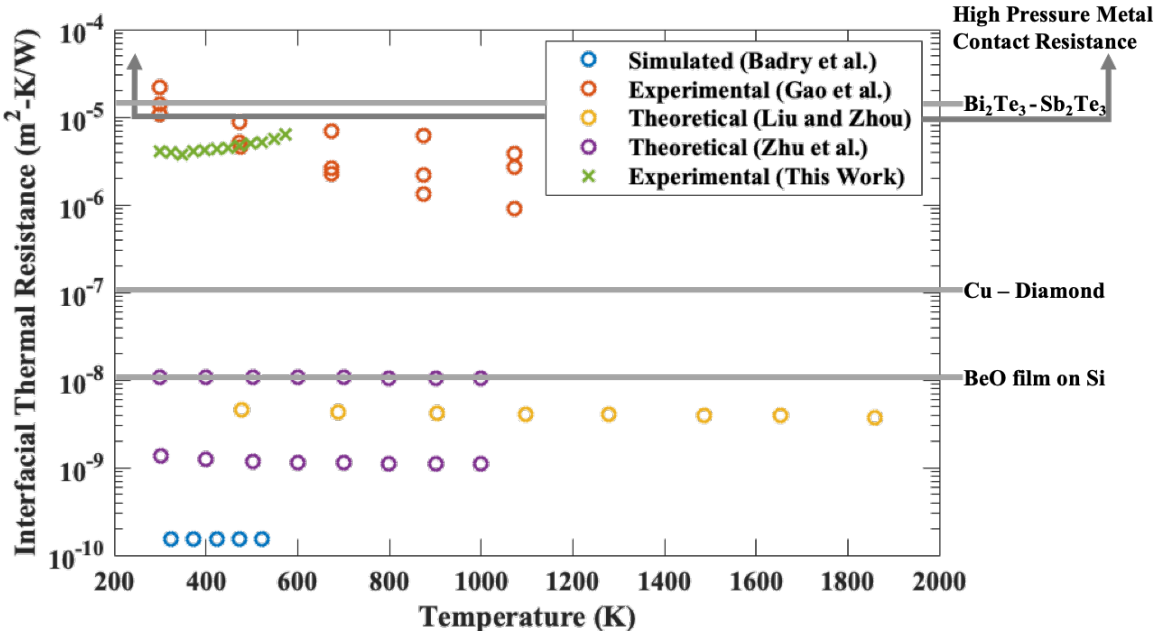

Figure 5.22 Comparison of the reported interfacial thermal resistance values between uranium dioxide and beryllium oxide determined by theoretical, combined simulated-experimental, and combined experimental-analytical methods [Adapted from 25-27,54,72,120-122]

Among the reported values in the literature in Fig. 5.22, this work compares well with the results reported by other combined experimental-analytical methods. Reports of lower interfacial thermal conductivity, on the order of 10^{-10}-10^{-9} m^2-K/W, are largely formulated by various theoretical methods, with Badry *et al*. the exception as a combined simulated-experimental measurement; however, as discussed, error is expected in the measurement reported by Badry *et al.* due to the heterogeneity of the experimental microstructure and the difference in scale of the simulation and microstructure. It is expected that a combined experimental-analytical method would result in a higher interfacial thermal resistance due to the encompassing measurement of all boundary phenomena not captured in theoretical formulations.

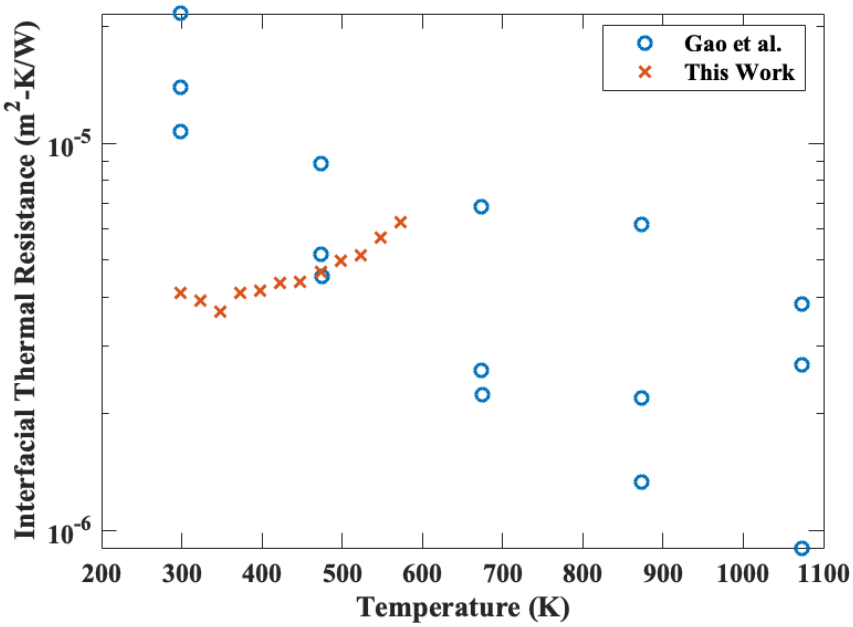

Figure 5.23 Comparison of the reported interfacial thermal resistance values between uranium dioxide and beryllium oxide determined by experimental-analytical methods on dispersed (this work) and continuous (Gao *et al.*) microstructures [Adapted from 25]

Focusing only on the interfacial thermal resistance values reported by combined experimental-analytical methods in Fig. 5.23, Gao *et al.* fabricated UO_2-BeO composites with a continuous BeO microstructure, reporting results for spark plasma sintering from Li *et al.* and two pressureless sintering methods, whereas this work fabricated dispersed BeO microstructures by pressureless sintering. The density of the BeO component in Gao *et al.* is reported in the range of 73-80% of the theoretical density, while this work predicts 97% of the theoretical density. Despite varying fabrication processes, goal microstructures, and component densities, the reported values are on the same order-of-magnitude and in agreement.

The upward trend in the data with temperature reported here is not typical, however, but could be due to the comparatively high density of measurements over a short

temperature range. In general, the interfacial thermal resistance should tend to trend down with increasing temperature. Both the thermal boundary resistance decreases until the Debye temperature after which it is constant and the thermal contact resistance decreases as the temperature approaches the fabrication temperature due to thermal expansion. Because the temperature range studied here is limited compared to the scale of the driving phenomena, the "trend" is attributed to the reported uncertainty of ±15% and a value of 4.6×10^{-6} m^2-K/W is used to represent a constant interfacial thermal resistance for the data currently available.

While only a range of values was reported, Zhu *et al.* also fit an interfacial thermal resistance on the order of 10^{-6} to 10^{-5} m^2-K/W by applying Eq. 13 to the experimental results in literature for continuous microstructures, including Ishimoto *et al.* [40]. Recalling the spread of reported improvements in Fig. 2.5, it was originally believed that the fabrication method imparted boundary conditions that contributed to higher interfacial thermal resistance, separating conventionally sintered composites from those fabricated above the eutectic temperature. The reporting by this work, Gao *et al.*, and Zhu *et al.* that the interfacial thermal boundary resistance is on the same order of magnitude regardless of fabrication technique (pressureless or spark plasma sintering), fabrication temperature (above or below the eutectic temperature), or component density (73% to 97% of theoretical BeO density), however, suggests the interfacial thermal resistance alone does not differentiate the improvements in Fig. 2.5.

While the interfacial thermal resistance is not reported as a differentiating feature between the literature, the quantification is still critical to understanding heat transfer in

the composite microstructure. Although new characterization of the microstructures reported in the literature is unlikely to impart additional understanding to Fig. 2.5, an analytical expression can be manipulated to understand how the temperature-dependent properties and microstructure influence the improvement in the thermal conductivity. By this method, the informed design of the microstructure can target improvements for applications as an accident tolerant fuel.

The results shown in Fig. 4.20, comparing Eq. 12, Eq. 13, and Eq. 37 with simulated results spanning simulation dimensions, granule shape, and interfacial thermal resistance, show the method of equivalent thermal resistance captures the effects within ~10%. Analytical expressions reported by Ishimoto *et al.* for continuous microstructures exhibited ~20% uncertainty prior to optimizing the shape factor to improve the uncertainty to ~10% [39]. Figure 4.20 shows the same uncertainty is achieved by the method of equivalent thermal resistance without optimization or characterization and incorporates the interfacial thermal resistance.

The experimental results are similarly considered for the dispersed and continuous microstructures. For the dispersed case, Eq. 13, the method of equivalent resistance, and Eq. 29, the Hasselman-Johnson expression, are compared to the experimental data using the literature correlations for the component thermal conductivity given by Eq. 23, the properties from Chapter 3, and the granule diameter from Table 11. The results are shown in Fig. 5.24. For the continuous case, Eq. 13 also uses the literature correlations and the available data in the literature. While the granule size was characterized here, comparable efforts are not reported for the continuous data in the literature. While Ishimoto *et al.*

reports grain size used as a proxy for the UO_2 granule size, Garcia *et al.* and Gao *et al.* report the sieve limits of 50-500 µm and 100-200 µm, respectively [25,34,40]. In Fig. 5.25, the assumed granule size for Garcia *et al.* is 300 µm and 200 µm for Gao *et al.*

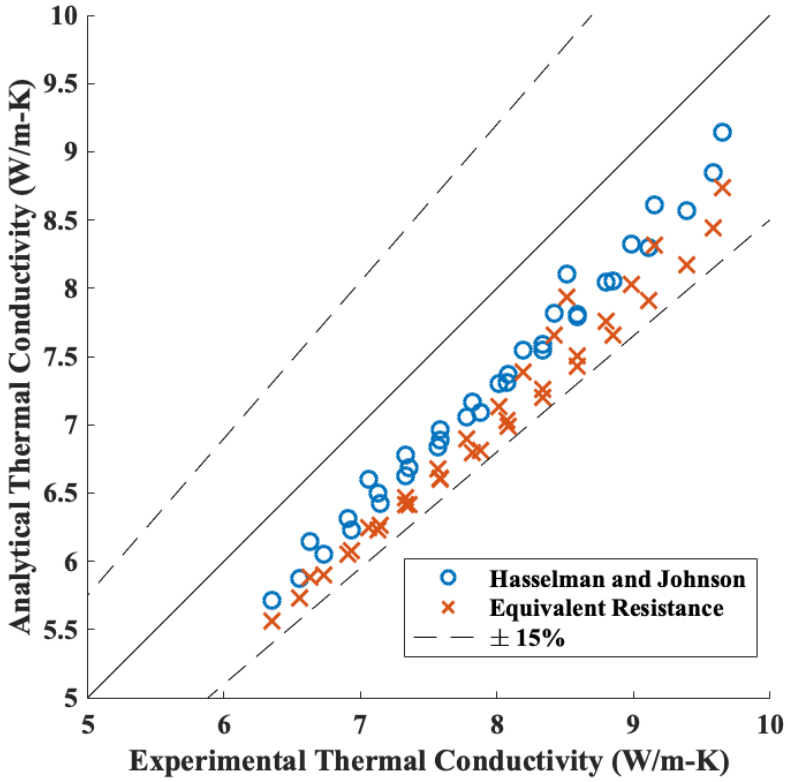

Figure 5.24 Comparison of the thermal conductivity of UO_2-BeO composites with dispersed microstructures fabricated in this work with analytical expressions reported by Hasselman and Johnson and derived by the method of equivalent thermal resistance

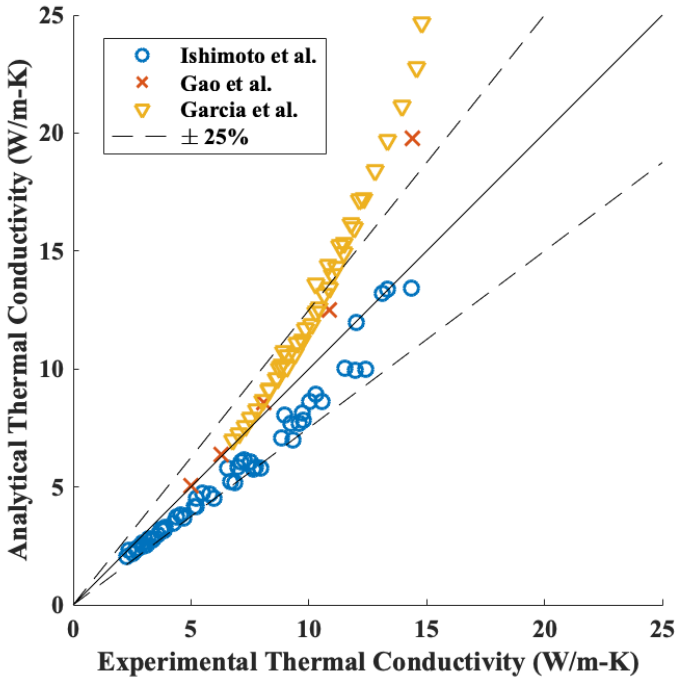

Figure 5.25 Comparison of the thermal conductivity of UO_2-BeO composites with continuous microstructures with analytical expressions derived by the method of equivalent thermal resistance [Adapted from 25,34,40]

The comparison of the analytical expressions with the experimental results for dispersed microstructures in Fig. 5.24 demonstrates the uncertainty introduced by the literature thermal conductivity correlations and bulk porosity measurements typical in the literature. The interfacial thermal resistance was, after all, fit to the Hasselman-Johnson model in the figure. Figure 5.24 demonstrates the challenge with selecting analytical expressions to model experimental microstructures, even for the well-characterized results presented in this work.

The weakness magnifies when Eq. 29 is applied to the continuous microstructures in the literature. In addition to the ±15% uncertainty associated with the literature thermal conductivity correlations and bulk porosity measurements, Fig. 5.25 relies on estimations

of the UO_2 granule size and measurement instrumentation may even influence the results. The lower temperature data, located on the higher end of the thermal conductivity, reported by Gao *et al.* and Garcia *et al.* deviates dramatically. Operating reactor fuel temperatures are expected to begin around 600 K, however, above the maximum temperature measured by LFA here, and the agreement between the analytical model and experimental results improves with temperature. Thus, the results suggest Eq. 13 is satisfactory to represent the three-dimensional, continuous, experimental microstructures at the temperatures of interest.

Figure 5.25 also revives the debate as to if the interfacial thermal resistance is as uniform across the literature as has been reported by combined analytical-experimental methods. Bruggeman's expression fit the data reported by Ishimoto *et al.* with less uncertainty without an interfacial thermal resistance. The implemented interfacial thermal resistance in Fig. 5.25 under predicts the thermal conductivity. Additionally, if the spread in the reported improvements in Fig. 2.5 is not clarified by the relationship between interfacial thermal resistance and granule size, the shape and orientation of the BeO network may dominate the improvement, an effect not captured by the analytical methods reported here and would certainly impact the evaluation of the interfacial thermal resistance in continuous microstructures as reported by Gao *et al.* and Zhu *et al.* These concerns motivated the selection of the dispersed microstructure to probe the interfacial thermal resistance in this work.

Regardless of the basis behind the varying improvements reported in the literature, with the introduction of an interfacial thermal resistance, the effective thermal

conductivity of the composite depends on the size of the components. Using Eq. 10 and Eq. 13 reported by Zhu *et al.*, the effects of the interfacial thermal resistance on the effective thermal conductivity with respect to UO_2 granule size in the continuous microstructure, temperature, and BeO concentration are explored in Fig. 5.26 and Fig. 5.27. In Fig. 5.26, the effective thermal conductivity of a UO_2-5 vol.% BeO composite with a continuous microstructure is modeled as a function of the UO_2 granule size with the interfacial thermal resistance implemented around ±15% of the value 4.6×10^{-6} m^2-K/W. The plot is produced at four temperatures, three targeting temperatures spanning the pellet radius during normal operating conditions and one approaching the eutectic temperature in an accident scenario. The sample plot is generated for a UO_2-10 vol.% BeO composite in Fig. 5.27.

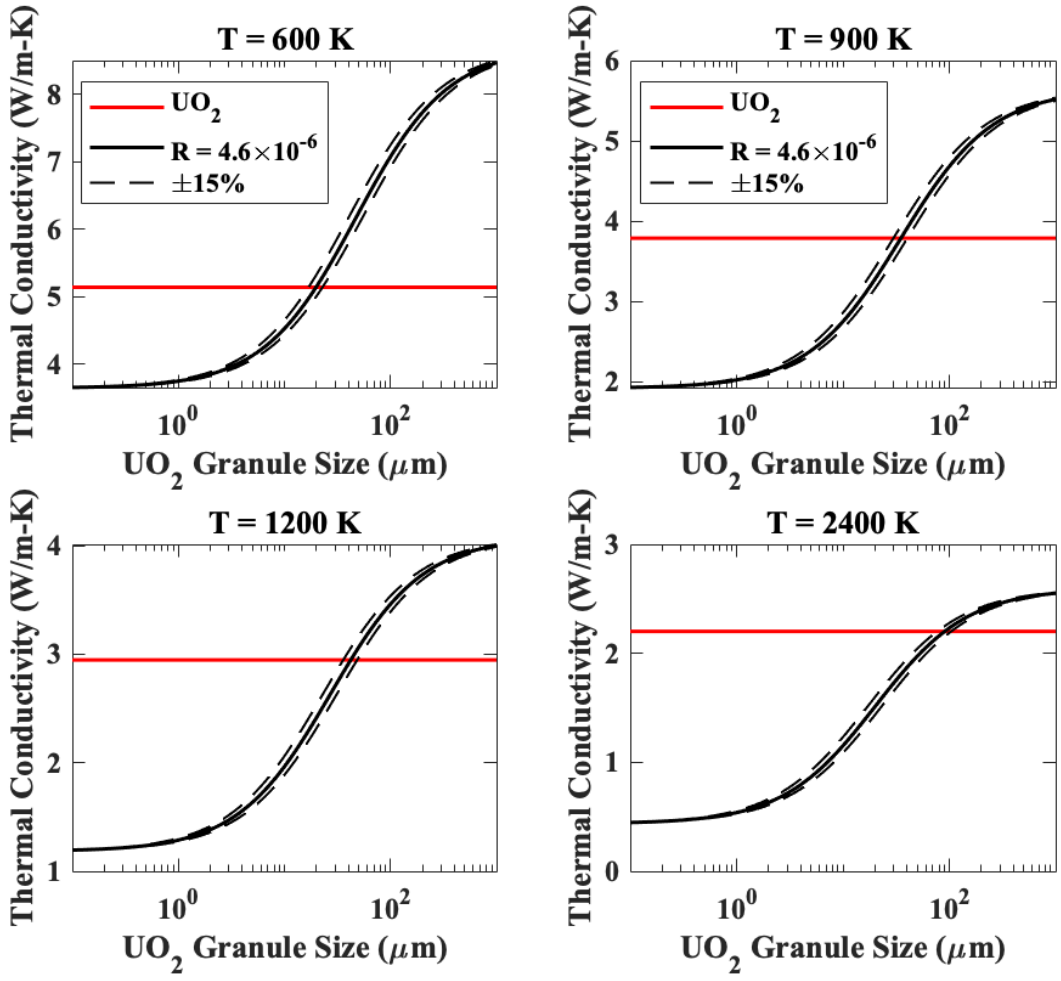

Figure 5.26 The influence of UO_2 granule size on the effective thermal conductivity of a UO_2- 5 vol.% BeO composite with a continuous microstructure modeled with an interfacial thermal resistance (m^2-K/W) at temperatures spanning normal operating conditions to a severe accident scenario

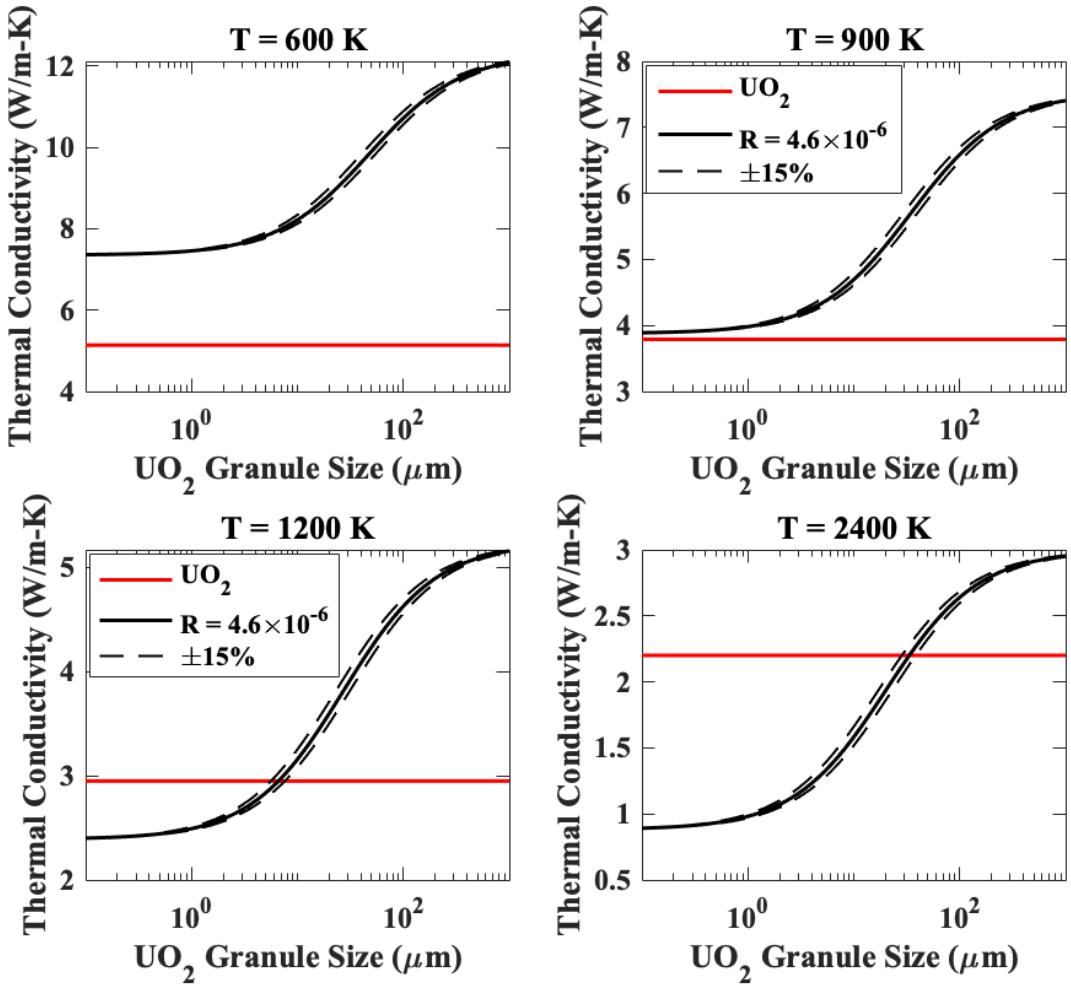

Figure 5.27 The influence of UO_2 granule size on the effective thermal conductivity of a UO_2- 10 vol.% BeO composite with a continuous microstructure modeled with an interfacial thermal resistance (m^2-K/W) at temperatures spanning normal operating conditions to a severe accident scenario

In each figure, the red line indicates the thermal conductivity of UO_2 at that temperature using the correlation reported by Fink [19]. A composite composed of granules smaller than the value at the intersection of the UO_2 and composite thermal conductivity, the critical granule size, would report a lower thermal conductivity than UO_2. In Fig. 5.26, for example, at 600 K and 900 K, a UO_2- 10 vol.% BeO composite exhibits higher thermal conductivity than UO_2 for all granule sizes; however, the granule

size becomes appreciable at 2400 K, a scenario the fuel is targeted to exhibit improved performance over UO_2. The relationship between the critical granule size and temperature for the two BeO concentrations considered here is shown in Fig. 5.28.

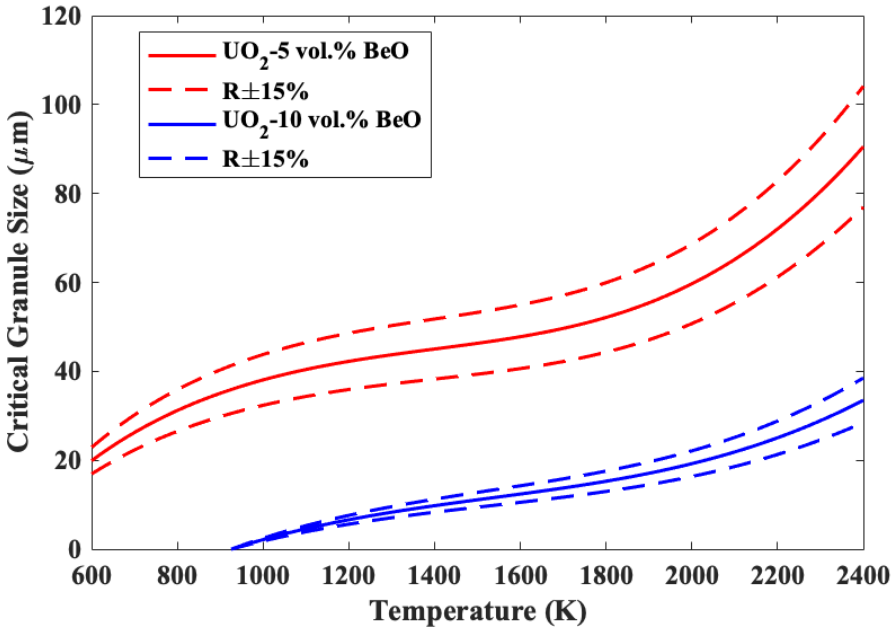

Figure 5.28 The relationship between the critical granule size, below which the composite thermal conductivity is lower than UO_2, and temperature for UO_2-BeO composites with continuous microstructures with 5 vol.% and 10 vol.% BeO

As alluded to in Fig. 5.26 and Fig. 5.27, Fig. 5.28 highlights the sensitivity of the critical granules size to the concentration of BeO and the interfacial thermal resistance. While for the 10 vol.% BeO case the response with temperature is muted, the 5 vol.% BeO case begins to increase markedly around 1800 K and has varies more with the uncertainty associated with the interfacial thermal resistance measurement. Notably in the 5 vol.% case, while 50 μm granule cells would contribute to higher thermal conductivity during normal operating conditions, in an accident scenario granule cells from 50 μm up to as

large as 100 μm would negatively impact the composite thermal conductivity as compared to UO_2, assuming no change in the interfacial thermal resistance at these temperatures.

In addition to thermal considerations, Hickman *et al.* considered irradiation damage effects on the design of UO_2-BeO composites reporting to retain compact strength, the interparticle spacing, or the BeO thickness, should be no larger than 30 μm [123]. In combination, this work and the results by Hickman *et al.* limit the UO_2 granule size in an ideal, continuous microstructure. For a UO_2-5 vol.% BeO composite, the UO_2 granule size should be limited to above roughly 100 μm to maintain thermal conductivity improvement over UO_2 for the full temperature range and below 1740 μm to maintain compact strength throughout irradiation. For a UO_2-5 vol.% BeO composite, the UO_2 granule size should be limited to above roughly 40 μm to maintain thermal conductivity improvement over UO_2 for the full temperature range and below 840 μm to maintain compact strength throughout irradiation.

6. CONCLUSIONS

The aim of the present research was to quantify the interfacial thermal resistance in UO_2-BeO composites and examine the role of the interfacial thermal resistance on the effective thermal conductivity of microstructures with a continuous BeO network, applicable as an accident tolerant fuel. In contrast with the existing measurements, this work sought to apply the experimental flash method to quantify the interfacial thermal resistance from a microstructure with spherical, dispersed BeO granules to capture all the boundary contributions, excluded from theoretical approaches, and limit uncertainty in the analytical model applied. Rather than relying on effective thermal conductivity in the literature, this work fabricated and characterized samples specifically designed for the task of quantifying the interfacial thermal resistance, eliminating unnecessary assumptions and improving confidence in the measurement accuracy.

Dense, robust UO_2-BeO composites with a dispersed microstructure were fabricated using methods aligned with industry practice. Composites of 5, 10, and 15 vol.% BeO granules with a limited size distribution of 150-250 μm were selected to provide uniform microstructures with distinct thermal properties. The series of samples was within 1.5% of 95% of the theoretical density and demonstrated sensible thermal conductivity improvement over UO_2 as measured by LFA. The results affirm the methodology reported by Garcia *et al.* as reliably producing high quality composites, an issue in recent literature resulting in low density BeO networks [34]. Of practical interest, however, composites fabricated with larger granules resulted in lower bulk density, a

finding generally supported in the literature [117-118]. The fabrication results lay the groundwork for future research establishing the practical upper limit of the granule size to complement the thermal and irradiation limits identified in this work.

The fabricated microstructures were characterized in backscatter electron mode by microprobe. Quantitative stereology across the sample set measured over 1000 granules. The two-dimensional granule cross-sectional area was transformed into the three-dimensional diameter by fitting a kernel distribution to the total empirical continuous distribution function, representing the distribution as a finely binned histogram, and inversion to determine an average granule diameter of 242.2 μm when weighted by volume. The results contribute to the confidence level in the fit interfacial thermal resistance compared to previous work where sieve cutoffs and cross-sectional micrographs solely informed the granule size. The fit and stereological inversion resulted in an approximately 40% difference in the average diameter compared to the granule cross-sections and a 15% difference with the monodisperse assumption, inaccuracies which contribute to measurement uncertainty in the literature. Further improvements could increase the granule sample size to reduce noise in the raw data.

The interfacial thermal resistance was elucidated by fitting the experimental data using the Hasselman-Johnson model to a value of 4.6×10^{-6} m^2-K/W with a ±15% uncertainty. As expected, the results showed that the experimentally measured interfacial thermal resistance was greater than the theoretical predictions and large enough to warrant design consideration here. The magnitude of the interfacial thermal resistance set a practical lower limit on the UO_2 granules in continuous microstructures that without the

interfacial thermal resistance could be reduced without penalty to maximize the BeO coverage. Surprisingly, the results are on the scale of measurements fit to continuous microstructures of varying fabrication technique and BeO density, cautiously suggesting the interfacial thermal resistance is less sensitive to fabrication process than initially posited based on the spread in reported improvement.

Whilst this study did not confirm the interfacial thermal resistance as the critical parameter differentiating the effective thermal conductivity of UO_2-BeO composites in the literature, the measurement is nonetheless crucial to further analysis of the fuel form. The UO_2 granule size, partially reported in the experimental literature on continuous microstructures, only impacts the effective thermal conductivity in models and simulations when an interfacial thermal resistance is implemented. Additionally, the BeO network shape and orientation descriptors, similarly related to the interfacial thermal conductivity, are sparsely noted in the literature and often fit. This could be a fruitful area for further work for this study is limited by the lack of information for the various continuous microstructures reported in the literature.

In addition to the thermal conductivity, this work fit the thermal conductivity of BeO and UO_2 in application which agreed with the literature and the baseline UO_2 sample fabricated, respectively, suggesting a porosity of ~3% in the sampled area. The baseline UO_2 data, however, was roughly 10% higher than the correlation recommended by Fink, which has a reported 10% uncertainty. For the dispersed microstructures, the interfacial thermal resistance and matrix and particle thermal conductivities are reliable predictors of the effective thermal conductivity; however, the uncertainty imparted by literature thermal

conductivity correlations and commonly reported characterization techniques, such as bulk density and sieve sizes, can be seen in Fig. 5.24. The results indicate well-characterized microstructures and materials are principal to simulation and model accuracy against experimental results and likely limit the broad success of the models in this work compared to the experimental continuous microstructures in literature.

In spite of the limitations in understanding the existing literature for UO_2-BeO composites with continuous microstructures, the difficulties highlight the major strength of the work presented. This project is the first dedicated experimental investigation of the interfacial thermal resistance in UO_2-BeO composites. Unlike previous measurements of the interfacial thermal resistance which relied on underdetermined analytical models and literature thermal conductivity correlations, this study, grounded in the inverse method reported by Nan, Li, and Birringer, fabricated defined, well-characterized microstructures of varying granule diameter and concentration to specifically quantify the interfacial thermal resistance and reduce uncertainty.

While the analytical model derived by the method of equivalent resistance did not satisfactorily predict the experimental effective thermal conductivity, conclusions can be drawn for idealized continuous microstructures to improve the microstructure design for maximal thermal conductivity. This study identifies the critical granule size for UO_2 in the composite to maintain thermal conductivity improvement over UO_2 across operating and accident conditions. A lower limit of 100 μm is identified for a 5 vol.% BeO composite and 40 μm for a 10 vol.% BeO composite, although this assumes the interfacial thermal resistance is constant up to the eutectic temperature. High temperature measurement of

the effective thermal conductivity of the samples in this work would contribute greatly to understanding how the interfacial thermal resistance and critical granule size vary with temperature. While upper limits based off of predicted irradiation damage in BeO exist, the practical upper limit to the granule diameter, and effective thermal conductivity, is likely set by the specific processing and fabrication. These experiments showed that granules between 300-450 μm likely contributed to open porosity in the sample bulk which distinctly reduced the effective thermal conductivity.

In summary, the following results and conclusions encapsulate the major outcomes of this work:

1) The fabrication of dilute, dispersed BeO microstructures enabled the quantification of the interfacial thermal resistance with improved characterization and reduced uncertainty.
2) The characterization of the true BeO granule distribution by the inversion method increased the average diameter (242.2 μm) by 40% over the literature approach of using the apparent granule size and by 15% over the monodisperse assumption.
3) The average interfacial thermal resistance over the temperature range studied was calculated as 4.6×10^{-6} m^2-K/W with a ±15% uncertainty, unexpectedly on the same order of magnitude of previous measurements for continuous microstructures.
4) The measured interfacial thermal resistance value had practical impacts on the fabrication of UO_2-BeO composites, limiting the minimum UO_2 granule size

in continuous microstructures to 100 μm for 5 vol.% BeO and 40 μm for 10 vol.% BeO for improved thermal conductivity across temperatures of interest in accident scenarios, an effect not replicated without the interfacial thermal resistance where there is no penalty to reducing UO_2 granule size and increasing BeO coverage.

This research adds to the growing body of work indicating that the interfacial thermal resistance is vital to modeling and understanding the effective thermal conductivity of UO_2-BeO composites, as well as other enhanced UO_2 fuel composites with SiC and other additives. The new understanding reported here should help improve predictions of the thermal conductivity and evaluate the impact of additional features, such as the shape and orientation descriptors for the BeO network. Overall, this study strengthens the indication that the component thermal conductivity and interfacial thermal resistance are necessary to quantify for particular fuel designs and fabrications processes. The insight gained will be of assistance to the informed design of the fuel microstructure, including particle size and composition selection and evaluation of the component morphology, for improved accident tolerance.

REFERENCES

1. U.S. Department of Energy: Roadmap: Development of Light Water Reactor Fuels with Enhance Accident Tolerance, (Washington, DC: Author, 2015).

2. Organization for Economic Co-operation and Development, Nuclear Energy Agency, Nuclear Science: Second Meeting of the Expert Group on Accident Tolerant Fuels for Light Water Reactors, (Issy-les-Moulineaux, France: Author, 2014).

3. K.H. Sarma, J. Fourcade, S-G. Lee, A.A. Solomon, New processing methods to produce silicon carbide and beryllium oxide inert matrix and enhanced thermal conductivity oxide fuels, J. Nucl. Mater. 352 (2006) 324-333.

4. S. Yeo, E. McKenna, R. Baney, G. Subhash, J. Tulenko, Enhanced thermal conductivity of uranium dioxide-silicon carbide composite fuel pellets prepared by spark plasma sintering (SPS), J. Nucl. Mater. 433 (2013) 66-73.

5. A.K. Singh, S.C. Zunjarro, R.P. Singh, Processing of uranium oxide and silicon carbide based fuel using polymer infiltration and pyrolysis, J. Nucl. Mater, 378 (2008) 238-243.

6. S. Yeo, R. Baney, G. Subhash, J. Tulenko, The influence of SiC particle size and volume fraction on the thermal conductivity of spark plasma sintered UO_2-SiC composites, J. Nucl. Mater. 442 (2013) 245-252.

7. Z. Chen, G. Subhash, J.S. Tulenko, Master sintering curves for UO_2 and UO_2-SiC composites processed by spark plasma sintering, J. Nucl. Mater. 454 (2014) 427-433.

8. Z. Chen, G. Subhash, J.S. Tulenko, Raman spectroscopic investigation of graphitization of diamond during spark plasma sintering of UO_2-diamond composite nuclear fuel, J. Nucl. Mater., 475 (2016) 1-5.

9. P. Medvedev, Effect of diamond additive on the fission gas release in UO_2 fuel irradiated to 7.2 GWd/tHM, Ann. Nucl. Energy 139 (2020) 107282.

10. S.W. Lee, H.T. Kim, I.C. Bang, Performance evaluation of UO_2/graphene composite fuel and SiC cladding during LBLOCA using MARS-KS, Nucl. Eng. Des. 257 (2013) 139-145.

11. H.S. Lee, D.J. Kim, J.H. Yang, D.R. Kim, Numerical and experimental investigation on thermal expansion of UO_2-5 vol% Mo microcell pellet for qualitative comparison to UO_2 pellet, J. Nucl. Mater., 518 (2019) 342-349.

12. H.S. Lee, D.J. Kim, S. W. Kim, J.H. Yang, Y.H. Koo, and D.R. Kim, Numerical characterization of micro-cell UO_2Mo pellet for enhanced thermal performance, J. Nucl. Mater. 477 (2016) 88-94.

13. L. Cheng, B. Yan, R. Gao, X. Liu, Z. Yang, B. Li, Y. Zhong, P. Liu, Y. Wang, M. Chu, B. Bai, and P. Zhang, Densification behavior of UO_2/Mo core-shell composite pellets with a reduced coefficient of thermal expansion, Ceram. Int. 46 (2020) 4730-4736.

14. L. Cheng, R. Gao, B. Yan, C. Zhang, R. Li, C. Ma, Z. Yang, B. Li, Y. Wang, Y. Zhong, M. Chu, B. Bai, and P. Zhang, Investigation of the residual stress in UO_2-Mo composites via a neutron diffraction method, Ceram. Int. 46 (2020) 15889-15896.

15. B. Li, Z. Yang, M. Chu, Q. Huang, Z. Wang, R. Goa, Y. Zhong, X. Liu, L. Duan, and P. Zhang, Ti3SiC2/UO_2 composite pellets with superior high-temperature thermal conductivity, Ceram. Int. 44 (2018) 19846-19850.

16. R. Latta, S.T. Revankar, and A.A. Solomon, Modeling and measurement of thermal properties of ceramic composite fuel for light water reactors, Heat Transf. Eng. 29 (2008) 357-365.

17. A.A. Solomon, H.S. Kuchibhotla, S.T. Revankar, S.M. McDeavitt, and J.C. Ragusa, Ceramic-ceramic composites and process therefor, nuclear fuels formed thereby, and nuclear reactor systems and processes operated therewith, WO 2012/047657 A3, 12 April 2012.

18. G.A. Slack, S.B. Austerman, Thermal Conductivity of BeO Single Crystals, J. Appl. Phys. 42 (1971) 4713-4717.

19. J.K. Fink, Thermophysical properties of uranium dioxide, J. Nucl. Mater. 279 (2000) 1-18.

20. "CINDAS Recommended Data Based on CINDAS Evaluation from Available Information," https://cindasdata.com/Applications/TPMD/. Accessed 7 August 2019.

21. C.E. McNeilly: The Pseudo Ternary System BeO-UO_2-PuO_2, (Richland, WA: Battelle Memorial Institute/Pacific Northwest National Laboratory, 1967).

22. S.T. Revankar, W. Zhou, D. Chandramouli, Thermal Performance of UO_2-BeO Fuel during a Loss of Coolant Accident, Int. J. Nucl. Energy Sci. Eng. 5, (2015) 1-8.

23. D. Chandramouli, S.T. Revankar, Development of Thermal Models and Analysis of UO_2-BeO Fuel during a Loss of Coolant Accident, Int. J. Nucl. Energy 2014 (2014) 1-9.

24. R. Liu, W. Zhou, P. Shen, A. Prudil, P.K. Chen, Fully coupled multiphysics modeling of enhanced thermal conductivity UO_2-BeO fuel performance in a light water reactor, Nucl. Eng. Des. 295 (2015) 511-523.

25. R. Gao, Z. Yang, B. Li, B. Yan, L. Cheng, Y. Wang, Y. Zhong, Q. Huang, Z. Wang, M Chu, B. Bai, X. Zhu, P. Zhang, R. Li, T. Liu, Fabrication of UO_2-BeO composite pellets with superior thermal conductivity based on multi-parameter theoretical analyses, J. Nucl. Mater. 542 (2020) 152533.

26. X. Zhu, R. Gao, H. Gong, T. Liu, D.Y. Lin, H. Song, UO_2/BeO interfacial thermal resistance and its effect on fuel thermal conductivity, Ann. Nucl. Energy 154 (2021) 108102.

27. F. Badry, R. Brito, M.G. Abdoelatef, S. McDeavitt, K. Ahmed, An experimentally validated mesoscale model of thermal conductivity of a UO_2 and BeO composite nuclear fuel, JOM 71 (2019) 4829.

28. D.P.H. Hasselman, L.F. Johnson, Effective thermal conductivity of composites with interfacial thermal barrier resistance, J. Compos. Mater. 21 (1987) 508-515.

29. Y. Benveniste, T. Miloh, The effective conductivity of composites with imperfect thermal contact at constituent interfaces, Int. J. Eng. Sci. 24 (1986) 1537-1552.

30. Y. Benveniste, Effective thermal conductivity of composites with a thermal contact resistance between the constituents: Nondilute case, J. Appl. Phys. 61:8 (1987) 2840-2843.

31. C.-W. Nan, R. Birringer, D.R. Clarke, H. Gleiter, Effective thermal conductivity of particulate composites with interfacial thermal resistance, J. Appl. Phys. 81 (1997) 6692-6700.

32. C.-W. Nan, X.-P. Li, R Birringer, Inverse problem for composites with imperfect interface: Determination of interfacial thermal resistance, thermal conductivity of constituents, and microstructural parameters, J. Am. Ceram. Soc. 83:4 (2000) 848-854.

33. A.G. Every, Y. Tzou, D.P.H. Hasselman, R. Raj, The effect of microstructure on the thermal conductivity of particulate ZnS/Diamond composites, Acta Metall. Mater. 40:1 (1992) 123-129.

34. C.B. Garcia, R.A. Brito, L.H. Ortega, J.P. Malone, S.M. McDeavitt, Manufacture of a UO_2-based nuclear fuel with improved thermal conductivity with the addition of BeO, Metall. Mater. Trans. E, 4E (2017) 70-76.

35. J.N. Cuzzi and D.M. Olsen, Recovering 3D particle size distributions from 2D sections, Meteorit. Planet Sci. 52 (2017) 532-545.

36. P.L. Goldsmith, The calculation of true particle size distributions from the sizes observed in a thin slice, Brit. J. Appl. Phys. 18 (1967) 813-830.

37. L.M. Cruz-Orive, Particle size-shape distributions: The general spheroid problem; I: Mathematical model, J. Microsc-Oxford 107 (1976) 235-253.

38. L.M. Cruz-Orive, Particle size-shape distributions: The general spheroid problem; II: Stochastic model and practical guide, J. Microsc-Oxford 112 (1978) 153-157.

39. L.M. Cruz-Orive, Distribution-free estimation of sphere size distributions from slabs showing overprojection and truncation, with a review of previous methods. J. Microsc-Oxford 131 (1983) 265-290.

40. S. Ishimoto, M. Hirai, K. Ito, Y. Korei, Thermal Conductivity of UO_2-BeO Pellet, J. Nucl. Sci. Technol. (Abingdon, U.K.) 33 (1996) 134-140.

41. B. Li, Z. Yang, J. Jia, Y. Zhong, X. Liu, P. Zhang, R. Gao, T. Liu, R. Li, H. Huang, M. Sun, D. Mazhao, High temperature thermal physical performance of BeO/UO_2 composites prepared by spark plasma sintering (SPS), Scripta Mater. 142 (2018) 70-73.

42. P.G. Lucuta, H. Matzke, I.J. Hastings, A pragmatic approach to modelling thermal conductivity of irradiated UO_2 fuel: review and recommendations, J. Nucl. Mater. 232 (1996) 166-180.

43. K.J. Geelhood, W.G. Luscher, C.E. Beyer, and J.M. Cuta: FRAPTRAN 1.4: A Computer Code for the Transient Analysis of Oxide Fuel Rods, vol. 1 (Richland, WA: Pacific Northwest National Laboratory, 2011).

44. K.J. Geelhood, W.G. Luscher, C.E. Beyer, and J.M. Cuta: FRAPTRAN: Integral Assessment, vol. 2 (Richland, WA: Pacific Northwest National Laboratory, 2011).

45. NRC: RELAP5/MOD3.3 Code Manual, Volume I: Code Structure, System Models, and Solution Methods, (Rockville, MD: Author, 2006).

46. NRC: RELAP5/MOD3.3 Code Manual Volume III: Developmental Assessment Problems, (Rockville, MD: Author, 2006).

47. K. McCoy, C. Mays, Enhanced thermal conductivity oxide nuclear fuels by co-sintering with BeO: II. Fuel performance and neutronics, J. Nucl. Mater. 375 (2008) 157-167.

48. D.S. Li, H. Garmestani, J. Schwartz, Modeling thermal conductivity in UO_2 with BeO additions as a function of microstructure, J. Nucl. Mater. 392 (2009) 22-27.

49. W. Zhou, S.T. Revankar, R. Liu, M.S. Beni, Microstructure-based thermal conductivity and thermal behavior modeling of nuclear fuel UO_2-BeO, Heat Transfer Eng. 39 (2018) 760-774.

50. F. Boey, A.I.Y. Tok, Y.C. Lam, S.Y. Chew, On the effects of secondary phase on thermal conductivity of AlN ceramic substrates using a microstructural modeling approach, Mater. Sci. Eng. A 335 (2002) 281-289.

51. N. Kürti, B.V. Rollin, F. Simon, Preliminary experiments on temperature equilibria at very low temperatures, Physica 3 (1936) 266-274.

52. W.H. Keesom, A.P. Keesom, On the heat conductivity of liquid helium, Physica 3 (1936) 359-360.

53. P.L. Kapitza, The study of heat transfer in helium ii, J. Phys. (USSR), 4 (1941) 181.

54. M. Zain-ul-abdein, W.S. Awan, H. Ijaz, A.A. Taimoor, A. Muhammad, S.u. Rather, Effect of micro- to nanosized inclusions upon the thermal conductivity of powdered composites with high and low interface resistance, J. Nanomater. 2015 (2015) 1-8.

55. X. Liang, M. Baram, D.R. Clarke, Thermal (Kapitza) resistance of interfaces in compositional dependent ZnO-In_2O_3 superlattices, Appl. Phys. Lett. 102 (2013) 223903.

56. A.M. Limarga, D.R. Clarke, The grain size and temperature dependence of the thermal conductivity of polycrystalline, tetragonal yttria-stabilized zirconia, Appl. Phys. Lett., 98 (2011) 211906.

57. X.-Y. Shen, X.-B. He, S.-B. Ren, H.-M. Zhang, X.-H. Qu, Effect of molybdenum as interfacial element on the thermal conductivity of diamond/Cu composites, J. Alloys Compd. 529 (2012) 134.

58. K. Pietrak, T.S. Wiśniewski, Methods for experimental determination of solid-solid interfacial thermal resistance with application to composite materials, J. Power Technol. 94 (2014) 270-285.

59. V. Khuu, M. Osterman, A. Bar-Cohen, M. Pecht, Considerations in the use of the laser flash method for thermal measurements of thermal interface materials, IEEE Trans. Compon., Packag., Manuf. Technol. 1 (2011) 1015-1028.

60. Y. Wang, K. Fujinami, R. Zhang, C.L. Wan, N. Wang, Y. Ba, and K. Koumoto, Interfacial thermal resistance and thermal conductivity in nanograined $SrTiO_3$, Appl. Phys. Express 3 (2010) 031101.

61. E.T. Swartz and R.O. Pohl, Thermal boundary resistance, Rev. Mod. Phys. 61 (1989) 605-668.

62. A.C. Anderson, The Kapitza Thermal Boundary Resistance Between Two Solids: Nonequilibrium Superconductivity, Phonons, and Kapitza Boundaries, ed. K. E. Gray, (New York, NY: Plenum Press, 1981) 1.

63. G.L. Pollack, Kapitza Resistance, Rev. Mod. Phys. 41 (1969) 48-81.

64. E.T. Swartz, R.O. Pohl, Thermal resistance at interfaces, Appl. Phys. Lett. 51 (1987) 2200-2205.

65. Y. Zhang, D. Ma, Y. Zang, X. Wang, N. Yang, A modified theoretical model to accurately account for interfacial roughness in predicting the interfacial thermal conductance, Front. Energy Res. (2018) doi: 10.3389/fenrg.2018.00048

66. E.S. Landry, A.J.H. McGaughey, Thermal boundary resistance predictions from molecular dynamics simulations and theoretical calculations, Phys. Rev. B 80 (2009) 165304.

67. S. Pettersson, G.D. Mahan, Theory of the thermal boundary resistance between dissimilar lattices, Phys. Rev. B 42 (1990) 7386-7390.

68. P.K. Schelling, S.R. Phillpot, P. Keblinski, Comparison of atomic-level simulation methods for computing thermal conductivity, Phys. Rev. B 65 (2002) 144306.

69. M. Matsui, G.D. Price, A. Patel, Comparison between the lattice dynamics and molecular dynamics methods: Calculation results for $MgSiO_3$ perovskite, Geophys. Res. Lett., 21:15 (1994) 1659-1662.

70. T. Chen, D. Chen, B.H. Sencer, L. Shao, Molecular dynamics simulations of grain boundary thermal resistance in UO_2, J. Nucl. Mater., 452 (2014) 364-369.

71. W.K. Kim, J.H. Shim, M. Kaviany, UO_2 bicrystal phonon grain-boundary resistance by molecular dynamics and predictive models, Int. J. Heat Mass Transfer, 100 (2016) 243-249.

72. R. Liu, W. Zhou, Multiphysics modeling of novel UO_2-BeO sandwich fuel performance in a light water reactor, Ann. Nucl. Energy, 109 (2017) 298-309.

73. L.W. Da Silva, M. Kaviany Micro-thermoelectric cooler: interfacial effects on thermal and electric transport, Int. J. Heat Mass Transf. 47 (2004) 2417-2435.

74. B.T. Wang, P. Zhang, R. Lizárraga, I. Di Marco, O. Eriksson, Phonon spectrum, thermodynamic properties, and pressure-temperature phase diagram of uranium dioxide, Phys. Rev. B. 88 (2013) 104-107.

75. P. Riou, C. Denoual, C.E. Cottenot, Visualization of the damage evolution in impacted silicon carbide ceramics, Int. J. Impact Eng. 21 (1998) 225-235.

76. A.N. Smith, J.L. Hostetler, P.M. Norris, Thermal boundary resistance measurements using a transient thermoreflectance technique, Microscale Thermophys. Eng. 4 (2000) 51-60.

77. F. Lepoutre, D. Balageas, P. Forge, S. Hirschi, J.L. Joulad, D. Rochais, F.C. Chen, Micron-scale thermal characterizations of interfaces parallel or perpendicular to the surface, J. Appl. Phys. 78:4 (1995) 2208-2223.

78. E. Chapelle, B. Garnier, B. Bourouga, Interfacial thermal resistance measurement between metallic wire and polymer in polymer matrix composites, Int. J. Therm. Sci. 48 (2009) 2221-2227.

79. R.F. Hill, P.H. Supancic, Determination of the thermal resistance of the polymer-ceramic interface of alumina-filled polymer composites, J. Am. Ceram. Soc. 87:10 (2004) 1831-1835.

80. W.J. Parker, R.J. Jenkins, C.P. Butler, G.L. Abbott, Flash method of determining thermal diffusivity, heat capacity, and thermal conductivity, J. Appl. Phys. 32 (1961) 1679-1684.

81. R.D. Cowan, Pulse method of measuring thermal diffusivity at high temperatures, J. Appl. Phys. 34 (1963) 926-927.

82. C.-P. Chiu, J.G. Maveety, Q.A. Tran, Characterization of solder interfaces using laser flash metrology, Microelectron. Reliab. 42 (2002) 93-100.

83. J. Absi, D.S. Smith, B. Nait-Ali, S. Grandjean, J. Berjonaux, Thermal response of two-layer systems: Numerical simulation and experimental validation, J. Eur. Ceram. Soc. 25 (2005) 367-373.

84. J. Hartmann, O. Nilsson, J. Fricke, Thermal diffusivity measurements on two-layered and three-layered systems with the laser flash method, High Temp. – High Pressure, 25 (1993) 403-410.

85. N.D. Milosević, M Raynaud, K.D. Maglić, Simultaneous estimation of the thermal diffusivity and thermal contact resistance of thin solid films and coatings using the two-dimensional flash method, Int. J. Thermophys. 24 (2003) 799-819.

86. N.D. Milosević, Optimal parametrization in the measurements of the thermal diffusivity of thermal barrier coatings, Thermal Science 11 (2007) 137-156.

87. N.D. Milosević, Determination of transient thermal interface eresistance between two bonded metal bodies using the laser-flash method, Int. J. Thermophys. 29 (2008) 2072-2087.

88. J.C. Maxwell: A Treatise on Electricity and Magnetism, vol. 1, Clarendon, England: Oxford University Press, 1873, pp. 360.

89. J.C.M. Garnett, Colours in metal glasses and in metallic films, Philos. Trans. R. Soc. A 203 (1904) 385-420.

90. J.C.M. Garnett, Colours in metal glasses, in metallic films, and in metallic solutions, Philos. Trans. R. Soc. A 205 (1906) 237-288.

91. D.A.G. Bruggeman, Berechnung verschiedener physikalischer Konstanten von heterogenen Substanzen ,Ann. Phys. 24 (1935) 636-664.

92. R. Landauer: Electrical Transport and Optical Properties of Inhomogeneous Media, ed. J.C. Garland and D.B. Tanner, New York, NY: American Institute of Physics, 1978, pp.2.

93. L.E. Nielsen, The thermal and electrical conductivity of two-phase systems, Ind. Eng. Chem. Fundam. 13 (1974) 17-20.

94. G. Ondracek, B. Schulz, The porosity dependence of the thermal conductivity for nuclear fuels, J. Nucl. Mater. 46 (1973) 253-258.

95. K. Pietrak, T.S. Wiśniewski, A review of models for effective thermal conductivity of composite materials, J. Power Technol., 95 (2015) 14-24.

96. K. Chockalingam, P.C. Millett, M.R. Tonks, Effects of intergranular gas bubbles on thermal conductivity, J. Nucl. Mater. 430 (2012) 166-170.

97. P.C. Millett, M. Tonks, Meso-scale modeling of the influence of interfranular gas bubbles on effective thermal conductivity, J. Nucl. Mater. 413 (2011) 281-286.

98. P.C. Millet, M.R. Tonks, K. Chockalingam, Y. Zhang, S.B. Biner, Three dimensional calculations of the effective Kaptiza resistance of UO_2 grain boundaries containing intergranular bubbles, J. Nucl. Mater. 439 (2013) 117-122.

99. C.J. Permann, D.R. Gaston, D. Andrš, R.W. Carlsen, F. Kong, A.D. Lindsay, J.M. Miller, J.W. Peterson, A.E. Slaughter, R.H. Stogner, R.C. Martineau, MOOSE: enabling massively parallel multiphysics simulation, SoftwareX 11 (2020) 100430.

100. D.R. Gaston, C.J. Permann, J.W. Peterson, A.E. Slaughter, D. Andrš, Y. Wang, M.P. Short, D.M. Perez, M.R. Tonks, J. Ortensi, L. Zou, R.C. Martineau, Physics-based

multiscale coupling for full core nuclear reactor simulation, Ann. Nucl. Energy 84 (2015) 45-54.

101. K. Ahmed, A. El-Azab, Phase-field modeling of microstructure evolution in nuclear materials, In: W. Andreoni, S. Yip (ed), Handbook of Materials Modeling 2018. Springer, New York, NY 2018, DOI: 10.1007/978-3-319-50257-1_133-1.

102. B. Spencer, D. Schwen, J. Hales, Multiphysics Modeling of Nuclear Materials, In: W. Andreoni, S. Yip (ed), Handbook of Materials Modeling 2018. Springer, New York, NY 2018, DOI: 10.1007/978-3-319-50257-1_131-1.

103. K. Bakker, Using the finite element method to compute the influence of complex porosity and inclusion structures on the thermal and electrical conductivity, Int. J. Heat Mass Transfer, 40 (1997) 3503-3511.

104. M. Teague, M. Tonks, S. Novascone, S. Hayes, Microstructural modeling of thermal conductivity of high burn-up mixed oxide fuel, J. Nucl. Mater. 444 (2014) 161-169.

105. B. Bellamy, T.W. Baker, D.T. Lively, The lattice parameter and density of beryllium oxide determined by precise x-ray methods, J. Nucl. Mater. 6:1 (1962) 1-4.

106. R. Brandt, G. Neuer, Thermal conductivity and thermal radiation properties of UO_2, J. Non-Equilib. Thermodyn. 1 (1976) 3-23.

107. W. Niesel, Dielectric constants of heterogeneous mixtures of isotropic and nonisotropic substances, Ann. Der Phys. 6 (1952) 336-348.

108. C.A. Schneider, W.S. Rasband, K.W. Elceiri, NIH Image to ImageJ: 25 years of image analysis, Nat. Methods, 9 (2012) 671-675.

109. E.R. Weibel, Stereological methods, volume 1: Practical methods for biological morphometry. Cambridge, Massachusetts: Academic Press, 1979.

110. E.R. Weibel, Stereological methods, volume 2: Theoretical foundations. Academic Press, Cambridge, MA, 1980.

111. D.D. Eisenhour, Determining chondrule size distributions from thin-section measurements, Meteorit. Planet Sci. 31 (1996) 243-248.

112. E.E. Underwood, Quantitative stereology. Addison-Wesley, Boston MA, 1970.

113. S.D. Wicksell, The corpuscle problem, I: Case of spherical corpuscles. Biometrica 17 (1925) 84-99.

114. S. Saltykov, The determination of the size distribution of particles in an opaque material from a measurement of the size distribution of their thin sections. In: Elias H (ed) Stereology 1967. Springer-Verlag, New York, 1967, p 163-173.

115. S. Benito, C. Cuervo, F. Pöhl, W. Theison, Improvements on the recovery of 3D particle size distributions from 2D sections, Mater Charact 156 (2019) 109872.

116. D.W. Scott, On optimal and data-based histograms, Biometrika, 66:3 (1979) 605-610.

117. R. Oberacker, Powder Compaction by Dry Pressing. In: Riedel R, Chen I-W (ed) Ceramics Science and Technology. Volume 3: Synthesis and Processing 2012. Wiley-VCH Verlag GmbH & Co. KGaA, 2012.

118. M.N. Rahaman, Ceramic Processing and Sintering. Taylor & Francis Group, Boca Raton, FL, 2003.

119. D. Susan, Stereological analysis of spherical particles: Experimental assessment and comparison to laser diffraction, Metall. Mater. Trans. A 36A (2005) 2481-2492.

120. J.T. Gaskins, P.E. Hopkins, D.R. Merrill, S.R. Bauers, E. Hadland, D.C. Johnson, D. Koh, J.H. Yum, S. Banerjee, B.J. Nordell, M.M. Paquette, A.N. Caruso, W.A. Lanford, P. Henry, L. Ross, H. Li, L. Li, M. French, A.M. Rudolph, S.W. King, Review—Investigation and Review of the Thermal, Mechanical, Electrical, Optical, and Structural Properties of Atomic Layer Deposited High-k Dielectrics: Beryllium Oxide, Aluminum Oxide, Hafnium Oxide, and Aluminum Nitride, ECS J. Solid State Sci. Technol. 6 (2017) N189.

121. N. Nandihalli, T. Mori, H. Kleinke, Effect of addition of SiC and Al_2O_3 refractories on Kapitza resistance of antimonide-telluride, AIP Advances B (2018) 095009.

122. M.M. Yovanovich, Four Decards of Research on Thermal Contact, Gap, and Joint Resistance in Microelectronics, IEEE T Compon Pack T 28 (2005) 182-206.

123. B.S. Hickman, W.B. Rotsey, R.J. Hilditch, K. Veevers, Effects of Irradiation on Beryllia-Based Fuels, J Am Ceram Soc 51:2 (1968) 63-69.